united nations
educational, scientific
and cultural
organization

international atomic
energy agency

the
abdus salam
international centre for theoretical physics

H4.SMR/1241-18

"Workshop on Three-Dimensional Modelling
of Seismic Waves Generation and their Propagation"

25 September - 6 October 2000

LOCAL WAVEFORM INVERSION FOR SOURCE PARAMETERS

A. SARAO, P. SUHADOLC

Department of Earth Sciences
Trieste, Italy

Local Waveform Inversion for Source Parameters

A.Sarao` and P. Suhadolc

Department of Earth Sciences, University of Trieste, Italy

E-mail : angela@dst.univ.trieste.it, suhadolc@dst.univ.trieste.it

New developments in waveform inversion methods together with establishment of high quality-digital seismograph networks have led to important progress in the understanding of earthquake source behavior. We review some recent earthquake source studies from the view point of the methodology employed, paying particular attention to the artifacts of modeling that can led to wrong interpretation of the inversion results. Effects of using different data and accurate Green Functions will be also discussed.

Examples of applications will include both the results of moment tensor determination by waveform inversion in italian tectonic (Friuli, UmbriaMarche) and volcanic areas (Mt. Etna, Vesuvio, Campi Flegrei) as well as studies of detailed rupture process retrieved from observed data for the 1998 Bovec and 1976 Friuli earthquakes. The discussed topics are described in the attached papers. A list of useful references is also provided.

The earthquake source

Earthquake arise through the sudden release of energy within some confined region of the Earth.....

The basic mechanical representation of a seismic source is a confined region with spatial dimension L and time duration L/c where c is the rupture velocity..

When the epicentral distance D >> L, and the wave-lenghts are relatively long ($\lambda/L>>1$), or more rigorously $\lambda D>>L^2$, the region can be taken as a point at wich there is equilibrium of force and moment systems

(Bullen & Bolt, 1985)

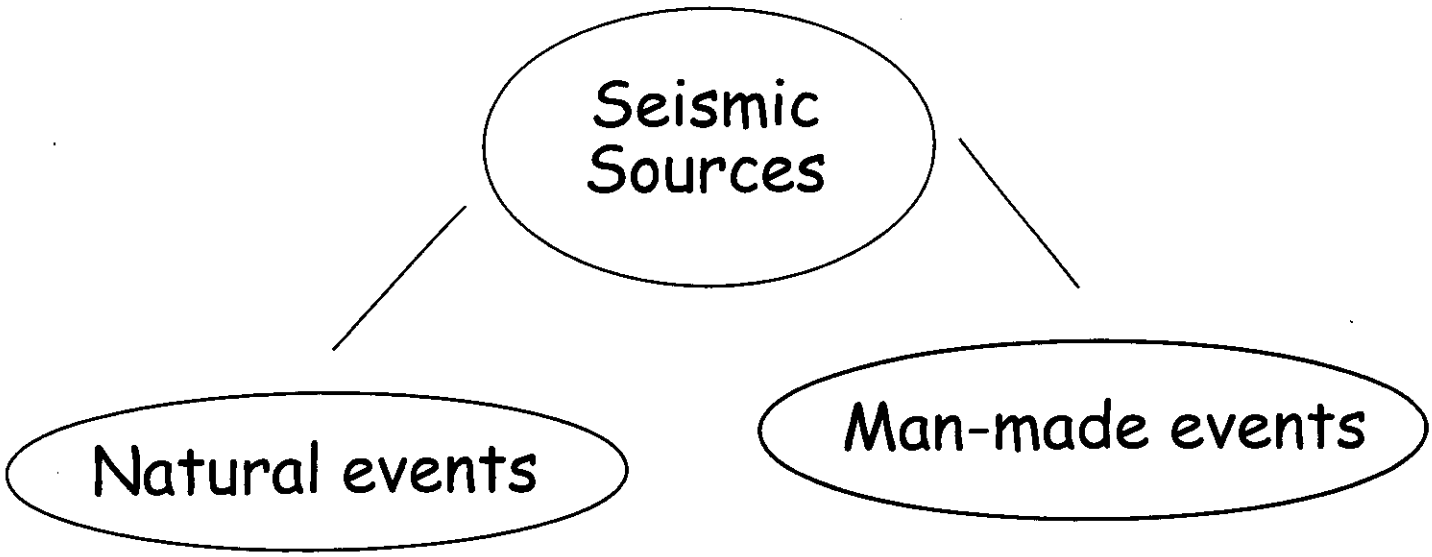

Tectonic earthquakes

Volcanic Tremors and earthquakes

Rock Falls, collapse of Karst Cavities

Storm microseisms

Explosions, Vibrators

Reservoir Induced earthquakes

Mining Induced Earthquakes

Cultural Noise

The forward problem can be written schematically as

$$d_i = F_i\,[m(r)]$$

where $m(r)$ is a model describing some physical property of the Earth, d_i i sthe predicted value for datum i and F_i is a functional whose existence implies that if we know m exactly, we could predict the data perfectly.

The simplest class of inverse solutions is the forward modelling, involving an educated guess. The fundamental weakness of this procedure is that once a model is found that fits the data, one does not know how reliable that model is.

The inverse problem can be written formally as:

$$m(r) = F_i^{-1}\,[d_i\,]$$

Existence: Does any model fit the data?
Uniqueness: Can the data uniquely constrain the model?
Construction: How can we find a solution?
Appraisal: How well do the data constrain the model?

Resolution

Absolute resolution is difficult to address, because one can evaluate the resolution only for the specific problem, not for the actual earthquake source.
Therefore, usual resolution matrices are of limited value and can give only relative estimates of error.

One way is to compare solutions that utilize different data sets, parametrizations, constraints, and inversion norms.

In terms of fitting the data many solutions give an equally acceptable model. The similarities of these different solutions are considered to be the aspects of the rupture model that are better resolved, in an absolute sense.

The physical constraints used should, however, be clearly stated!

Robustness

Use different methods --> the common features of these solutions point out robust characteristicss of the slip distribution that are independent of the inversion parametrization.

One can use botstrapping and jack-kniving techniques.

Instability and non-uniqueness

Increasing the model dimension results in a decrease of the solution uniqueness. To stabilize the problem external constraints need to be placed on the inverison.

The parametrization itself severly restricts the possible solutions and has a big stabilizing effect. *Attention!* A too restrictive parametrization can lead to the true solution lying outside the solution space of the model!

Need to parametrize the problem with sufficient flexibility to encompass realistic models of faulting:
---> physical constraints serve to stabilize the inversion.

Physical constraints are desirable stabilizing tools because they can be unambiguously stated and easily adapted to reflect the current knowledge of the earthquake source physics.

Some techniques require the use of several initial random models to verify that the solution is stable with respect to the starting model and inversion procedure.

Goodness of the solution
Objective (or cost) function

This is the function to be minimized in order to obtain an acceptable fit between the data and the model.

$$\Sigma_{i=1}^{N} W_i \int [x_i(t) - u_i(t)]^2 dt = \text{minimum}$$

with $x_i(t)$ the synthetics, $u_i(t)$ the data and W_i some weight given to the data.

This is the L2 norm, but also the L1 and other norms can be used. Generally the choice is not a critical one.

Physical constraints

Positivity of slip
Strong causality (limits on rupture velocity)
Weak causality (rupture velocity smaller than P-wave velocity)
Model fits observed surface offsets
Tapering of slip to zero at the bottom of the fault
Find least moment or predetermined moment model
Model which incorporates minimum and maximum limits on rupture velocity

Other constraints

Find spatially smoothest model
Find minimum norm model

Incorporated as limits to the current model or as linear functions appended to the calculation of the objective function.

Moment Tensor Decomposition

The equivalent forces of a general seismic point source can be determined from the analysis of the eigenvalues and eigenvectors of the moment tensor.

A common way to decompose the moment tensor is in terms of ISOTROPIC, DOUBLE COUPLE (DC) and Compensated Vector Linear Dipole (CLVD) components.

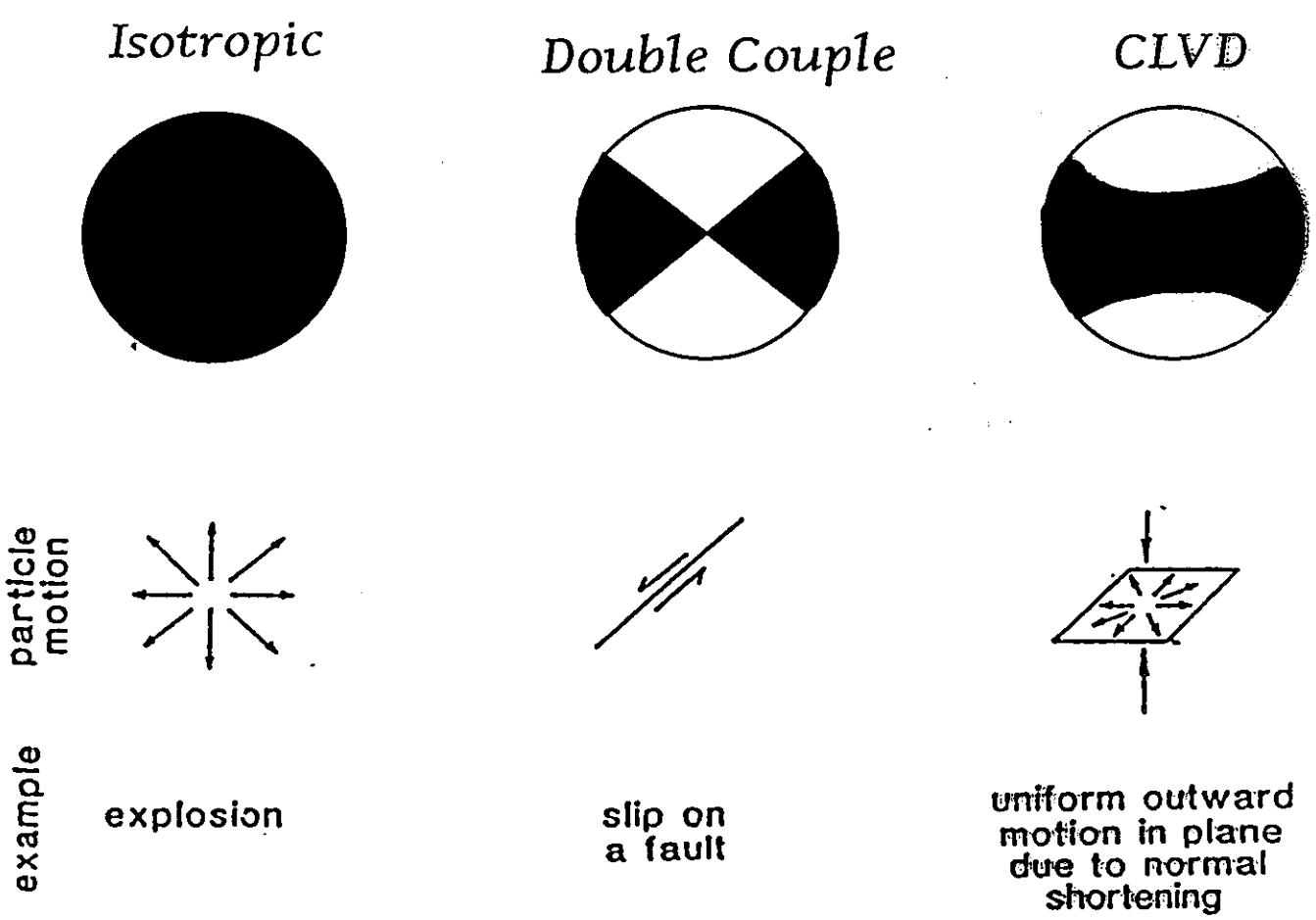

(Frolich & Apperson, 1992)

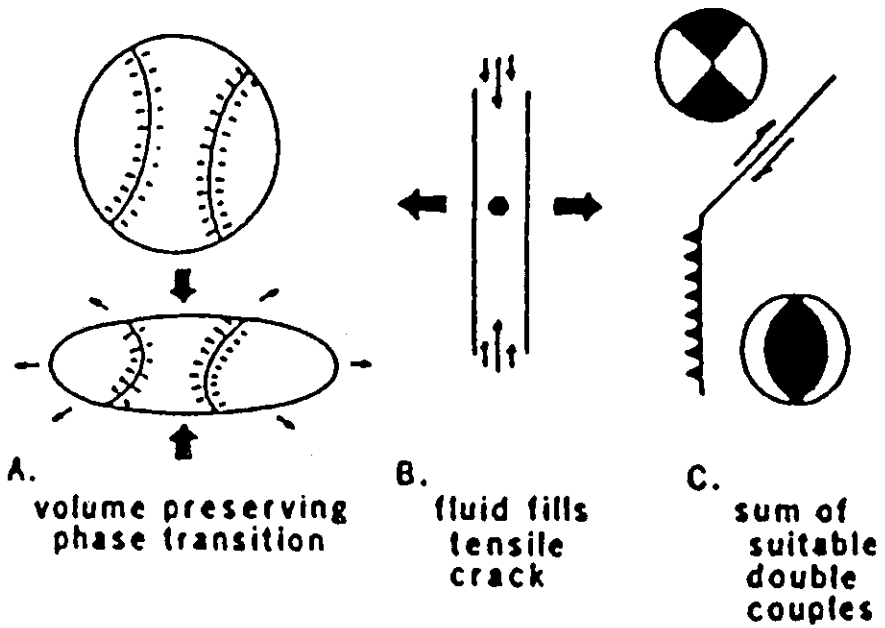

Fig. 1. Suggested models for a CLVD source: For a pure CLVD source particle motion is inward (outward) along one axis, and outward (inward) along the two normal axes, with no net volume change. This might occur; (a) if a phase change caused a spherical volume to become disk-shaped, with no net change in volume; (b) when fluid suddenly fills a tensile crack; and (c) if two double-couple earthquakes occur simultaneously. The resulting source is a pure CLVD if they have the same size, and if they have parallel P (or T) axes and perpendicular B axes. Here the focal mechanisms and faults are shown in map view.

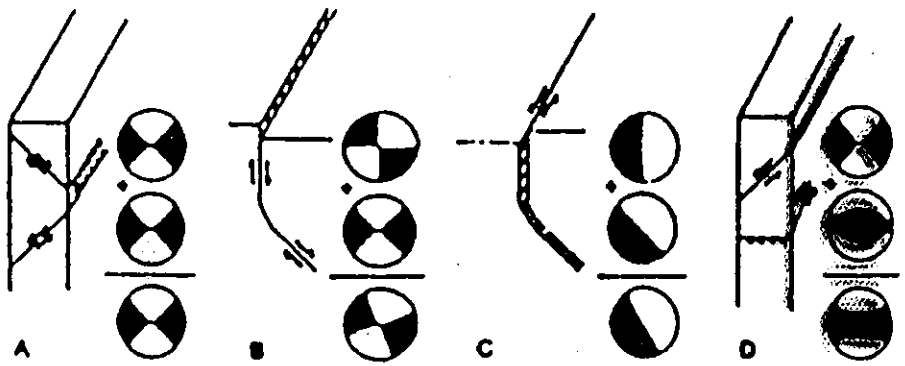

Fig. 2. The sum of pure double-couple subevents may produce a source which is a pure double couple, a pure CLVD, or any combination in between. Thus subevents with the same B-axes, as in (a) or (b), or subevents with the same slip vectors, as in (c), produce a pure double couple. However, subevents having the same P axes but perpendicular B axes add to form a pure CLVD event. Such a P_{edge} source pattern might occur at the edge of a subducting lithospheric slab. In this figure the focal mechanisms are shown as back-hemisphere projections.

Some methods of moment tensor inversion

NEIC Fast Moment Tensors

This is an effort by the US National Earthquake Information Center (NEIC) in co-operation with the IRIS Data Managment Center to produce rapid estimates of the seismic moment tensor for earthquakes with body wave magnitudes > 5.7. Broadband waveform data are quickly retrieved from IRIS stations and transmitted to NEIC by Internet. These data at teleseismic distances contain the *P* waveforms that are used to improve the earthquake locations over what was reported initially and to compute a seismic moment tensor using a technique based on optimal filter design (Sipkin, 1982). The solution is then disseminated by e-mail to a list of subscribers. To register send a request by e-mail to *sipkin@usgs.gov.*
More information under *http://gldss7.cr.usgs.gov/neis/FM/fast_moment.html.*

Harvard CMT solutions

The Harvard group maintains the most extensive catalogue of centroid moment tensor (CMT) solutions for strong (mainly $M > 5.5$) earthquakes over the period from 1976 till present. This and quick CMT solutions of recent events can be viewed at *http://www.seismology.harvard.edu/projects/CMT/.* The Harvard CMT method makes use of both very long-period (T > 40 s) body waves from the *P* wave onset until the onset of the fundamental modes and so-called mantle waves at T > 135 s that comprise the complete surface wave trains. Besides the moment tensor the iterative inversion procedure seeks also a solution for the best point source location of the earthquake. This is the point where the system of couples is located in the source model described by the moment tensor. It represents the integral of the moment density over the extended rupture area. This centroid location may, for very large earthquakes, significantly differ from the hypocentre location based on arrival times of the first *P* wave onsets. The hypocentre location corresponds to the place where rupture started. Therefore, the offset of the centroid location relative to the hypocentral location gives a first indication on rupture directivity. In case of the August 17, 1999 Izmit (Turkey) earthquake the centroid was located about 50 km east of the "*P*-wave" hypocentre. It coincided with the area where the maximum surface ruptures were observed.

EMSC rapid source parameter determinations

This method uses a grid search algorithm to derive within 24 hours after the event fault plane solutions and seismic moment of earthquakes ($M > 5.5$) in the European-Mediterranean area. This is an initiative of the European-Mediterranean Seismological Centre (Bruyeres-le-Chatel, France, *http://www.emsc-csem.org/*) and the GEOFON Programme at the GeoForschungs- Zentrum Potsdam (*http://www.gfz-potsdam.de/geofon/*). The data used are P- and S-wave amplitudes and polarities. More information through *http://www.gfz-potsdam.de/pb2/pb24/emsc/emsc.html.*

Relative moment tensor inversion

Especially for the inversion of local events so called relative moment tensor inversion schemes have been developed (Oncescu, 1986; Dahm 1993, 1996). If the sources are separated by not more than a wavelength, the Green's functions can be assumed to be equal with negligible error. In this case it is easy to construct a linear equation system, which relates the moment tensor components of a reference event to those of another nearby event. This avoids the calculation of high-frequency Green's functions necessary for small local events and all problems connected with that (especially the necessity of modelling site transfer functions in detail).
This is a very useful scheme for the analysis of aftershocks if a well determined moment tensor of the main shock is known. Moreover, if enough events with at least slightly different mechanisms and enough recordings are available, it is also possible to eliminate the reference mechanism from the equations (Dahm 1993, 1996). This is interesting for volcanic areas, where events are swarm-like and of similar magnitude, and where a reference moment tensor cannot be provided (Dahm 1997).

http://www.seismo.com/msop/nmsop/nmsop.html
by Global Seismological Services

Working Group on Moment Tensor Determination

http://www.esg.ca/esc.html

Purpose :
The evaluation of earthquake source mechanism and characterization of failure components using seismic moment tensor inversion has been used for quite some time. In spite of the increasing number of such applications, the large diversity of such methodologies used and the limited statistical analysis employed make often difficult both the comparison and the validation of the results obtained. The purpose of this Working Group is to stimulate the objective study and analysis of the methodologies and results obtained by moment tensor inversion. This web page has been created to support this effort and is intended:

(1) to make sample data sets available to all those interested in seismic moment tensor inversion;

(2) to provide access to freely available software;

(3) to create quick and reliable technical discussion and dissemination framework.

Sileny and Panza's method

(Sileny et al., GJI, 1992; 1996)

The method consists of two main steps:

1) unconstrained linear inversion to determine, from the recorded seismograms, the six moment rate functions;

$$u_k(t) = \dot{M}_{ij}(t) \otimes g_{ki,j}(t)$$

where the $g_{ki,j}$ is the far field term of the space derivative of the Green function

Once the Green functions are determined (Panza 1985), the MTRFs are obtained by using a parametrization of the moment rate functions by a series of triangles overlapping in their half-width (Nabelek, 1984).

2) ***constrained non-linear inversion where the moment rate functions determined in the first step are used as data to obtain the average mechanism and the source time function.***

The mechanism and the source time function are obtained after factorization of the MTRFs

$$\dot{M}_{ij}(t) \rightarrow M_{ij} m(t).$$

In other words, we look for a constant MT and a common source time function. The problem is solved iteratively by imposing constraints such as

- positivity of the source time function
- a mechanism consistent with clear readings of first arrival polarities (when these are available).

The predicted MTRFs are then matched to the observed MTRFs obtained as output of the first step.

Monitoring volcanic and geothermal areas by full seismic moment tensor inversion: are non-double couple components always artifacts of modeling?

Giuliano Francesco Panza (1,2) and Angela Saraò (1)

1) Dipartimento di Scienze della Terra, Università di Trieste, Via E. Weiss 1, 34127 Trieste, ITALY

2) The Abdus Salam International Centre for Theoretical Physics, SAND Group, Trieste, ITALY

Accepted ... Received ... ; in original form ....

SHORT TITLE: Are non-double couples always artifacts of modeling?

Corresponding author: Angela Saraò

Department of Earth Sciences, University of Trieste

Via E. Weiss, 4 - 34127 TRIESTE - ITALY

Tel. +39.040.6762127 Fax: +39.040.676211

E-mail angela@dst.univ.trieste.it

Monitoring volcanic and geothermal areas by full seismic moment tensor inversion: are non-double couple components always artifacts of modeling?

G.F. Panza (1,2) & A. Saraò (1)

1) Dipartimento di Scienze della Terra, Università di Trieste, Via E. Weiss 1, 34127 Trieste, ITALY

2) The Abdus Salam International Centre for Theoretical Physics, SAND Group, Trieste, ITALY

SUMMARY

Non-double couple mechanisms in volcanic environments are indicators of local modifications of the stress field induced by dike injection, high fluid pressure or by thermal cooling. Nevertheless, the possible biasing effects of wave propagation in structurally complicated regions, the presence of noise or the inappropriate station coverage can make the identification of non-double couple as true source phenomena uncertain.

In this paper we review possible sources of false non-double couple and we estimate the reliability of the non-double couple solutions on the basis of the error analysis that includes the variance of the modeling and of the noise in the data. Our analysis of synthetic and real data shows that we can identify - within the confidence level of 99% and 95% respectively - spurious non-double couples due to inadequate station coverage, to noise in the data and to inadequacies of the structural model. Real data analyses must be preceded by synthetic tests in order to define lower limits from which the non-double couple components can be considered statistically significant at a certain confidence level.

KEYWORDS: *Earthquake-source mechanism, Inverse problem, Waveform analysis, Fault-plane solutions, Source time functions, Volcanic activity.*

1. INTRODUCTION

The most general earthquake source is a combination of double couple - the equivalent forces representing a sudden displacement on a fault plane - of compensated linear vector dipole (CLVD) - the equivalent forces of a sudden change in shear modulus in presence of axial strain - and volumetric source - the equivalent forces of sudden volume changes - (Knopoff & Randall, 1970). The seismic moment tensor - a symmetric second order-tensor - gives a complete mathematical representation of the seismic source. Indeed, with a simple parametrization, the seismic moment tensor can be decomposed in double couple, CLVD, related for instance to fluid-driven formation of tensile cracks or to complex events consisting of more subevents occurring along non-parallel fault surfaces, and isotropic source describing explosion or implosion. Therefore, by the seismic-moment tensor we can investigate the physical processes within a volcano induced by magma or fluid movements. Nevertheless the possible biasing effects of wave propagation in structurally complicated regions, the presence of noise or bad station coverage can make the determination of the moment tensor components uncertain. Several authors (e.g. Foulger, 1988; Foulger & Julian, 1993) have demonstrated that structural effects alone are unlikely to explain large amounts of non-double couple and that explanations must be sought in the physical processes acting at the source.

In this paper we discuss moment tensor solutions coming from waveform inversion of both synthetic and recorded signals from Italian volcanic (Campi Flegrei, Vesuvio and Mt. Etna) and geothermal (Larderello) areas. We review some results published in the literature showing situations where spurious non-double couples appear because of bad station coverage, presence of noise in the data or structural inadequacies, and we evaluate their reliability by estimating the error of the moment tensor solutions.

2. MOMENT TENSOR INVERSION

2.1 The method

To obtain the six components of the seismic moment tensor by waveform inversion we apply the method developed by Sileny *et al.* (1992). The problem is non-linear nevertheless the linearity may be kept in the first step of the inversion by introducing the time function describing the development in time of the individual

components of the moment tensor, the moment rate functions (MTRFs). The equation (1) relates the MTRFs to seismic ground motion $u_k(t)$

$$u_k(t) = \dot{M}_{ij}(t) \otimes g_{ki,j}(t) \qquad (1)$$

where the $g_{ki,j}$ is the far field term of the space derivative of the Green function (simply Green function from hereafter) convoluted with the MTRFs.

The method consists of two main steps: (1) unconstrained linear inversion to determine, from the recorded seismograms, the six moment rate functions; (2) constrained non-linear inversion where the moment rate functions determined in the first step are used as data to obtain the average mechanism and the source time function.

In the *first step* the moment rate functions are obtained by deconvolving the Green functions from the data. Using the modal-summation technique (Panza, 1985; Florsch *et al.* 1991), the synthetic Green functions are computed at each grid points of a model space defined by a preassigned range of possible hypocentral coordinates and by two structural models assumed to represent the boundaries of the relevant portion of the structural model space. When the medium in which the source is buried is different from the medium of the recording station, the boundaries are the two structural models. The Green function at a generic point of the space is determined by interpolating the Green function computed at neighboring grid points. Once the Green functions are determined, the MTRFs are obtained applying a method based on Sipkin (1982) approach modified by introducing a damping of the normal equations (Koch, 1991) to obtain reliable moment rate functions when processing local high-frequency waveforms, and by using a parametrization of the moment rate functions by a series of triangles overlapping in their half-width (Nabelek, 1984).

In the *second step* the mechanism and the source time function are obtained after factorization of the MTRFs that is $\dot{M}_{ij}(t) \rightarrow M_{ij}m(t)$ where the mechanism is described by the moment tensor Mij (MT), and if Mij is normalized to unity, the source time function multiplied by m(t) is the scalar moment rate function. In other words, we look for a constant MT and a common source time function. The problem is non-linear and it is solved iteratively by imposing constraints such as positivity of the source time function and the requirement of a mechanism consistent with clear readings of first arrival polarities, when these are available. The predicted MTRFs are then matched to the observed MTRFs obtained as output of the first step.

The advantage of this approach is a simplification of the problem of fitting the input seismograms by converting it into a problem of matching the MTRFs. The number of MTRFs is fixed at six, or five when dealing with only deviatoric sources, and their length is controlled by the number of triangles used for their parametrization. Considering the MTRFs as independent function in step 1 leads to an overparametrization of the problem which is advantageous to absorb poor modeling of the structure (Kravanja *et al.* 1999a). In the second step, assuming that for a weak event it is reasonable to expect a constant mechanism during the energy release, that is the MTRFs are linearly dependent, we search for their correlated part. Moreover if a reverse slip occurs in the deconvoluted MTRFs we attribute it to poor modeling of the structure and we search only for the positive source time function. The ambiguity of deciding about the sign is avoided by seeking for a mechanism consistent with the available clear readings of first-polarities.

2.2 The error analysis

To estimate the uncertainties affecting the mechanism and the source time function we consider the station coverage, the random noise contained in the seismic records, the mislocation of the hypocenters and the inaccurate knowledge of the medium. Assuming that the error distribution tends to a Gaussian distribution, the variance of the modeling and of the data is defined and then transformed into confidence regions of the eigenvalues and eigenvectors of the moment tensor and into error bars of the source time function (Sileny *et al.* 1996). The method of Riedesel & Jordan (1989) is employed to display the moment tensor solutions together with an immediate statistical evaluation of the significance of the non-double couple. The eigenvectors for a pure double couple correspond to the usual definition of tension (T), neutral (B) and compression (P) axes and will be plotted with these symbols even if the source is not a simple double couple. On the surface of the focal sphere unit vectors, whose components in the principal axis system are the eigenvalues of the different types of source mechanisms, are plotted. The vector which describes a general source mechanism is **L**, a double couple source mechanism has the vector representation **d**, two possible CLVD vectors are **l** (if the major dipole is directed along the T axis) or **l'** (if the major dipole is oriented along the pressure axis), and the vector corresponding to a purely isotropic source is **i**. The great circle which connects **d**, **l** and **l'** on the unit sphere defines the subspace on which **L** must lie for a deviatoric source. In Fig. 1(a) we show a double couple since L

lies on top of the vector **d**; Fig. 1(b) is a plot for a CLVD mechanism, in fact **L** is identical to the vector **l**. A deviatoric mechanism free from non-double couple components is shown in Fig. 1(c), where **L** lies on the deviatoric great circle between **d** and **l**. Fig. 1(d) represents a general source mechanism which is a linear combination of equal parts of double-couple, CLVD, and isotropic source (Riedesel & Jordan, 1989).

The uncertainties in the estimates of the moment tensor components are plotted on the focal sphere as projection of the confidence ellipses around **L**, P, T, B. The error ellipse for **L** is a representation of the uncertainty of all the moment tensor components. Let us consider as an example a mechanism whose solutions are computed, for our choice, with a 95% confidence level. The hypothesis of a single double couple can be accepted (Fig. 1e) or rejected (Fig. 1f) if **d** lies respectively inside or outside the **L**'s confidence ellipse. Fig. 1(f) shows a mechanism with a CLVD reliable at the 95% confidence level. For Fig. 1(g) the hypothesis that the mechanism is purely deviatoric cannot be rejected, whereas if the ellipse includes no part of the deviatoric great circle (Fig. 1h) the mechanism has a significant isotropic part at the 95% confidence level (Riedesel and Jordan, 1989).

3. Non double couple components as artifacts of modeling: synthetic tests

Previous studies (Sileny *et al.* 1992; Sileny *et al.* 1996; Kravanja *et al.* 1999a) have discussed advantages and limits of the methodology briefly described in section 2. Also, the capability of the method to distinguish between reliable volumetric components and artifacts has been confirmed by a study of both tectonic earthquakes and man-made explosions in central Switzerland recorded by the Swiss Seismological Service (Campus and Fäh, 1997). In order to have a global vision of the possible false non-double couples due to improper modeling, we summarize below the most important results obtained with synthetic cases.

3.1 Station coverage

Two three-component stations are, in principle, capable of determining the six components of the moment tensor in the time or frequency domain. In the time domain, the six independent data are obtained from P, SV and SH arrivals at two stations. In the frequency domain the tensor M is defined by 6 x 2 scalars, since each element of the moment tensor consists of a real and an imaginary part (amplitude and phase). Therefore if P,

SV, and SH amplitudes and arrivals are known, two three-component stations can determine the system of equations to be solved in the inversion. If only the vertical component of a complete signal is used, two linearly independent pieces of information (P and SV arrivals or P and SV amplitudes and phases) are available. In such a case a minimum of three vertical component stations is required to obtain the complete moment tensor both in the time or frequency domain (Stump & Johnson, 1977; Satake, 1985; Sileny *et al.* 1996). In fact, using only two three-component stations Aoudia *et al.* (2000) studied the main events of the Umbria-Marche (Italy) sequence of September 1997 and obtained the best double couple orientations and the source time functions in excellent agreement with the CMT - Harvard ones, which were based on 42 long-period, three-component stations (Ekström *et al.* 1998).

Nevertheless, even if the number of stations is sufficient, the inversion problem can be well or ill posed due to a regular or sparse distribution of stations on the focal sphere. On this problem Sileny *et al.* (1996) showed that, for stations clustered in a localized region on the focal sphere, the similarity of the Green function to each other introduces instability in the inverse problem. To estimate the limits on the resolution of the individual components of the moment tensor, six configurations (Fig. 2) were considered starting from a regular one (Configuration 1) and going towards a very tightly clustered network distribution (Configuration 6). For each configuration five, four and three stations were used (Fig. 2). As simplification of the experiment the data were generated directly on the focal sphere. Straight rays passing a unit distance through a homogeneous medium are used in the synthesis of the data, thus the structural effects is excluded a priori. The synthesized records for double-couple source correspond to a dip-slip, a strike slip and an isotropic mechanism (explosion).

Fig. 3, modified from Sileny *et al.* (1996), shows the percentage of the decomposed double-couple part for a dip-slip mechanism (Fig. 3a) a strike-slip mechanism (Fig. 3b) and that of the isotropic explosive source. The results are obtained using three-component and vertical component stations. From Fig. 3 one can conclude that configurations 1, 2, 3, are adequate, both for vertical or three component stations. For configurations where stations are clustered in a sector of a focal sphere less than 90° (configuration 5 and 6) the situation worsens and only three-component stations guarantee good results. Indeed if only vertical components are used the double-couple percentage decreases, especially for the strike-slip source, up to 40% (Fig. 3b), whereas for the explosive mechanism (Fig. 3c) the isotropic percentage decreases up to 50% when configuration 6 is used. Inside each

diagram, the source model used to generate the waveforms is plotted. For each mechanism going from configuration 4 to 6 the CLVD part increases. If only vertical components are used, network 5 and 6 guarantee statistically significant solutions only for components above the 50%.

Therefore, since non-double couple components can appear just because of the station configuration, synthetic tests are necessary before to start analysis of real data in order to verify the goodness of the network coverage and to define lower limits above which the reliability of non-double couple components can be evaluated.

To verify the effect of inappropriate station coverage we perform other synthetic tests using real network configurations. The network shown in Fig. 4(a) is located in the Friuli area (NE Italy). Starting from this configuration we perform further tests eliminating some of the stations in the inversion. In order to eliminate problems due to inappropriate structure modeling we generate synthetic noise-free waveforms for a double couple mechanism 4 km deep, using the same one-dimensional structural model used to compute the Green function for the inversion.

Fig. 4(b1) shows the fit between synthetic data (solid line) and the waveforms obtained after the first step of the inversion (dotted line), together with the full (solid line) and deviatoric (dotted line) MTRFs (Fig. b2). Fig. 4(c) shows the results after the second step of the inversion. The retrieved focal mechanism is plotted together with the source time function and the focal mechanism. Obviously since nor noise nor modeling errors are present, the confidence areas are null. The shadowed area of the source time function is representative of its reliable part. The solution obtained from the inversion reproduces exactly the starting mechanism (100% double couple, 0% non-double couple). Similar experiments made reducing the number of stations are shown in Fig. 5. The waveform fits are as good as that of Fig. 4 both for case a) and b), but when only three stations are used (Fig. 5a) a very small CLVD component (2%) appears. For the case of Fig. 5(b) the stations used are four but the resulting coverage is not sufficiently adequate and 10% of CLVD component is found.

As another example we consider the network on Mt. Etna used by Saraò *et al.* (2000) (Fig. 6a). We compute synthetics for a double couple 3.6 km deep located near the central crater of the volcano (Fig. 6a). The structural model used for the forward modeling and for the inversion is the one used at the Istituto Internazionale di Vulcanologia of Catania (Italy) (personal communication) and plotted in Fig. 6(b). The waveform fit is good (Fig. 7a1), the source time function (Fig. 7c) is perfectly reproduced but a spurious non-double couple

mechanism (Fig. 7c) namely 14% of isotropic component is found due to the network configuration. Therefore when working on real data on Mt. Etna, any isotropic component smaller say than 15%, should be considered an artifact of the network configuration rather than a solution related to physical phenomena at the source.

3.2 Noisy data

The most severe case of data contamination is the presence of noise with a frequency content similar to that of the data so that it cannot be simply eliminated by filtering. Sileny *et al.* (1996) performed some tests superimposing on the synthetic data generated for an explosive source, five levels of noise variance reaching 5%, 10%, 15%, 20% and 30% of the peak amplitude in the whole data set. These noise levels are extreme estimates if we consider that a 10% noise level corresponds generally to about 50% (or more) of the amplitude of P waves. Sileny *et al.* (1996) show that with increasing noise, the mechanism remains quite stable for all the cases, whereas the source time function worsens when the noise reaches a level of 30% (Fig. 8). In this latter case the isotropic part decreases whereas the CLVD component increases (Fig. 8). The L error ellipse, plotted as hatched areas around the vector (Fig.8), remains far from the deviatoric circle, i.e. only the isotropic component is reliable, for a noise level as large as 20%. When the noise level reaches 30% there is no way to discriminate between artifacts and physical solutions.

In the same paper Sileny *et al.* (1996) investigated possible non-double couple solutions due to mislocation of the hypocenter, usually the less constrained coordinate of a seismic point source. In such cases they observe that the improper modeling causes an increase of the error bars in the source time function, by about 20%, whereas the mechanism and its confidence ellipses are essentially not altered.

3.3 Structural model

The effects of inadequacies of the structural models have been investigated by Sileny *et al.* (1992), Kravanja *et al.* (1999a). Starting from a double couple mechanism with an instantaneous source time function (δ-pulse) they prove, by synthetic tests, that a poorly known structure, not contained in the allowed interpolation range of the Green function 1) causes mainly the presence of apparent non-double couple components in the moment tensor solutions; 2) contaminates particularly the CLVD that increases from 0% of the starting model to 40%

for large inconsistency cases; 3) maintains the orientation of the double couple stable within ± 10°, and 4) leads to spurious peaks in the source time function (Kravanja *et al.* 1999a). In Fig. 9, modified from Kravanja *et al.* (1999a), the histogram bars are relative to different cases with low (case 1, 2) or high (case 3, 4) perturbation of the starting model for shallow and deep crustal sources. We report, in Fig. 9(b), the mechanism with the error computed at the 95% confidence level only for the worse case with the largest value of CLVD (40%) to statistically evaluate the significance of the findings. Since the hatched area does not include any of the vectors representing the CLVD, the hypothesis of a double couple mechanism is valid at the 95% confidence level.

The robustness of the solution against variations of the structural model can be tested using real data, when different reliable structural models for the studied zone are available. Thus we consider all published structural models for the Etna area (Fig. 6b) and we invert the waveforms of two recorded events of the sequence that preceded the December 1991 eruption. Here we present the inversion results obtained for the event 1990, 27 August (event 3 on the map in Fig. 6a, duration-magnitude 2.6) 15 km deep, since for both events we reach similar conclusions.

We plot the results of three different inversions performed for event 3 using for each case two different structural models one for the source and the other for the receiver. In Fig. 10(a), the structural models used in the inversion are 1-2 (Fig. 6b); in Fig. 10(b) the structural models are 2-3 (Fig. 6b); in Fig. 10(c) we used the model 2-4 (Fig. 6b). The stations used are mapped in Fig. 6(a). Independently of the structural models used, the results show no evident differences. In Fig. 10(d) we report the error computed for the solutions of Fig. 10(b) computed at the 95% confidence level. As solutions we find 62% of double couple 39% of CLVD. The only reliable peak of the source time function is the shaded one (between 0.1-0.3s) whereas the small peaks visible on the tails must be neglected at the 95% confidence level.

4. REAL DATA

The methodology we use to determine the seismic moment tensor has been applied in volcanic and geothermal areas (Campus *et al.* 1993; Panza *et al.* 1993; Kravanja *et al.* 1999b; Saraò *et al.* 2000) as well as in tectonic environments (Radulian *et al.* 1996; Campus *et al.* 1993; Campus & Fäh, 1997; Dufumier *et al.* 1997,

Aoudia *et al.* 2000). In this section we briefly summarize the results obtained in volcanic and geothermal areas where the identification of reliable non-double couple is very important.

4.1 Campi Flegrei and Vesuvio

Phlegraean fields, near Naples (Italy), are periodically affected by bradyseismic activity - slow local movements of the crust in the direction up-down (positive) or down-up (negative) -. Analyses of the seismic moment tensor of some events occurred during the last bradyseismic activity (1984-1986), have been done by Campus *et al.* (1993), Panza *et al.* (1993) and Cespuglio *et al.* (1996). They found that for most of the events there is a dominance of double couple components. The direction and the dip of the fault planes obtained reveal that the compressive axis is always oriented towards the centre of symmetry of the vertical deformation observed during the last period of the bradyseismic activity. This fact seems to confirm that the earthquakes are generated by the same stress-field variation that is responsible for the strain along the pre-fractured areas of the caldera, which represents preferential zones for the dissipation of the increasing stresses.

Non-double couples and particularly strong isotropic components (around 40%) statistically significant at the 95% confidence level, have been found in the most energetic events of the seismicity of Mt. Vesuvius of the last 28 years (De Natale *et al.* 2000).

4.2 Mt. Etna

The temporal evolution of the complete source moment tensor for 28 etnean earthquakes (Fig. 6a) occurred before the outbreak of the 1991-1993 Etna eruption started on 1991 December 15, has been investigated by Saraò *et al.* (2000). Between August 1990-December 1991, the percentage of CLVD (Fig. 11), statistically significant at the 95% confidence level, increases. This fact can be related to fluid movements even if, for some events, the complex interaction between tectonic stress and volcanic activity cannot be excluded. The presence of non-double couple components depicts a process where depressurizing magma body and cracks formation lead to magma injection towards shallower portions of the volcano and agree with the geophysical observations suggesting that the volcanic activity takes place through sequences of emptying and refilling episodes within a reservoir situated a few kilometers below the volcanic edifice. Since the magmas are poor in volatile, CLVDs dominate the etnean seismicity whereas at Mt. Vesuvius, where magmas are rich in volatiles generating explosive mixtures, isotropic components are more relevant (De Natale, 2000)

Even if the percentage of non-double couple components can be affected by some systematic errors due to poor structural modeling, the variation found and the observed trend is free from such a shortcoming (Saraò *et al.* 2000). In Fig. 11 we report the variation in time of the percentage of non-double couple components. Only the values validate by the error analysis are plotted.

Tests described in section 3 testify to the power of the method and the reliability of the results. Therefore, one may conclude that when the time monitoring of the moment tensor components is done on events occurring in the same area (same structural model) recorded by the same network, and using the same methodology, the non-double couple and, even more its variation with time, cannot be attributed simply to modeling effects and explanations must be sought in physical processes acting at the source.

4.3 Larderello

The seismic source mechanisms in the geothermal area of Larderello have been studied considering events with magnitude in the range from 0.5 to 3.5 occurring from 1977 to 1994 (Kravanja *et al.* 1999b). For all the studied events a CLVD component is present but the isotropic part is negligible. The fault plane solutions retrieved agree with the results of previous studies. The non-double couple components can be related to the circulation of fluids in an area with highly fractured rocks saturated with hydrothermal fluids and minerals (Kravanja *et al.* 1999b).

5. CONCLUSIONS

When monitoring volcanic or geothermal activity, the statistical significance of the non-double couple components can be evaluated by the estimation of uncertainties and reliable solutions, related to physical process acting at the source, can be sorted out. In fact, we show with synthetic tests that, by an appropriate error analysis of the results, false non-double couple due to poor station coverage, mislocation of the hypocentre, noise contamination of the data or inadequate structural modeling can be recognized in the moment tensor solution at the 99% confidence level, when using synthetic data, or at the 95% if real data are used. The analysis is even more robust when in the same region the evolution in time of the non-double couple components is investigated.

However since spurious non-double couple components can arise just because of the station configuration, when dealing with real data any inversion must be preceded by synthetic tests to define lower limits above which the non-double couple components found can be considered statistically significant at a certain confidence level.

ACKNOWLEDGMENTS

We are grateful to the Editor, A.F. Gangi and to the two referees E. Wielandt and Y.T. Chen whose criticism helped in improving the manuscript. This study was supported by the italian CNR-GNV (Gruppo Nazionale per la Vulcanologia) 96.00862.PF62, 97.00094.PF62 and 98.00695.PF62 grants, and by MURST-COFINANZIMENTO funds ("Dynamics of the lithosphere: seismicity and deformation in active regions of central Italy - Dynamics of Seismogenic Process"; "The Mesozoic Tethyan lithospheric inheritance in the subduction and collisional processes of the central-eastern Mediterranean - Structure and seismicity of the Adriatic plate lithosphere").

REFERENCES

Aoudia, A., Chimera, G., Costa, G., Nunziata, C., Panza, G.F., Romanelli, F., Saraò, A., Suhadolc, P. & Vaccari, F., 2000. Modelling of the seismic ground motion of the Umbria-Marche sequence (September 1997), *Proceedings of the 12th World Conference on Earthquake Engineering*, Auckland-New Zealand, CD-Rom – paper ID 2500.

Campus, P., Cespuglio, G. & Panza, G.F., 1993. Full moment tensor retrieval and fluid dynamics in volcanic areas: the case of Plegrean Fields (South Italy), *Atti dell'Accademia dei Lincei of the International Conference Large explosive eruptions (The problem of eruptions, forecasting and warning; limits and possibilities)*, 81-101.

Campus, P. & Fäh, D., 1997. Seismic monitoring of explosions: a method to extract information on the isotropic component of the seismic source, *J. Seism.*, 1, 205-218.

Cardaci, C., Coviello, M., Lombardo, G., Patanè, G. & Scarpa, R., 1993. Seismic tomography of Etna Volcano, *J. Volcanol. Geotherm. Res.*, 56, 357-368.

Cespuglio, G., Campus, P. & Sileny, J., 1996. Seismic moment tensor resolution by waveform inversion of few local noisy records-II. Application to Phlaegrean Fields (Southern Italy) volcanic tremors, *Geophys. J. Int.*, 126, 620-634.

De Natale, G., Kuznetzov, I., Kronrod, T., Peresan, A., Saraò, A., Troise, C. & Panza, G.F., 2000. The recent seismic crisis of Mt. Vesuvius in the framework of its past 30 years seismic activity. Submitted to *Geophys. Res. Lett.*

Dufumier, H., Michelini, A., Du, Z., Bondar, I., Sileny, J., Mao, W., Kravanja, S. & Panza, G.F., 1997. Regional Structure Modeling and Source Inversion for the 1992 Roermond Earthquake, *J. Seism., 1*, 321-340.

Ekström, G., Morelli, A., Boschi, E. & Dziewonski, A., 1998. Moment Tensor Analysis of the Central Italy Sequence of September-October 1997, *Geophys. Res. Lett.*, 25, 1971-1974.

Florsch, N., Fäh, D., Suhadolc, P., & Panza, G.F, 1991. Complete Synthetic Seismograms for High-Frequency Multimode SH-waves, *Pure and Appl. Geophys.*, 136, 529-560.

Foulger, G.R., 1988. Hengill triple junction, SW Iceland; Tectonic structure and the spatial and temporal distribution of local earthquakes, *J. Geophys. Res.*, B, 93, 13493-13506.

Fougler, G.R. & Julian, B.R., 1993. Non-double couple earthquakes at the Hengill-Grensdalur Volcanic Complex, Iceland: Are they the artifacts of crustal heterogeneity?, *Bull. Seismol. Soc. Am.*, 83, 38-52.

Hirn, A., Nercessian, A., Sapin, M., Ferrucci, F. & Wittlinger, G., 1991. Seismic heterogeneity of Mt. Etna: structure and activity, *Geophys. J. Int.*, 105, 139-153.

Julian, B.R., Miller, A.D. & Fougler, G.R., 1998. Non-double-couple earthquakes I. Theory, *Rev. Geophys.*, 36, 525-549.

Knopoff, L. & Randall, M., 1970. The compensated linear-vector dipole: A possible mechanism for deep earthquakes, *J. Geophys. Res.*, 75, 4957-4963.

Koch, K., 1991. Moment Tensor Inversion of local earthquake data - I. Investigation of the method and its numerical stability with model calculations, *Geophys. J. Int.*, 106, 305-319

Kravanja, S., Panza, G.F. & Sileny, J., 1999a. Robust retrieval of seismic point source time function, *Geophys. J. Int.*, 136, 385-394

Kravanja, S., Batini, F., Fiordelisi, A. & Panza, G.F., 1999b. Full moment tensor retrieval waveform inversion in the Larderello geothermal area, in press on *Pure and Appl. Geophys.*

Nabelek, J.L., 1984. *Determination of earthquake source parameters from inversion of body waves*, Ph.D. Thesis, Massachusetts Institute of Technology , Cambridge, USA.

Panza, G.F., 1985. Synthetic seismograms: the Rayleigh waves modal summation, *J. Geophys.*, 58, 125-145.

Panza, G.F., Sileny, J., Campus, P., Nicolich, R. & Ranieri, G., 1993. Point source moment tensor retrieval in volcanic, geothermal and orogenic areas by complete waveform inversion, *Int. J. Appl. Geophys.*, 30, 98-118.

Radulian, M., Ardeleanu, L., Campus, P., Sileny, J. & Panza, G.F., 1996. Waveform inversion of weak Vrancea (Romania) earthquakes, *Studia Geoph. Geod.*, 40, 367-380.

Riedesel, M.A. & Jordan, T.H., 1989. Display and assessment of seismic moment tensors, *Bull. Seismol. Soc. Am.*, 79, 85-100.

Saraò, A., Panza, G.F., Privitera, E. & Cocina, O., 2000. Non-double couple mechanisms in the seismicity preceding 1991-1993 Etna volcano eruption, submitted to *Geophys. J. Int.*

Satake, K., 1985. Effects of station coverage on moment tensor inversion, *Bull. Seismol. Soc. Am.*, 75, 1657-1667.

Sileny, J., Panza, G.F. & Campus, P., 1992. Waveform inversion for point source moment tensor retrieval with optimization of hypocentral depth and structural model, *Geophys. J. Int.*, 109, 259-274.

Sileny, J., Campus, P. & Panza, G.F., 1996. Seismic moment tensor resolution by waveform inversion of a few local noisy records-I. Synthetic tests, *Geophys. J. Int.*, 126, 605-619.

Sipkin, S.A., 1982. Estimation of earthquake source parameters by the inversion of waveform data: synthetic waveforms, *Phys. Earth. Planet. Inter.*, 30, 242-259.

Stump, B.W., & Johnson, L.R., 1977. The determination of source properties by the linear inversion of seismograms, *Bull. Seismol. Soc. Am.*, 67, 1489-1502.

FIGURE LEGENDS

Figure 1. Riedesel & Jordan (1989) graphical display of moment tensor solutions and their uncertainties. The vector which describes a general source mechanism is **L** (circle), the vector **d** (square) represent a double couple source mechanism, the CLVD vectors are **l** (triangle pointing downwards when they are in the lower hemisphere and upwards when they are in the upper hemisphere) if the major dipole is directed along the T axis or **l'** (triangle) if it is oriented along the pressure axis, and **i** (diamond) is the vector corresponding to a purely isotropic source. The great circle which connects **d, l** and **l'** on the unit sphere defines the subspace on which L must lie for a purely deviatoric source. Examples of mechanisms without errors: a) is for a pure double couple; b) shows a pure CLVD; c) a deviatoric source; d) a linear combination of double couple, CLVD and isotropic components. Examples of mechanisms with errors plotted as projection of confidence ellipse around P, T, B axes and **L** computed, for the showed case, at the 95% confidence level: e) a pure double couple source mechanism is reliable; f) a pure CLVD is reliable; g) the mechanism is a pure deviatoric ones; h) the isotropic solution is reliable at the 95% of confidence level.

Figure 2. Station configurations adopted to test the influence of the station coverage on the source mechanism. From top to the bottom five, four and three stations - represented on the focal sphere by triangles - are considered in the six configurations (modified after Sileny *et al.* 1996).

Figure 3. Drop in per cent of the principal source components obtained from the inversion of data recorded by the five-station networks. Filled squares correspond to the results obtained using only the vertical component whereas filled triangles represent results obtained with three component stations. The starting mechanisms - **a)** dip slip source; **b)** strike-slip source; **c)** explosive source - used to generate the synthetic data to be inverted are plotted in the corresponding diagrams (modified after Sileny *et al.* 1996).

Figure 4. a) Map view with the station distribution (triangles) around the epicentre (star). **b1)** Fit between "observed data" (solid line) and synthetic signals (dotted line). The epicentral distances are reported on the left whereas the maximum amplitudes and the correlation values are reported on the right; **b2)** comparison between the full (solid line) and the deviatoric (dotted line) MTRFs; **c)** mechanism and corresponding STF retrieved.

Figure 5. a) and **b)** As in Fig. 4(b1), and 4(c) but using a different station distribution. The stations used can be read on the left of the data fit plot and are mapped in Fig. 4(a).

Figure 6. a) Map with the stations (black circles) used by Saraò *et al.* (2000) for their study. The star represents the location of the event considered in the synthetic test. The circles are the 28 earthquakes analyzed by Saraò *et al.* (2000); **b)** examples of the structural models available in the literature, used in the inversion performed to test the robustness of the solutions. The Istituto Internazionale di Vulcanologia of Catania (private communication) has provided the structural model I.I.V. The model "Nicolich 1997" comes from Nicolich, private communication.

Figure 7. a1) Fit between "observed" data (solid line) and synthetic (dotted line) are plotted. The epicentral distances are reported on the left whereas the maximum amplitudes and the correlation values are reported on the right; **a2)** comparison between full (solid line) and deviatoric (dotted line) MTRFs. **c)** mechanism and STF retrieved.

Figure 8. Mechanisms with plot of the 95% confidence ellipses around T, B, and P and **L** and STF determined by the inversion of noisy data. The level of noise added is reported on the right. The reliable STF is given by the shaded area (modified after Sileny *et al.* 1996).

Figure 9. a) Variation of percentages of double couple (DC), CLVD and isotropic (V) obtained as a result of the inversion after introducing some perturbation in the structural model with respect to the model used to compute the synthetic "observed" data. In *Case 1* small inconsistency and shallow source; *Case 2* small inconsistency and deep source; *Case 3* large inconsistency and shallow source; *Case 4* large inconsistency, deep source (modified after Kravanja *et al.* 1999a). **b)** The mechanism with the error analysis is reported only for the case with the larger amount of CLVD. The **L** error ellipse at the 95% confidence level is on the top of the **d** vector, i.e. the CLVD found is not reliable.

Figure 10. Results obtained using the different structural models reported in Fig. 6(b). The waveform fit (bold line for real data, dotted line for synthetics), the MTRF (full and deviatoric) fit, the mechanism and the STF are reported for the test made using the structural models 1-2 **(a)**, 2-3 **(b)**, 2-4 **(c)**; **d)** the source mechanism obtained for case b) with errors .

Figure 11. Variation with time of the percentage of CLVD (squares) and V (stars) components for Mt. Etna (modified from Saraò *et al.* 2000). Only the values convalidated by the error analysis are plotted. the numbers correspond to the epicenters of Fig. 6a.

Fig. 1

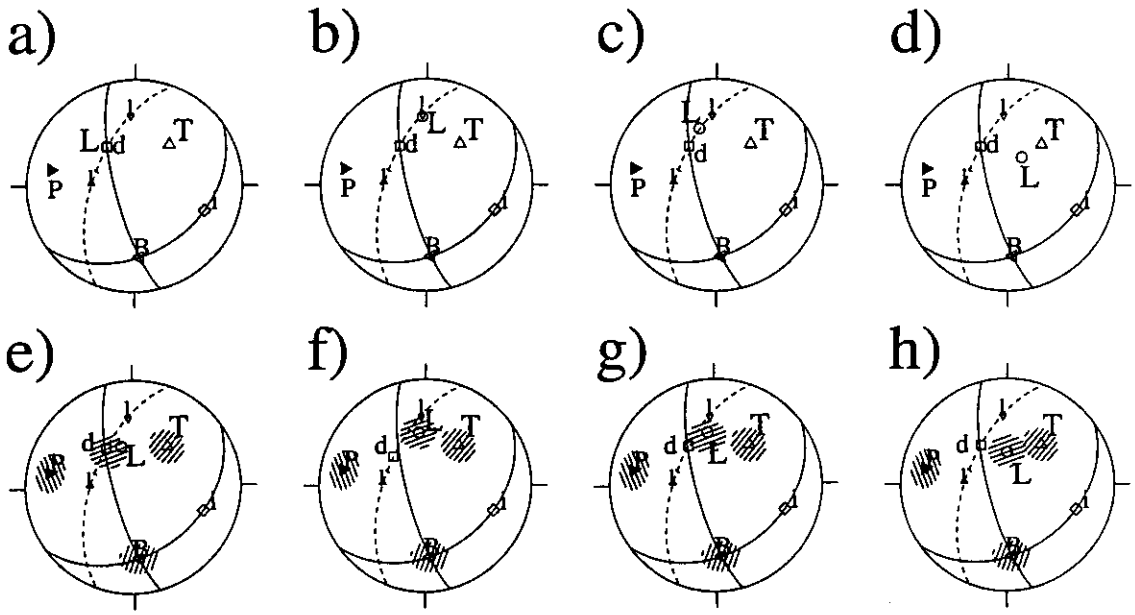

Fig. 2

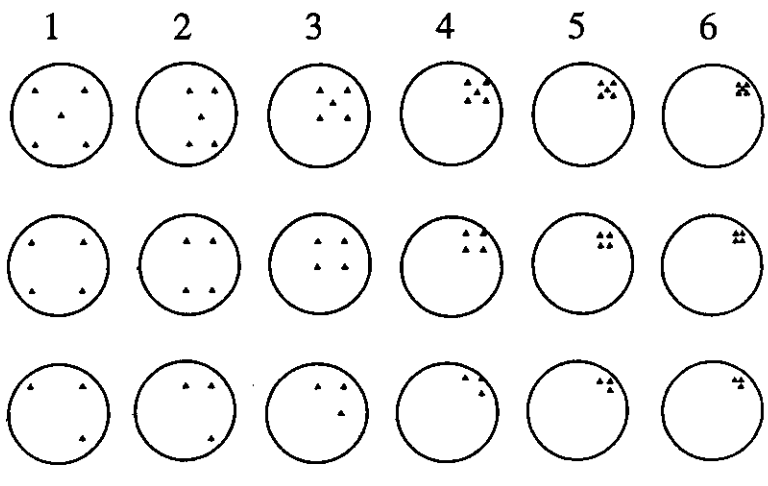

Configurations

Fig. 3

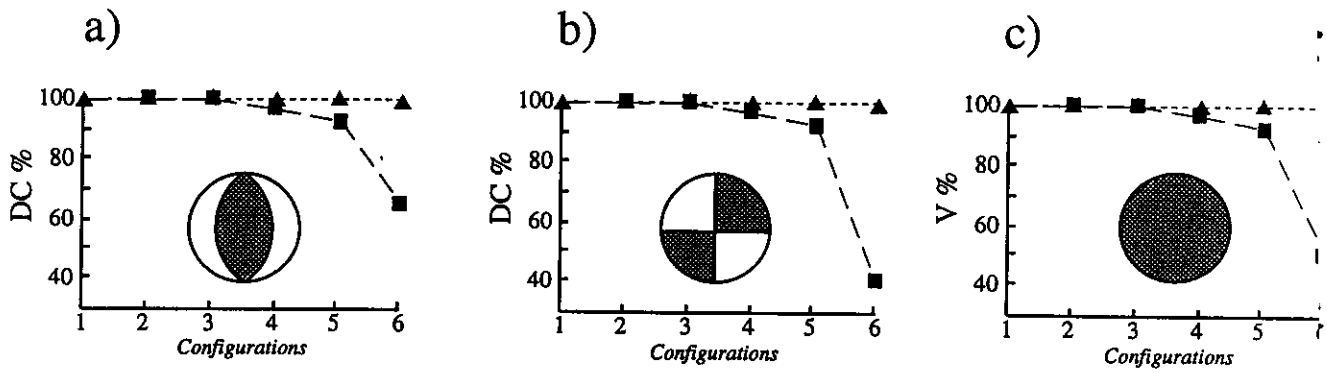

Figure 4

a)

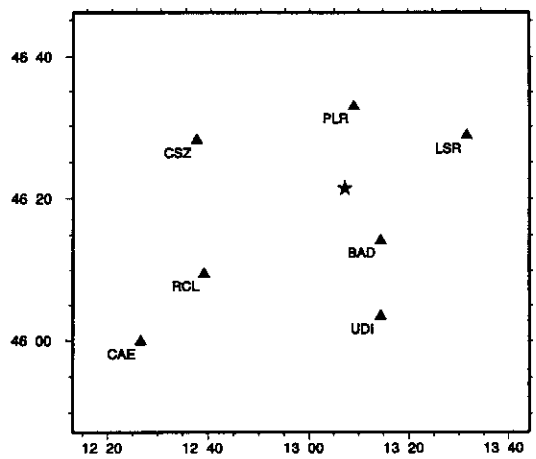

b1)

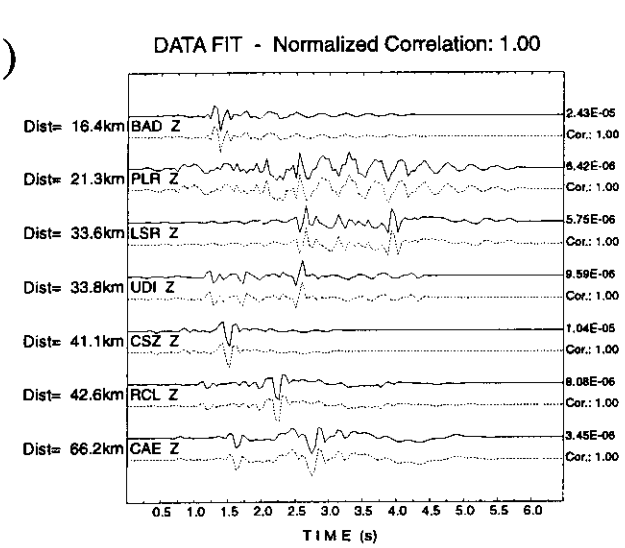

b2)

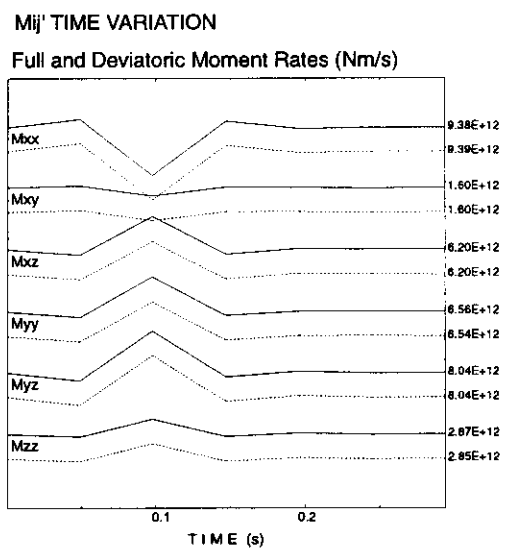

c)

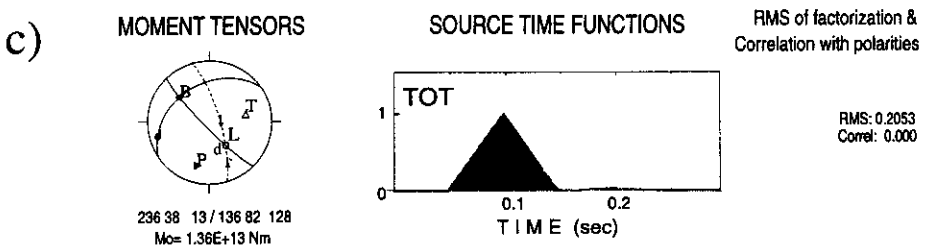

Figure 5

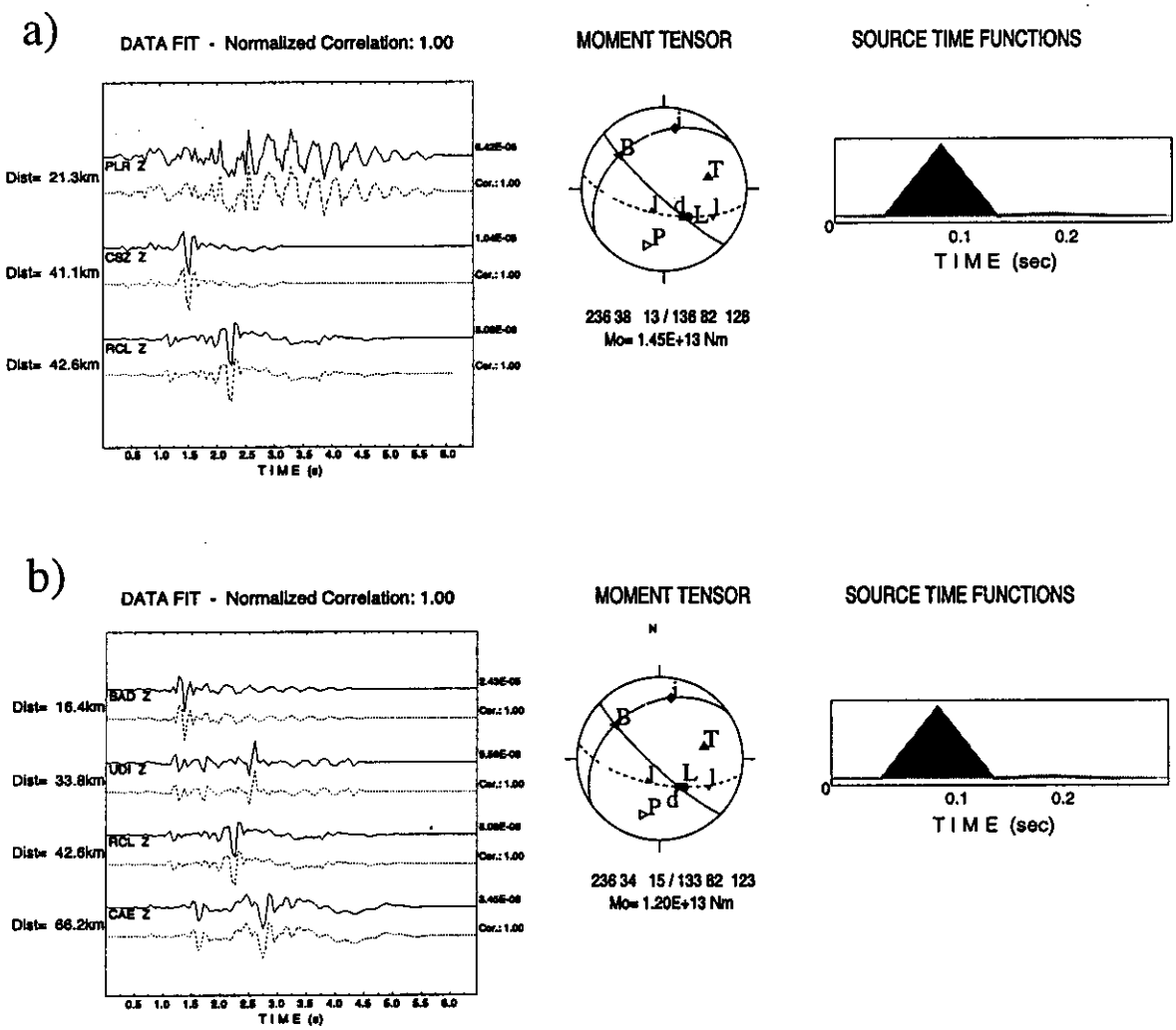
a)
DATA FIT - Normalized Correlation: 1.00
MOMENT TENSOR
SOURCE TIME FUNCTIONS
Dist= 21.3km
PLR Z
Cor.: 1.00
Dist= 41.1km
CSZ Z
Cor.: 1.00
Dist= 42.6km
RCL Z
Cor.: 1.00
0.5 1.0 1.5 2.0 2.5 3.0 3.5 4.0 4.5 5.0 5.5 6.0
TIME (s)
B
T
P
236 38 13 / 136 82 128
Mo= 1.45E+13 Nm
0
0.1
0.2
TIME (sec)
b)
DATA FIT - Normalized Correlation: 1.00
MOMENT TENSOR
SOURCE TIME FUNCTIONS
Dist= 16.4km
BAD Z
Cor.: 1.00
Dist= 33.8km
UOI Z
Cor.: 1.00
Dist= 42.6km
RCL Z
Cor.: 1.00
Dist= 66.2km
CAE Z
Cor.: 1.00
0.5 1.0 1.5 2.0 2.5 3.0 3.5 4.0 4.5 5.0 5.5 6.0
TIME (s)
N
B
T
P
236 34 15 / 133 82 123
Mo= 1.20E+13 Nm
0
0.1
0.2
TIME (sec)

Figure 6

a)

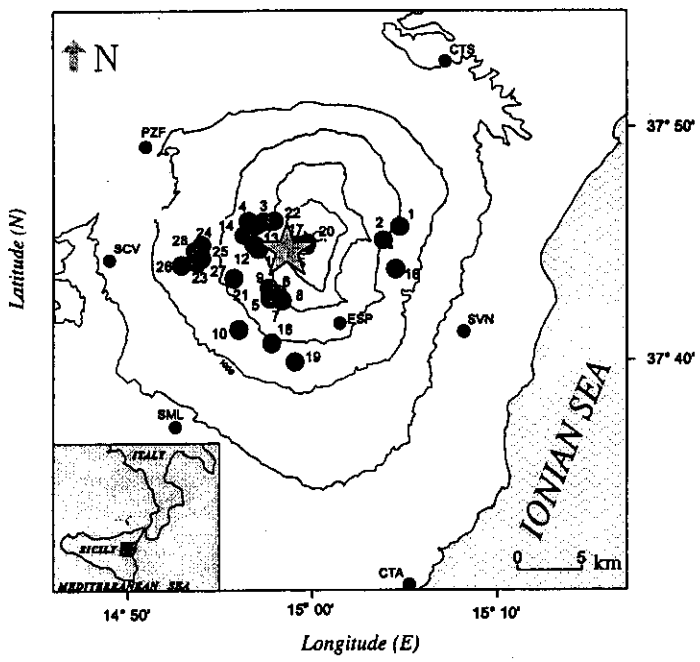
N
CTS
PZF
SCV
ESP
SVN
SML
CTA
IONIAN SEA
0 5 km
37° 50'
37° 40'
14° 50'
15° 00'
15° 10'
Latitude (N)
Longitude (E)

b)

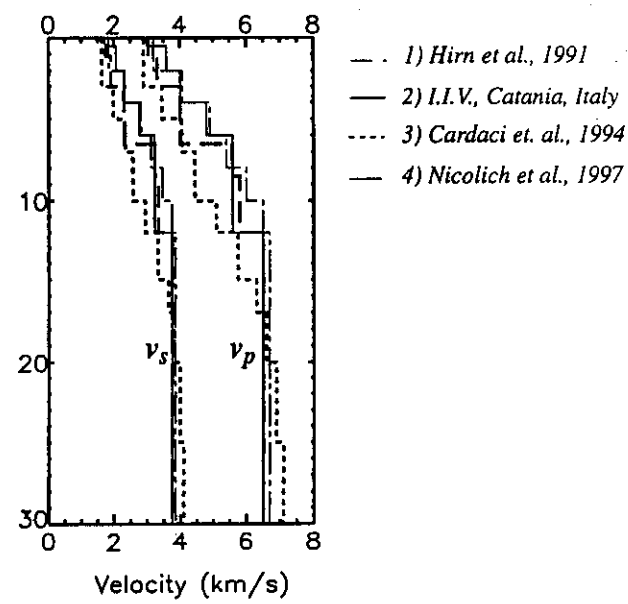
0 2 4 6 8
10
20
30
v_s
v_p
Velocity (km/s)
1) Hirn et al., 1991
2) I.I.V., Catania, Italy
3) Cardaci et. al., 1994
4) Nicolich et al., 1997

Figure 7

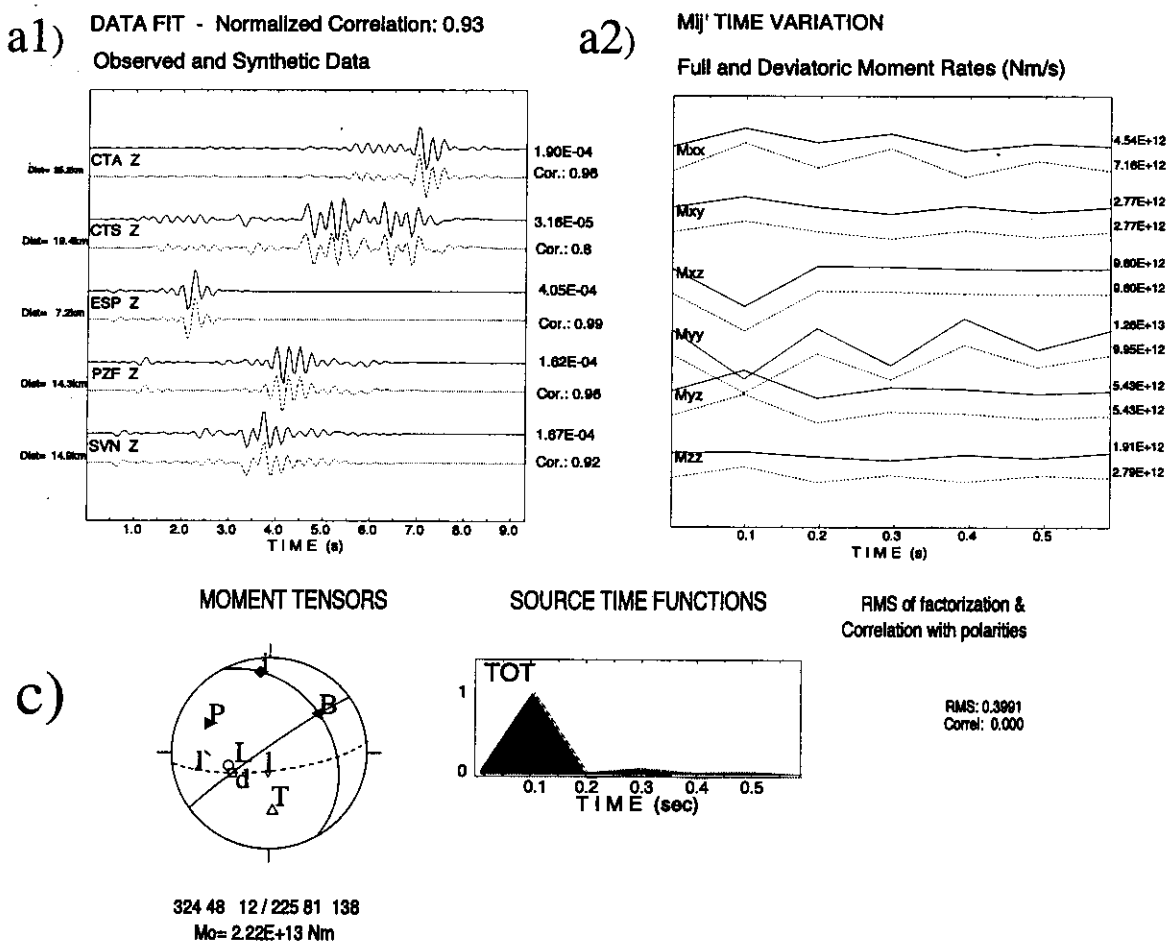
a1)
DATA FIT - Normalized Correlation: 0.93
Observed and Synthetic Data
CTA Z
1.90E-04
Cor.: 0.96
CTS Z
3.16E-05
Cor.: 0.8
ESP Z
4.05E-04
Cor.: 0.99
PZF Z
1.62E-04
Cor.: 0.96
SVN Z
1.67E-04
Cor.: 0.92
1.0 2.0 3.0 4.0 5.0 6.0 7.0 8.0 9.0
TIME (s)
a2)
Mij' TIME VARIATION
Full and Deviatoric Moment Rates (Nm/s)
Mxx
4.54E+12
7.16E+12
Mxy
2.77E+12
2.77E+12
Mxz
9.80E+12
9.80E+12
Myy
1.26E+13
9.95E+12
Myz
5.43E+12
5.43E+12
Mzz
1.91E+12
2.79E+12
0.1 0.2 0.3 0.4 0.5
TIME (s)
c)
MOMENT TENSORS
SOURCE TIME FUNCTIONS
RMS of factorization &
Correlation with polarities
P
B
T
TOT
1
0
0.1 0.2 0.3 0.4 0.5
TIME (sec)
RMS: 0.3991
Correl: 0.000
324 48 12 / 225 81 138
Mo= 2.22E+13 Nm

Figure 8

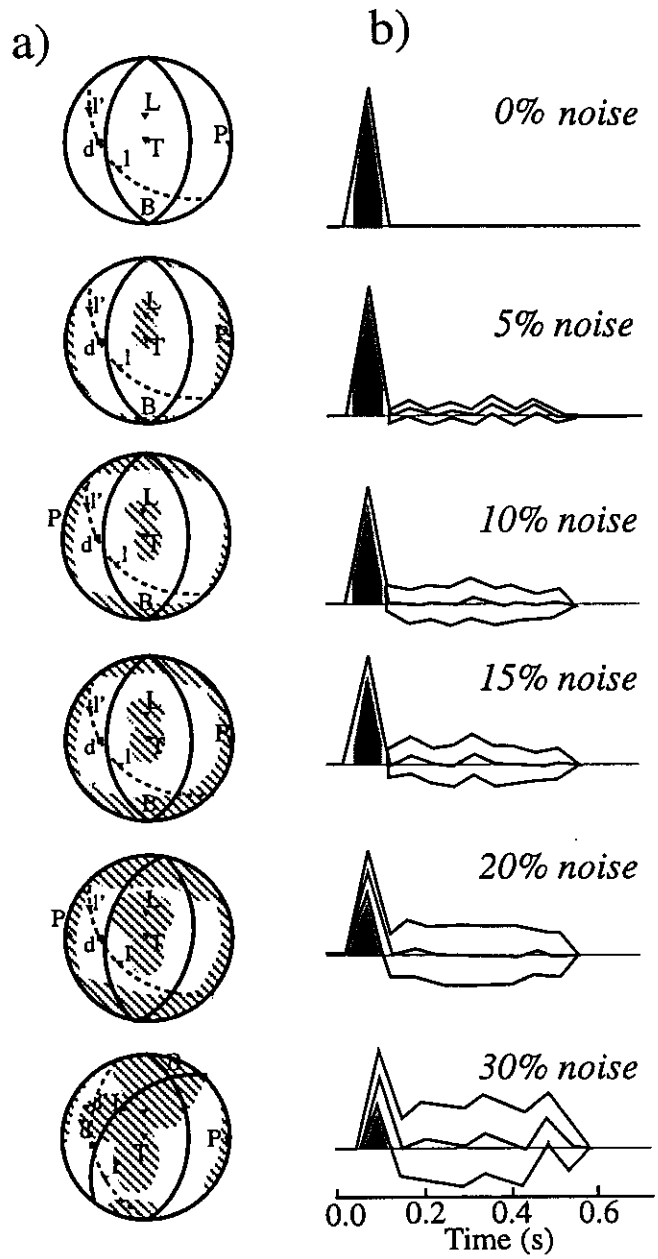
a)
b)
0% noise
5% noise
10% noise
15% noise
20% noise
30% noise
0.0
0.2
0.4
0.6
Time (s)

Figure 9

a)

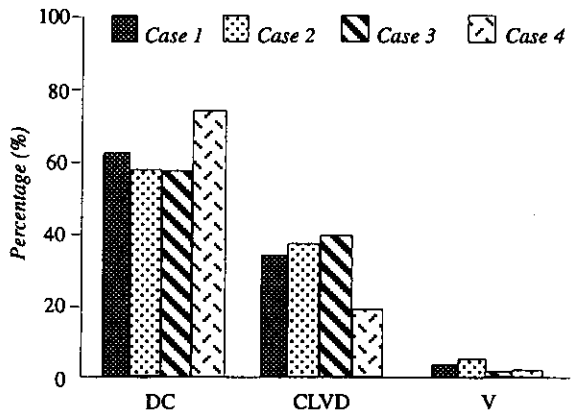
Case 1
Case 2
Case 3
Case 4
Percentage (%)
100
80
60
40
20
0
DC
CLVD
V

b)

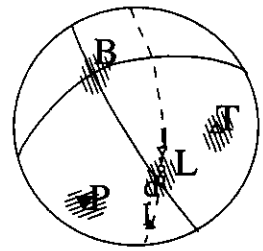
B
T
L
P

Figure 10

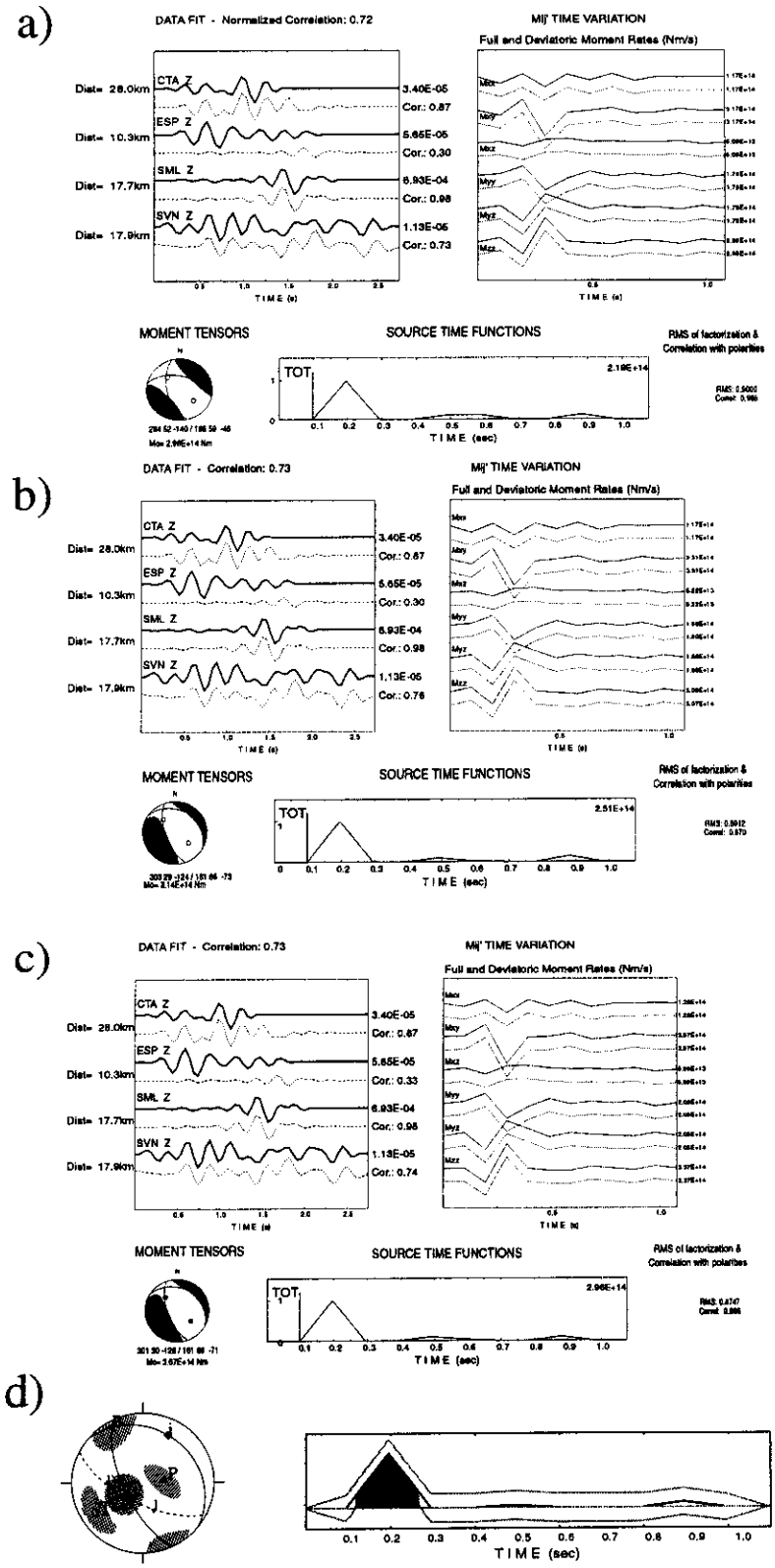
a)
DATA FIT - Normalized Correlation: 0.72
Mij' TIME VARIATION
Full and Deviatoric Moment Rates (Nm/s)
CTA Z
ESP Z
SML Z
SVN Z
Dist= 28.0km
Dist= 10.3km
Dist= 17.7km
Dist= 17.9km
3.40E-05
Cor.: 0.87
5.65E-05
Cor.: 0.30
6.93E-04
Cor.: 0.98
1.13E-05
Cor.: 0.73
TIME (s)
MOMENT TENSORS
SOURCE TIME FUNCTIONS
RMS of factorization &
Correlation with polarities
TOT
2.19E+14
TIME (sec)
b)
DATA FIT - Correlation: 0.73
Mij' TIME VARIATION
Full and Deviatoric Moment Rates (Nm/s)
CTA Z
ESP Z
SML Z
SVN Z
Dist= 28.0km
Dist= 10.3km
Dist= 17.7km
Dist= 17.9km
3.40E-05
Cor.: 0.87
5.65E-05
Cor.: 0.30
6.93E-04
Cor.: 0.98
1.13E-05
Cor.: 0.76
TIME (s)
MOMENT TENSORS
SOURCE TIME FUNCTIONS
RMS of factorization &
Correlation with polarities
TOT
2.51E+14
TIME (sec)
c)
DATA FIT - Correlation: 0.73
Mij' TIME VARIATION
Full and Deviatoric Moment Rates (Nm/s)
CTA Z
ESP Z
SML Z
SVN Z
Dist= 28.0km
Dist= 10.3km
Dist= 17.7km
Dist= 17.9km
3.40E-05
Cor.: 0.87
5.65E-05
Cor.: 0.33
6.93E-04
Cor.: 0.98
1.13E-05
Cor.: 0.74
TIME (s)
MOMENT TENSORS
SOURCE TIME FUNCTIONS
RMS of factorization &
Correlation with polarities
TOT
2.96E+14
TIME (sec)
d)
P
T
J
0.1
0.2
0.3
0.4
0.5
0.6
0.7
0.8
0.9
1.0
TIME (sec)

Fig. 11

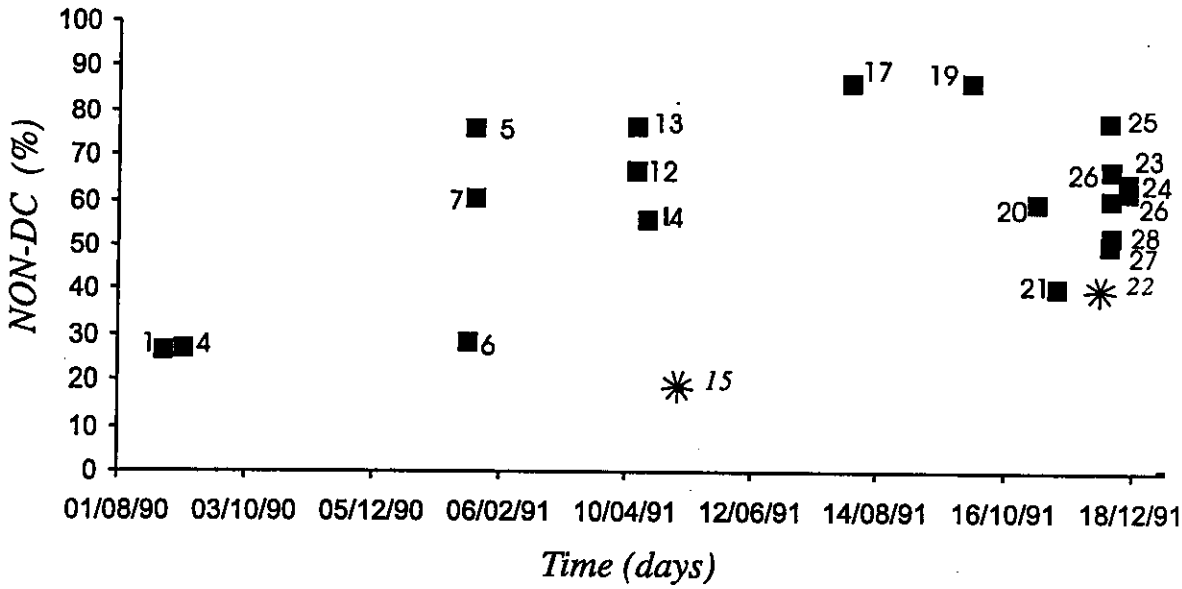
NON-DC (%)
100
90
80
70
60
50
40
30
20
10
0
01/08/90
03/10/90
05/12/90
06/02/91
10/04/91
12/06/91
14/08/91
16/10/91
18/12/91
Time (days)
1
4
5
6
7
12
13
14
15
17
19
20
21
22
23
24
25
26
26
27
28

JOURNAL OF GEOPHYSICAL RESEARCH, VOL. 101, NO. B3, PAGES 5725–5738, MARCH 10, 1996

On the inverse problem for earthquake rupture: The Haskell-type source model

S. Das

Department of Earth Sciences, University of Oxford, Oxford, England

P. Suhadolc

Istituto di Geodesia e Geofisica, Universita di Trieste, Trieste, Italy

Abstract. In order to gain insight into how to invert seismograms correctly to estimate the details of the earthquake rupturing process, we perform numerical experiments using artificial data, generated for an idealized faulting model with a very simple rupture and moment release history, and solve the inverse problem using standard widely used inversion methods. We construct synthetic accelerograms in the vicinity of an earthquake for a discrete analog of the Haskell-type rupture model with a prescribed rupture velocity in a layered medium. A constant level of moment is released as the rupture front passes by. We show that using physically based constraints, such as not permitting back slip on the fault, allow us to reproduce many aspects of the solution correctly, whereas the minimum norm solution or the solution with the smallest first differences of moment rates in space and time do not reproduce many aspects for the cases studied here. With the positivity of moment rate constraint, as long as the rupturing area is allowed to be larger than that in the forward problem, it is correctly found for the simple faulting model considered in this paper, provided that the rupture velocity and the Earth structure are known. If, however, the rupture front is constrained either to propagate more slowly or the rupturing area is taken smaller than that in the forward problem, we find that we are unable even to fit the accelerograms well. Use of incorrect crustal structure in the source region also leads to poor fitting of the data. In this case, the proper rupture front is not obtained, but instead a "ghost front" is found behind the correct rupture front and demonstrates how the incorrect crustal structure is transformed into an artifact in the solution. The positions of the centroids of the moment release in time and space are generally correctly obtained.

Introduction

With the deployment of high dynamic range, broad band digitally recording seismometers, and the availability of supercomputers, it has become feasible to consider the problem of inverting seismograms to obtain the details of the moment release time history and distribution on earthquake faults. The solution of this problem is important for the following reasons. Since the moment release on faults is generally expected to be nonuniform, one can identify regions of high and low moment release, or slip deficit. The slip or moment distribution obtained from such inversions can be used to infer the stress drop distribution due to the earthquake [e.g., *Miyatake*, 1992] that in turn can be used to estimate stress accumulation on faults. The slip deficit as well as the stress accumulation history on the fault can then lead to inferences about the times of future earthquakes on the fault. An example where a portion of a fault with slip deficit in one earthquake ruptured relatively soon afterwards in another earthquake is the 1986 Andreanof Islands earthquake [*Das*, 1990]. The rupture zone of the Andreanof Islands earthquake was contained entirely within that of the 1957 Aleutian earthquake ($M_w = 8.6$), yet the 1986 earthquake of $M_w = 8.0$ occurred only 29 years later on a plate boundary that is believed to have a much larger characteristic repeat time. Noting that the region of major moment release in the 1986 earthquake coincided with the region of the 1957 event that had essentially no aftershocks, *Das* [1990] identified the 1986 earthquake to be due to the slip deficit left after the 1957 event. Another situation in which the inverse problem solution is useful is when one can relate the variations in moment release on the fault to the morphology, say jogs or bends, or cross-cutting physical features on faults, and so on. Such understanding can lead in the long term to successful prediction of the expected ground motion at particular sites of special interest, say, the locations of critical structures such as power plants, dams, bridges, etc., in regions where large earthquakes are expected. Finally, once the motion on the fault is reconstructed, the entire displacement field can be found by solving the appropriate

Paper number 95JB03533.
0148-0227/96/95JB-03533$05.00

forward problem. This makes it possible to estimate the motion at some site where there is damage but where there was no seismometer [e.g., *Suhadolc et al.*, 1990], thus enabling the cause of the damage, for example, focusing of waves on the site, to be investigated.

The inverse problem for the earthquake source was first formulated by *Kostrov* [1970], and discussed by *Kostrov* [1975] and by *Kostrov and Das* [1988]. Of the numerous studies that estimate the rupture and moment release history during earthquakes, we mention here the papers that develop a new method, or extend an existing method of inversion for both the spatial and temporal moment release pattern on the fault. These include *Olson and Apsel* [1982], *Kikuchi and Kanamori* [1982], *Hartzell and Heaton* [1983], *Kikuchi and Fukao* [1985], *Beroza and Spudich* [1988], *Mendoza and Hartzell* [1988a, 1988b, 1989], *Olson and Anderson* [1988], *Das and Kostrov*, [1990, 1994], *Hartzell et al.* [1991], and *Hartzell and Liu* [1995].

The limitations of such inversions have, however, not yet been studied sufficiently. For example, how close is the solution of this problem, which is well known to be unstable, to the actual moment distribution? How does poor knowledge of crustal structure in the source region affect the estimate of the rupture front location and speed? Since such inversions are not unique, what methods can one use to choose the "correct" solution from among the multiplicity of solutions? The last question cannot, in fact, be answered when working with real data, since the actual moment release at the depths where earthquakes occur is unknowable. In their studies of the great 1986 Andreanof Islands earthquake and the great 1989 Macquarie Ridge earthquake, *Das and Kostrov* [1990, 1994] attempted, using teleseismic data, to choose solutions from among the many possible ones. They demonstrated that more than one slip distribution can fit the data equally well. For the Macquarie Ridge earthquake, alternative slip distributions that could be interpreted as due to a propagating crack or to isolated asperities rupturing fit the data. The different rupture models would clearly lead to different stress accumulation patterns and histories on the fault [*Ruff*, 1983].

In geophysical inverse problems, the solution is often stabilized by using nonphysical prior bounds, such as finding the minimum norm solution or the smoothest solution. *Hartzell and Heaton* [1983] and *Das and Kostrov* [1990,1994] investigated physically based constraints that can be used to stabilize the solutions. We shall show that physical constraints, such as not allowing back slip on the fault, produce the proper results, whereas the minimum norm solution and the solution with the smallest first differences do not, for the cases studied in this paper. *Hartzell and Heaton* [1983], *Mendoza and Hartzell* [1988a, 1988b, 1989], *Hartzell et al.* [1991], and *Hartzell and Liu* [1995] have used various stabilizing bounds in their inverse problem solutions and *Hartzell and Liu* [1995] summarize many features of such prior bounds.

In this paper we shall address only some specific aspects of the questions raised above by using artificial data where we do know what the correct solution is. We shall use the vertical components of synthetic accelerograms constructed using the "far-field" approximation in the vicinity of the earthquake epicenter for source receiver distances in the 15 to 35 km range, generated by a very idealized model of earthquake rupture. We shall take the fault rupture model to be a Haskell-type dislocation [*Haskell*, 1964, 1966, 1969] propagating at a constant rupture velocity. This model has the great advantage of being very simple and has been widely used in seismic source studies, both for the forward problem and for the inverse problem. *Madariaga* [1978] proved that it is an appropriate model for simulating radiation with wavelengths longer than the fault width, as in this paper. Some of the studies of the inverse problem referred to above use essentially this model. We therefore use this simple model to obtain insight into the inverse problem. In this study we confine ourselves to using accurate data and seismograms close to the earthquake source. We do not discuss the teleseismic problem, although some of the results could be adapted to that case by scaling of the fault size and wave periods used here. Neither do we discuss the effects of noise in the data. Rather, we aim to gain insight into the basic problem of solving such unstable inverse problems by studying a very simple and idealized situation. Most importantly, working with synthetic data provides the possibility of identifying artifacts of the solution and their causes.

We first set out briefly the method used to generate the synthetic ground motion data. We next describe the inverse solution method, generate many sets of synthetic data for different faulting models, invert them, and present the results. Finally, we examine the limitations of the inverse problem for earthquake faulting, identifying, for example, which source properties we might be able to infer reliably, which ones depend strongly on knowledge of proper crustal structure, and so on.

Description of the Mathematical Problem

The formulation of the problem in terms of the slip rate or slip on the fault is well known and is stated only briefly here. Using the representation theorem (e.g., equation (3.2) of *Aki and Richards* [1980]; equation (3.2.18) of *Kostrov and Das* [1988]) and neglecting body forces, the displacement record at a station located at point $\mathbf{x}_1$ on the Earth's surface can be expressed in terms of the slip distribution over a fault surface, Σ, as an integral equation of the first kind [*Das and Kostrov*, 1990]

$$u_k(\mathbf{x}_1, t_1) = \int_0^{t_1} dt \iint_\Sigma K_{ik}(\mathbf{x}_1, \mathbf{y}_1, t_1, t) a_i(\mathbf{y}_1, t) dS, \quad (1)$$

where $i, k = 1, 2, 3$, $u_k(\mathbf{x}_1, t_1)$ are the components of the displacement vector, $a_i(\mathbf{y}_1, t)$ are the components of the slip, and $K_{ik}(\mathbf{x}_1, \mathbf{y}_1, t_1, t)$ are the components of the impulse response of the medium at $(\mathbf{x}_1, t_1)$, due to a dislocation point source at $(\mathbf{y}_1, t)$. By moving the time derivative that exists in the kernel K to the slip term in (1), we obtain an equivalent representation in terms of the slip-rate distribution over the fault, with the corresponding kernel G. In short,

$$\mathbf{u} = K * \mathbf{a} = G * \dot{\mathbf{a}}, \text{ where } K = \dot{G} \quad (2)$$

where $\mathbf{u}$ is the displacement vector, $\mathbf{a}$ and $\dot{\mathbf{a}}$ are the slip and slip rate vectors, respectively, asterisk denotes convolution over the fault area and source duration, and dot denotes time derivative. We shall assume that the fault is planar and that the slip direction is constant over the fault. We can use either form of (2) to find slip or slip rate, if we know the kernels K and G and the displacement seismograms. Slip rate is easily converted into moment rate given the modulus of rigidity.

Discretizing the problem, by dividing the fault into square cells and the source time function into steps, reduces (2) to the system of equations

$$A\mathbf{x} \approx \mathbf{b}, \quad (3)$$

where A is the matrix obtained by integrating G or K over fault cells and time steps, each column of A being the appropriate discretized set of the kernel for all stations corresponding to different cells and time instants, ordered in the same way as the observations $\mathbf{b}$, and $\mathbf{x}$ are the unknown slips or slip rates. In this paper, we use the formulation in terms of the slip rates and the kernel G.

The Green functions are determined using the multimodal summation method for a layered, anelastic medium [*Panza*, 1985; *Panza and Suhadolc*, 1987; *Florsch et al.*, 1991]. In this paper we shall only use the vertical component of motion and Rayleigh wave modal summation to determine the Green function kernel. We have chosen to work initially with the vertical component only to make the matrix A smaller, for a given number of stations. The effect of including the horizontal component on the inversion will be investigated in the future.

The medium consists of homogeneous layers separated by first-order discontinuities. The modal summation method allows exact and complete solution of the full wave equation for a laterally homogeneous medium in a preassigned (ω,c) interval, where ω is the angular frequency, and c is the phase velocity [e.g. *Aki and Richards*, 1980]. The seismic source is included in the computations using the formulation due to *Harkrider* [1964] and *Ben-Menahem and Harkrider* [1964]. The extended fault is modeled as a grid of point sources, and the synthetic seismogram at each station due to the moment release on the fault is computed by summing the contributions from each point source with appropriate delays and weights [*Panza and Suhadolc*, 1987].

In this paper the Green functions are computed for a maximum frequency of 1 Hz. The frequency domain is sampled with 200 points in the range DC to 1 Hz, which gives a frequency step of 0.005 Hz, yielding good frequency resolution between 0.1 Hz and 1 Hz. The upper frequency of 1 Hz implies minimum wavelengths on the order of 1 km for the velocity models considered in this paper. The achievable spatial resolution on the fault at a given instant of time is on the order of 0.5 km. The size of the time step used in constructing the Green functions is taken as about 0.1 s (more precisely as 200/2048=0.09765 s, where 200 is the number of points in the frequency domain and 2048 is the number of points in the discrete Fourier transform).

Construction of the Synthetic Data

The synthetic accelerograms to be used in the inversion are constructed by performing the convolution in (2) for the particular faulting models considered. In this study the forward problem is a discretized form of the Haskell dislocation propagating unilaterally over a rectangular fault at a constant rupture velocity, $v_r = 0.7v_S$, where v_S is the shear wave speed in the medium. Figure 1 shows the fault geometry together with a schematic diagram of the propagating rupture. The fault is taken to be of pure dip-slip type with a 30° dip and with the top of the fault located at a depth of 1 km below the Earth's surface.

The discrete approximation (3), of equation (1), must be fine enough to be a good approximation to the integral in (1), must be representative for the wave lengths involved in the data, and yet be feasible to solve. The spatial cell size Δx

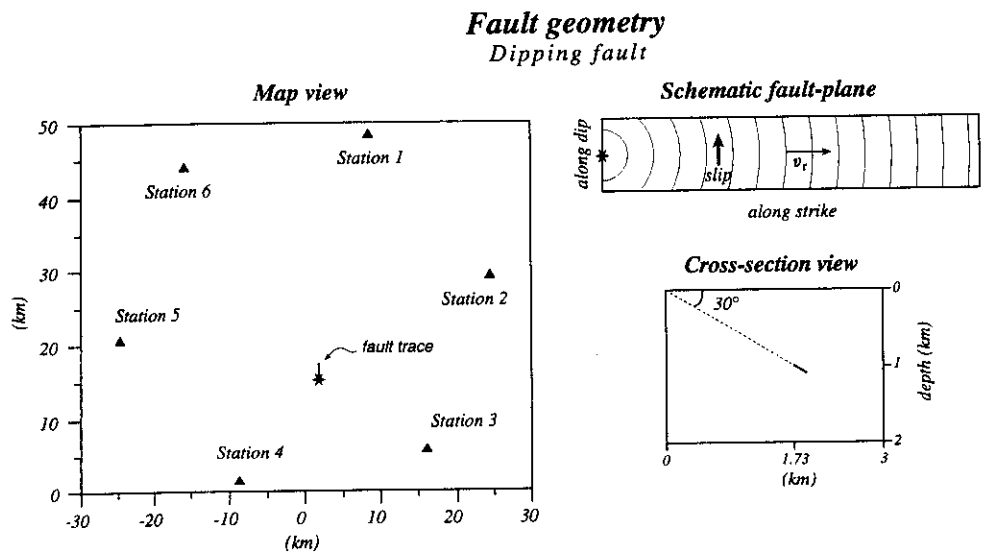

Figure 1. Fault and station geometry.

Table 1. Summary of Inversion Method, Parameters, and Results

Case	Source Medium (inv)	Faulting Parameters: Top of Fault (inv, km)	nh (fwd)	nh (inv)	nt (fwd)	nt (inv)	Centroid[a] in time (fwd)	Constraints Used	Inversion Method	Centroid[a] in Time (inv)	Centroid[b] Along Strike (inv)	Remarks
1a	$M1$	1	1	1	21	21	10.5	$R1(0.7v_S)$,MTO	SVD	10.6	26.0	Only total moment correctly reproduced
(2)	$M1$	1	1	1	21	21	10.5	$R1(0.7v_S)$,MTO,P	LP	10.5	25.5	Entire solution correctly reproduced
1b	$M1$	1	1	1	21	21	10.5	$R2$,MTO	SVD	10.6	26.0	Same as case 1a
(2)	$M1$	1	1	1	21	21	10.5	$R2$,MTO,P	LP	10.5	25.5	Entire solution reproduced
1c	$M1$	1	1	1	21	21	10.5	$R1(0.5v_S)$,MTO,P	LP	9.8	17.3	Poor solution
1d	$M1$	1	1	1	21	21	10.5	$R1(0.5v_S)$,MTO,P,M	LP	9.9	17.3	""
2a	$M1$	1	1	5	21	21	10.5	$R1(0.7v_S)$,P	LP	10.6	26.0	Some aspects of solution correct
(2)	$M1$	1	1	5	21	21	10.5	$R1(0.7v_S)$,P,MTO	LP	10.4	25.5	Entire solution correctly reproduced
2b	$M1$	1	5	1	21	21	10.5	$R1(0.7v_S)$	LP	10.9	26.2	Some aspects of solution correct
(2)	$M1$	1	5	1	21	21	10.5	$R2$	LP	10.3	23.9	Rupture front correctly found
3a	$M2$	2.05	1	1	21	38	10.5	$R2$,MTO,P	LP	20.3	24.3	Poor solution
3b	$M2$	2.05	1	5	21	38	10.5	$R2$,MTO,P	LP	11.1	20.3	""

$nx = 51$; $\Delta x = 50m$; $\Delta t = 0.097..s$ in all forward (fwd) and inverse (inv) cases.
FORWARD PROBLEM: Centroid along strike, measured from hypocenter/Δx=25.5; source in medium $M1$.
[a]Time centroid is $/\Delta t$. [b]Centroid along strike is $/\Delta x$.
MTO is "more than once".
For meaning of other constraints, see text.

on the fault is taken as 50 m and the time step size Δt in the source time function as approximately 0.1 s, both for the forward and inverse problems. The rupture front is discretized using the same spatial and temporal gridding, with the moment being released at the center of each cell and in the middle of each time step as the rupture front crosses any portion on the cell within the time step interval. The moment is released only once in each cell, at the time the cell ruptures. The level of moment released at each cell is taken as constant and equal to 1 x 10^{11} N m. The problem using finer discretization in the forward than in the inverse problem is the subject of another paper [*Das et al.*, 1995].

The size of the fault varies in the different cases considered here. Table 1 summarizes the length and width of the rupture area for each case. Figure 2 shows velocity profiles with depth for the Earth structures $M1$ and $M2$ that we shall use in this study. $M1$ has a low velocity layer that is absent in $M2$. The Q values in the two models range from a value of 20 in the surficial layers to 100 in the deep sediments and 400 beneath them. The six stations, distributed equally in azimuth around the fault (Figure 1), are chosen so as not to involve nodal directions. The hypocenter is marked by a star and the source receiver distances lie in the 15 to 35 km range. All the synthetic accelerograms are sampled at the same time interval as the time step size used to construct the Green function, about 0.1 s, and the entire accelerogram is used in the inversion.

Solution of the Inverse Problem

Since the integral equation (1) is unstable, we need to stabilize it by the use of additional constraints. *Olson and Apsel* [1982], *Hartzell and Heaton* [1983], *Das and Kostrov* [1990, 1994], and *Hartzell and Liu* [1995], among others, have identified constraints that can be used for this purpose. The physically based constraints we shall use in this paper are as follows:

1. Slip rate $\mathbf{x} \geq 0$ for all points on the fault for all time ("positivity" constraint P).
2. The final moment must equal some preassigned value ("moment" constraint M).
3. The rupture is constrained to move at, or more slowly than, some preassigned speed ("strong causality" constraint $R1$). It is important to point out that there is no rupture criterion involved in the discrete inverse problem, and by "rupture speed" we mean the rupture speed of some (unspecified) rupture triggering signal.
4. The moment rate is zero in any cell and time step that would produce a signal before the first arrival at any station from the hypocentral cell ("weak causality" constraint $R2$). In the case when there is insufficient station coverage, if this constraint is used without the constraint $R1$ also being enforced, the inversion may permit super P "rupture speeds".
5. In the forward problem, moment is released only once as the cell breaks. In the inverse problem, a cell may be allowed to release moment more than once. The phrase 'more than once' (MTO) will be used to denote this case.

We select constraints for the different cases studied (Table 1) in order to to gain insight into the effects on the solution of the constraints. Constraints of this type have been called "hard prior bounds" by *Jackson* [1979] and *Backus* [1988].

In addition, it is possible to improve the stability of the problem by the use of "soft prior bounds", such as finding the solution with the minimum norm or the smoothest solution in some sense, say, the solution with the smallest first differences. This is done by adding a term to the penalty functional $||\mathbf{b} - A\mathbf{x}||_p$, where $p = 1, 2, ...$, as desired. For example, to obtain the minimum norm solution, one then minimizes $||\mathbf{b} - A\mathbf{x}||_p + \eta||\mathbf{x}||_p$, where η is some weighting factor. To find the solution with the smallest first difference (in space and/or time), one minimizes $||\mathbf{b} - A\mathbf{x}||_p + \eta$ times the chosen norm of the appropriate first differences of $\mathbf{x}$, and so on. Such stabilizations have been used in the papers on inverse problem solution referred to earlier.

To solve the constrained linear system (3), we shall use two standard methods, discussed by *Press et al.* [1986], *Tarantola* [1987], and *Parker* [1994]. First, we solve (3) using the method of singular value decomposition (SVD), in which we minimize $||\mathbf{b} - A\mathbf{x}||_2$. If the results are not satisfactory, for example, if the moment obtained in not the right one, then we again use SVD but constrain the moment to a preassigned value (constraint M). If the results are still not satisfactory, for example, if there are large negative moment rates on the fault, we remove small singular values and examine the solution. Finally, in some instances we shall find the solution with the smallest first differences in space and time and compare it with the correct solution. In the second approach, we solve (3) using various combinations of the physical constraints discussed above and the method of linear programming, in which the 1-norm of the penalty functional

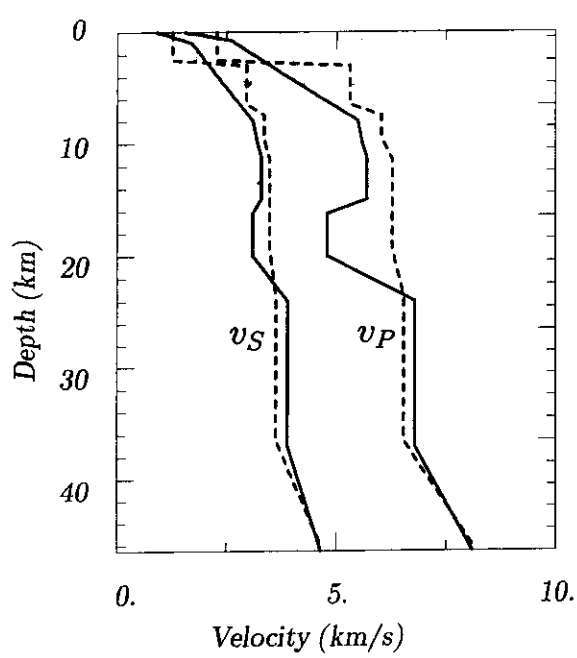

Figure 2. The P and S wave velocity profiles with depth in the crust for medium $M1$ (solid line) and medium $M2$ (dashed line).

is minimized. In some instances when using this second approach, we shall find solutions with the smallest second differences, following the formulation developed and applied to the earthquake faulting problem by *Das and Kostrov* [1990, 1994]. For some cases we use only the second approach to solve the inverse problem. The inversion method used together with the constraints and the results obtained for each case are summarized in Table 1.

Results

More than 40 inversions were performed. Selected cases are discussed in detail below.

Case 1

The synthesized vertical accelerograms in this case correspond to a unilateral rupture that spreads out over a 2.55 km-long and 50 m-wide fault in 21 time steps with a rupture velocity of $v_r = 0.7v_S$ in $M1$. The number of cells (nx) along fault strike is 51 and the number (nh) along the fault dip is 1. The number of time steps will be denoted by nt. The shortest wavelength (about 1.2 km for this case) is much larger than the fault width. Figure 3 shows the rupture model, the moment rate history and distribution and the final moment over the fault for this forward problem. (The corresponding source time function is shown later in Figure 5a.) The six synthesized accelerograms are displayed in Figure 4. Simply in order to check our programs, we solve this problem with the same rupture model and the the same Earth structure as in the forward problem. The system of equations has 51 unknowns and about 1500 equations (sum of all the samples in all the accelerograms) and is an exact one. A simple unconstrained SVD solution is found to agree with the forward problem to machine accuracy.

Case 1a: Rupture front constrained to actual front. We next constrain the rupture velocity v_r to be the same as in the forward problem ($0.7v_S$), but without restricting the number of times each cell behind the rupture front releases moment (MTO). The number of unknowns is now 554. The unconstrained SVD solution is close to the moment rate distribution of Figure 3 but with some negative values behind the rupture front, the magnitude of these moment rates being about 1% of the constant moment rate level of the forward problem. The solution fits the accelerograms to several significant figures. The solution source time function is compared to the true one in Figure 5a. For the first few time steps, when the area of slip on the fault is not large, the agreement is good, but at later times the source time function obtained oscillates about the correct solution. Though the total moment is correctly reproduced without being constrained, the final moment distribution on the fault, plotted in Figure 5b, also oscillates around the actual solution. Thus the negative moment rates, though small, when summed in space to produce the source time function or in time to obtain the final moment, have a nonnegligible contribution. Excluding small singular values did not improve the situation significantly. The centroids of the moment distribution in time and along strike are shown in Table 1. Both centroids are found to be close to the correct ones.

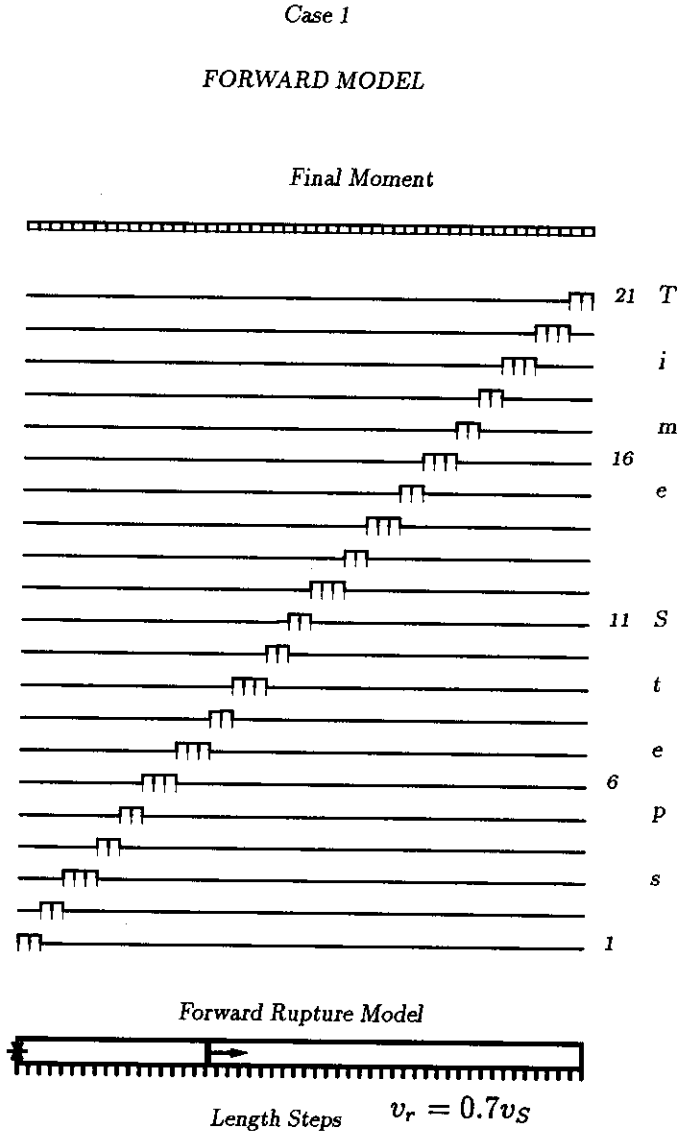

Figure 3. The forward model for case 1. The rupture model is displayed at the bottom of the figure, the moment rate time history along the fault length above it and the final moment along the fault is illustrated at the top. The fault length is taken along the abscissa and time is plotted along the ordinate. The numbers at the right indicate the time step. The level of moment release at each cell is 1 x 10^{11} N m. The cells that are slipping at each time step are indicated by tick marks below the trace. The scales used for plots similar to this will be kept the same throughout the paper to facilitate comparison, though the shift between time steps might vary in later figures in the interest of clarity. The solutions of the inverse problems for case 1, case 2a, and case 3 should be compared to this figure.

We next find the solution with the smallest first differences in space and time, but are still unable to remove the large number of small negative moment rates from the solution. We then solve the problem using linear programming and

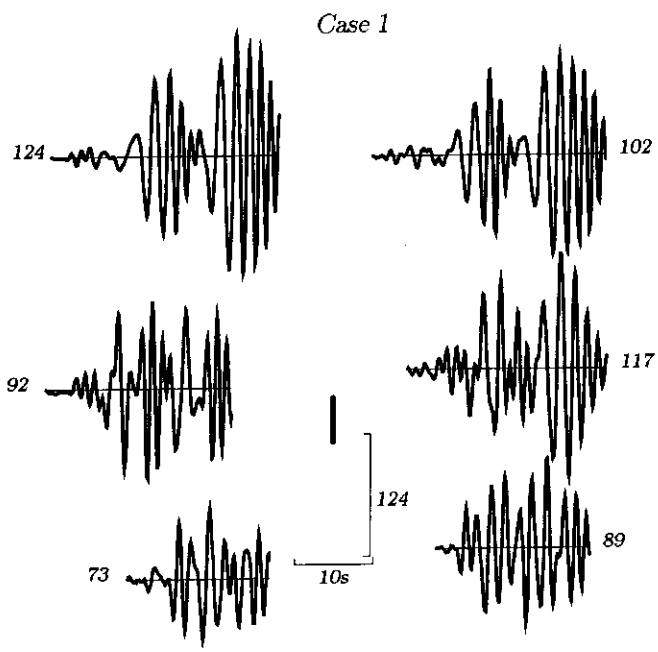

Figure 4. The synthetic accelerograms for the fault and station geometry of Figure 1, for the forward model of case 1. The thick line is the fault strike and the numbers next to each accelerogram give the maximum ground acceleration, multiplied by 100, in centimeters per second squared.

enforcing the moment rate to be positive (Case 1a(2)). All aspects of the forward model are now reproduced exactly. Even though cells have the freedom to release moment during more than one time step, it is found that each cell releases moment only once. Thus for the simple rupture model used here, we can reproduce the moment rate distribution and history on the fault if we know the rupture front, the focal mechanism and fault geometry, and Earth structure, by constraining the moment rate to be positive but without constraining the total moment. Since the predicted accelerograms cannot be distinguished from the original accelerograms (Figure 4), they are not plotted.

Case 1b: Weak causality applied to rupture front. We next apply the weak causality constraint (*R2*), with cells behind the causal front being allowed to release moment as often as necessary (MTO). We solve the inverse problem using both SVD and linear programming. The number of unknowns is now 987. The conclusions are the same as in case 1a. Thus as long as the positivity constraint is enforced, we can reproduce the rupture process using the weak causality constraint, knowing the fault mechanism, the fault geometry, and the Earth structure.

Case 1c: Rupture front constrained to propagate more slowly than in the forward problem. We next consider the same problem as in case 1a, but constrain the rupture front to a velocity of $0.5v_S$. We use only the linear programming approach in this case. The moment is not constrained and cells are allowed to release moment as often as necessary, but the moment rate is constrained to be positive. The number of unknowns is now 398. Owing to the low rupture speed con-

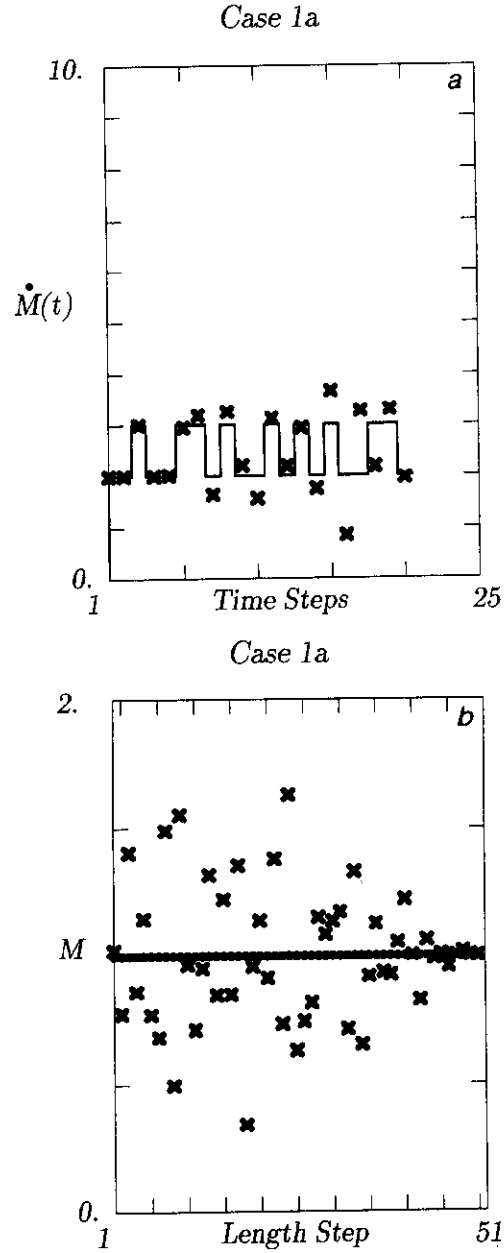

Figure 5. (a) Moment release per time step, multiplied by 1 x 10^{11} N m, on the fault for the forward problem (solid line) and the solution (crosses) for case 1a. In the forward problem either two or three cells break at each time step. The number of cells allowed to break at each time step is the same in the forward and in the inverse problem in this case, but the figure demonstrates that the amount of moment released at each time step in the inversion does not agree with that in the forward problem. (b) Final moment distribution, multiplied by x 10^{11} N m, on the fault for the forward problem (dots) and the solution (crosses) for case 1a.

straint used in the inversion, only part of the fault can rupture in the total rupturing time, which is determined by the durations of the synthetic accelerograms. Figure 6 shows the forward and inverse rupture models and the moment rate history obtained. Figure 7a shows the fit to the data; the fit is not per-

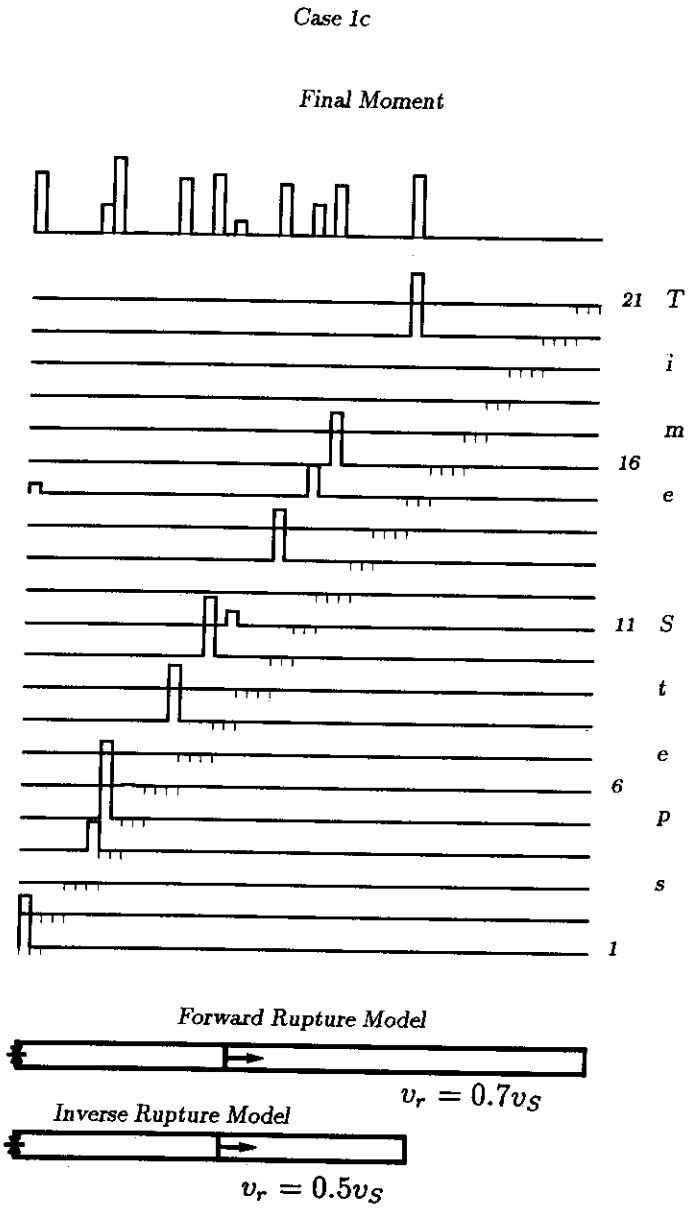

Figure 6. Same as Figure 3 but for the inversion in case 1c. Compare with Figure 3.

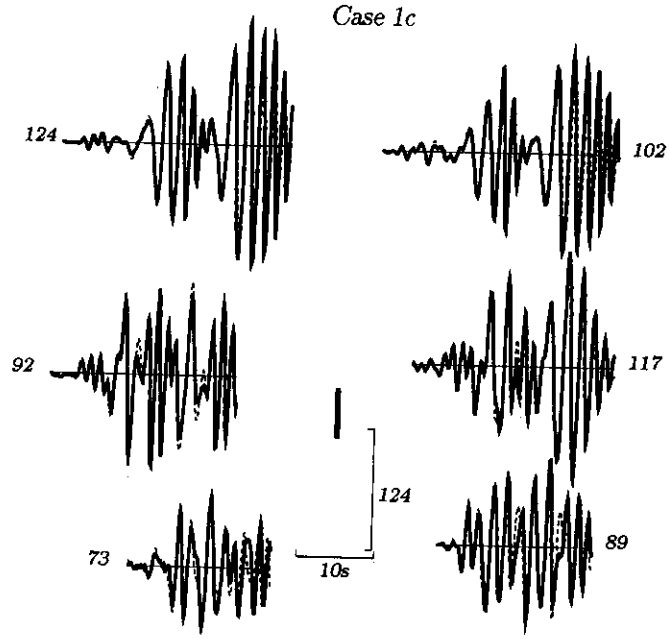

Figure 7a. Same as Figure 4 but for case 1c.

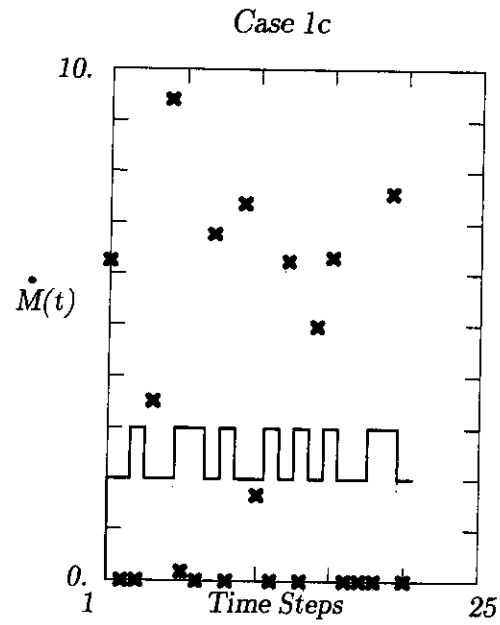

Figure 7b. Comparison of the data (solid lines) with synthetics (dashed lines) for case 1c. Notations and symbols are the same as in Figure 4.

fect, the l_1-misfit as defined by *Das and Kostrov* [1990] being 47%. However, the fit shown in Figure 7a would be considered very good for real data. Neither the moment rate distribution and history, the final moment, nor the source time function (Figure 7b) is reproduced well. The centroid in time is not far from the correct one but, as expected, the centroid along strike is not correctly obtained (see Table 1). Note also a cell rupturing well behind the rupture front. The moment was 20% larger than in the forward problem.

Case 1d: Rupture front constrained to propagate more slowly than that in forward problem, moment constrained. The solution obtained for this case using linear programming is not significantly better than for case 1c. Thus constraining the rupture front to propagate at too low a speed produced a poor fit to the data, which provides a clue that our inversion model is incorrect. We next attempt to smear out the moment distribution behind the rupture front by minimizing the maximum moment rate, as described by *Das and Kostrov* [1994], with 10% additional misfit to the data being permitted. It is found that the moment does spread out more evenly behind the rupture front but is still far from the correct solution. The results of a smoothed solution in which the sum of the modulii of the second differences of the moment rates were minimized, as formulated by *Das and Kostrov* [1994], with 10% additional misfit to the data being permitted, is very similar.

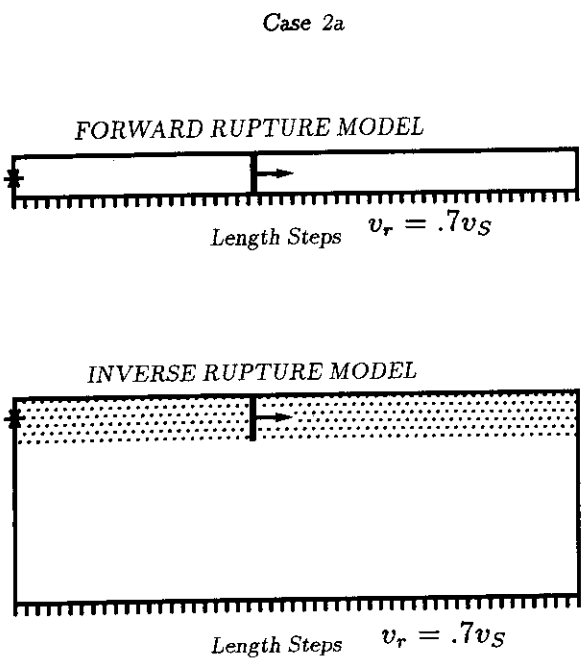

Figure 8. The forward and inverse rupture models used in case 2a. The top of the fault is at the same depth, 1 km, below the Earth's surface and the rupture nucleation points are marked by the asterisks. The shaded area in the inverse model is the part of the fault that slipped in the forward problem.

Case 2

We next consider a set of cases to obtain insight into the effect of inverting seismograms using a narrower or wider fault region than in the forward problem. We use the linear programming approach to solve the inverse problem in all cases in this section.

Case 2a: Inversion for wider fault than in forward problem. The forward and inverse rupture models for this case are illustrated in Figure 8. The forward problem is the same as in case 1, the data being shown in Figure 4, but the inverse model is taken as a 2.55 km x 250 m fault, with the top of the fault being at the same depth as in the forward case (1 km) and embedded in the same structure, $M1$. The rupture in the inversion model nucleates at the same point and propagates at the same speed ($0.7v_S$) as in the forward model, with each cell releasing moment only once as the rupture passes. The number of unknowns in this problem is 255. The only other constraint used is the positivity of moment rate. In the solution, the fit to the data is exact to three decimal places and the total moment is correctly reproduced. Figure 9a shows the moment rate history at the hypocentral depth level (stippled region in Figure 8), where the moment was released in the forward problem. Comparison with the correct solution (Figure 3) reveals that the level of moment release at the rupturing cells is not correctly obtained. Often a large moment is released at a certain cell without any moment being released at adjacent cells. No moment was released at the deeper levels even though this was allowed in the inversion. The final

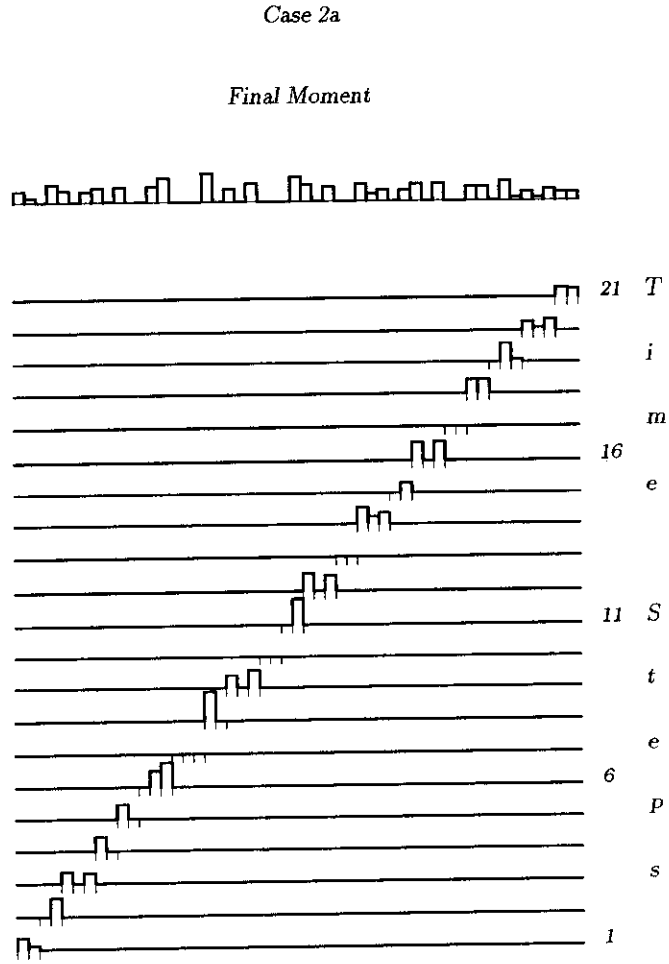

Figure 9a. Same as Figure 3 but for the inverse problem case 2a, plotted at the hypocentral cell level. Compare with Figure 3. No moment was released at the deeper parts of the fault, though this freedom was allowed in the inversion.

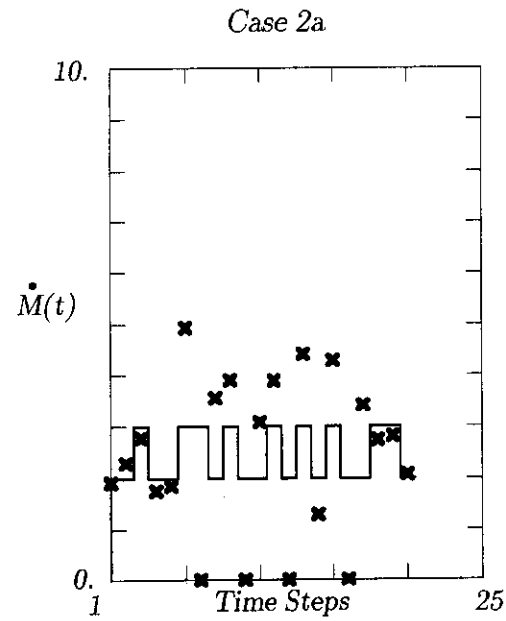

Figure 9b. Same as Figure 5a but for case 2a.

moment distribution, plotted at the top of Figure 9a, shows that the constant moment release over the fault is not reproduced. The source time function (Figure 9b) is also not reproduced correctly, but Table 1 shows that the centroids obtained are close to the correct ones. Next, the inverse problem is solved without any restriction on how often cells behind the rupture front are allowed to release moment (case 2a(2)). The number of unknowns is now 3731. The fit to the data is excellent and the total moment is correctly reproduced. The moment rate history at the hypocentral level and the final moment distribution on the fault are similar to that in case 2a. Thus when the positivity of moment rate is enforced, the width of the rupturing area and the moment centroids are correctly found, provided the rupture velocity and the Earth structure are known, even though the fault width in the inversion is larger than that used in creating the synthetic accelerograms. The moment release history, the final moment distribution, and the source time function are not, however, reproduced correctly.

Case 2b: Inversion for narrower fault area than in forward problem. The forward and inverse faulting models used in this case are illustrated in Figure 10. We construct synthetic accelerograms for the case of a 2.55 km x 250 m fault, with the rupture propagating at a constant speed of $0.7v_S$. Each cell is allowed to release moment only once as the rupture front passes. This is very similar to the classical "Haskell model" but with a curved rupture front. We perform the inversion using a 2.55 km x 50 m fault, with the top of the fault being at the same depth (1 km) as in the forward case and embedded in the same structure, $M1$. The rupture nucleation point and the rupture speed are the same in the inverse and forward models. The moment is not constrained and each cell is allowed to release moment only once as the rupture front passes. The number of unknowns in this case is 51. The l_1 misfit of the solution to the data is 18%, this difference being essentially undetectable by eye. The rupture process in time is plotted in Figure 11a. The total moment is found to be 95% of the correct value but the uniform moment release at the rupture front is not reproduced correctly; very large moment is released at certain fault cells but none at adjacent ones. The source time function, shown in Figure 11b, is not correctly reproduced. The spatial and temporal centroids of the moment distribution are found to be very close to the actual solution (Table 1). We then solve this same problem using the weak causality constraint (case 2b(2)) in order to allow more freedom in the inversion, but permit cells to release moment only once. The number of unknowns increases to 1038. The l_1 misfit is 12% and the moment is larger by about 10%. Figure 12 shows that although the rupture front position is not preassigned, the moment release is confined primarily to the vicinity of the true rupture

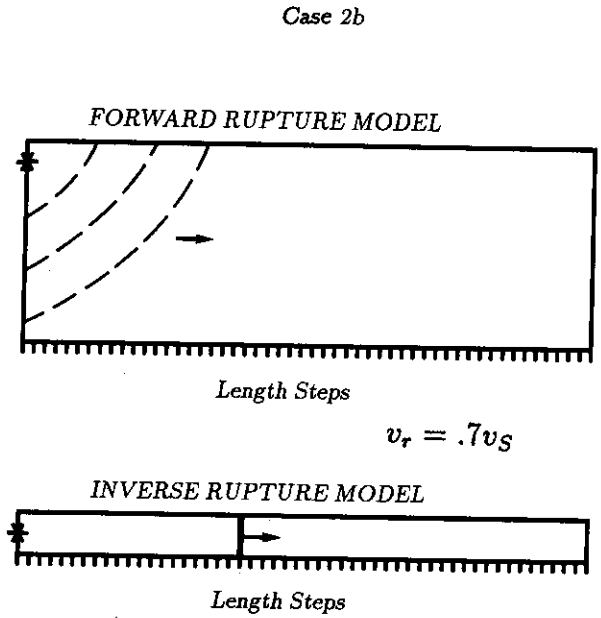

Figure 10. Same as Figure 8 but for case 2b.

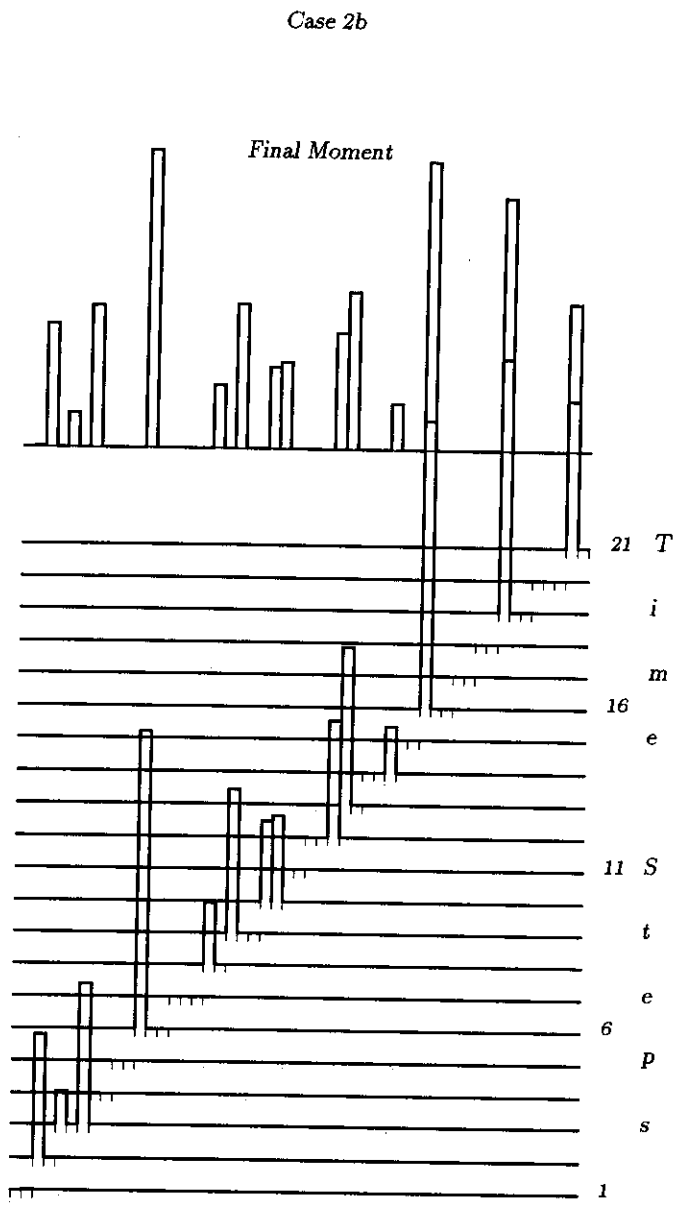

Figure 11a. Same as Figure 3 but for the inverse problem case 2b.

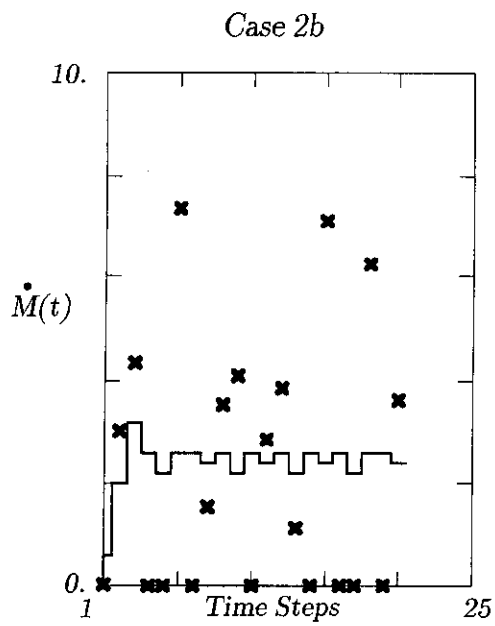

Figure 11b. Same as Figure 5a but for case 2b.

front, with some moment release both ahead and well behind it. The centroid of the moment release in both time and along fault strike is found correctly, but the source time function is not reproduced.

Case 3

We next consider a set of cases to find the effect of using incorrect Earth velocity models. Clearly, there is potential for such errors in Earth velocity to be aliased into artifacts in the solution. Here we demonstrate what some of these artifacts can be.

Case 3a: Effect of incorrect Earth structure. We construct synthetics for the 2.55 km x 50 m fault in medium $M1$, with the top of the fault located at a depth of 1 km below the Earth's surface (the forward problem of case 1). The rupture speed v_r is taken as $0.7v_S$ of medium $M1$. We solve the inverse problem using the same fault geometry but in medium $M2$. The rupture speed in the inversion is 70% of the shear wave speed of medium $M2$. Performing an SVD inversion, we obtain a very poor fit to the data with many negative moment rates. Adding constraints clearly will not improve the fit to the data. We then solve the problem using the linear programming approach and the positivity of moment rate constraint, but we are still unable to fit the data. Since the two media are different in the source region (Figure 2), we next determine the hypocentral depth in $M2$ for which the travel times of the first arrivals to the six stations are closest to those for the original source depth in $M1$, and place the fault at this depth (2.05 km) for the inversion. The forward and inverse faulting models are illustrated in Figure 13. We do not preassign the rupture speed but use only the weak causality constraint and allow grids to release moment more than once. Owing to the weak causality constraint, regions of the fault farthest from the nucleation region are found to rupture only

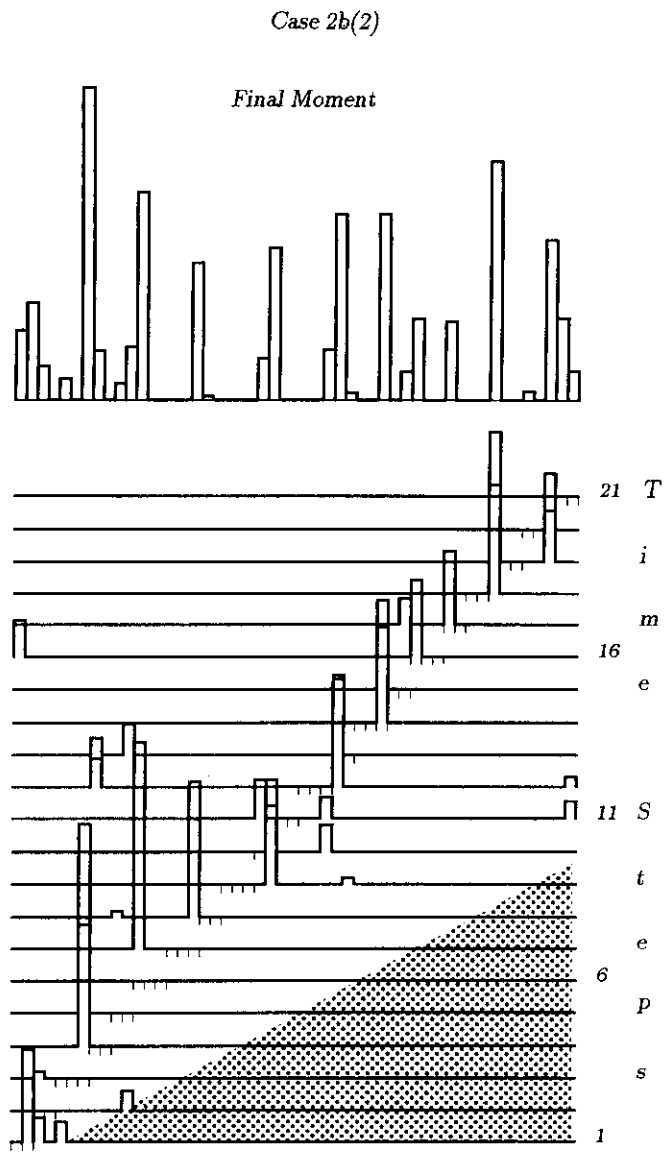

Figure 12. Same as Figure 3 but for the inverse problem case 2b(2). The tick marks shown at each time step are those for the forward problem. The region in space and time excluded by the weak causality constraint is indicated by stippling.

five time steps after nucleation, implying an apparent super P wave rupture speed. The duration of the entire source process is determined by the length of the synthetic accelerograms which is found to be 38 time steps for this inversion, the time step size being the same as in the forward problem, that is, approximately 0.1 s. The difference in the rupture durations of the forward and inverse cases is due to the different durations of the Green functions in the two media. The number of unknown moment rates is now 1818; the total moment is not constrained. Figure 14 shows the fit of the solution to the accelerograms. The fit is far from good, the l_1 norm of the misfit being 84%. Figure 15 displays the moment rate history and the final moment obtained. The first notable result is that the rupture front position is not correctly obtained and

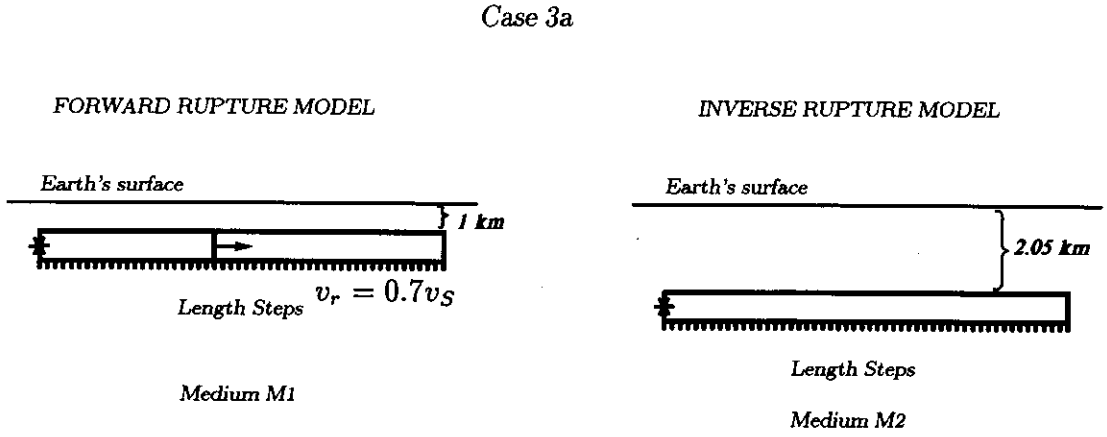

Figure 13. The forward and inverse rupture models used in case 3a. The top of the fault is at depth 1 km below the Earth's surface in the forward case and at depth 2.05 km in the inverse case. The rupture velocity in the forward problem is 70% of the shear wave speed of medium $M1$. The constraint $R2$ is used for the inversion in this case so that the rupture speed is not preassigned. The rupture nucleation points are marked by the asterisks.

the moment release appears to be somewhat randomly distributed on many parts of the fault, though an incoherent front can be identified, as indicated by the dotted line on Figure 15. The average speed of this front is about 60% of the shear wave speed of medium $M2$ at the level where the fault is located. The final uniform moment distribution of the forward problem and the source time function are not correctly reproduced. The moment obtained is 55% larger than the actual moment. The position of the centroid along strike is close to the correct one. The centroid in time, however, is far from correct which is not surprising since the duration of the process in the inversion is much longer than the correct one. But the most remarkable result here is the moment that is released at later times on the fault. Figure 15 shows an additional coherent moment release in space and time appearing from $nt = 20$ on, defining a second moment release front. We call this a "ghost front" and it illustrates how the incorrect structure manifests itself as an artifact of the solution, and would lead in the real case to being interpreted physically as a secondary rupture front. The moment release ahead of the rupture front could potentially be interpreted in the real case as evidence for super shear rupture speed and the random nature of the moment release at some other places as evidence of "asperities" rupturing. The poor fit of the synthetics to the data is the clue that our input model is incorrect.

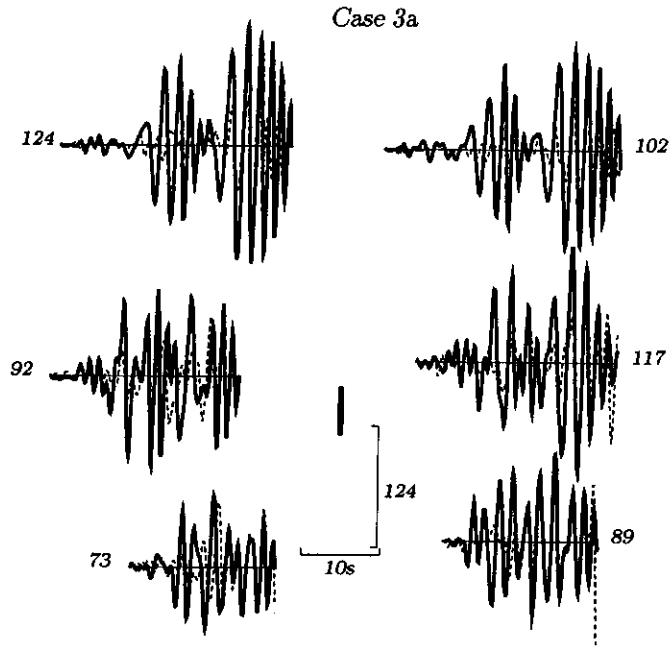

Figure 14. Same as Figure 4 but for case 3a.

Case 3b: Effect of incorrect Earth structure with a larger fault size. Finally, we use a larger fault, 2.55 km x 250 m in the inverse model, with the top of the fault located at a depth of 2.05 km, to see if this additional freedom improves the fit to the data. We find that the fit does not improve significantly. Constraining the moment only worsens the fit, as expected. Hence with the incorrect structure we are simply unable to fit the data.

Discussion and Conclusions

Using synthetic data, we solve the inverse problem for a very simple faulting model in order to gain insight into solutions of such unstable problems. We demonstrate that the constraint of positivity of moment rate on the fault is essential to reproducing all facets of the solution, namely the moment release history and distribution, the source time function, and the final moment distribution. With this constraint, we find that even if we do not preassign the rupture front position it is identifiable in the inversion, for all practical purposes, when the medium properties are known and for the simple rupture model considered here. The centroids of the moment release in space and time are generally found to be

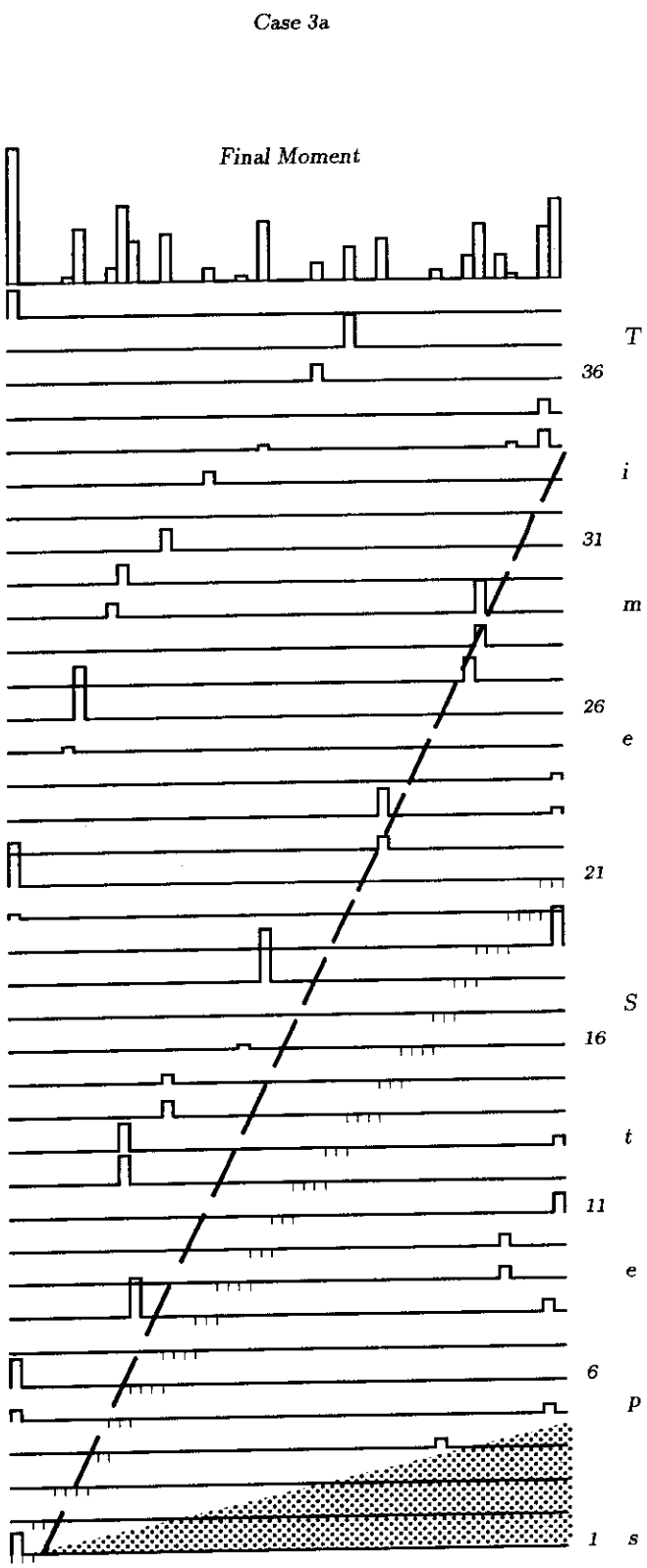

Figure 15. Same as Figure 12 but for the inverse problem case 3a. The tick marks shown at each time step are those for the forward problem in medium $M1$. The dashed line identifies the incoherent rupture front, propagating at an average speed of about 60% of the shear wave speed of the medium $M2$ at the depth where the fault is located.

close to the correct ones, even in cases where the fit to the data is poor, except that when the rupture front is constrained to propagate more slowly than in the forward problem (cases 1c and 1d), the spatial centroid is not correctly obtained. However, the constant level of moment release and the uniform final moment distribution of the forward problem generally are not correctly reproduced. In inversions of real data, such artifacts might be interpreted as evidence for heterogeneous faulting. We are unable to fit the data adequately if the rupture velocity is constrained to be lower than that in the true velocity or if the fault is constrained to be narrower than its true width. Use of incorrect crustal structure also has this effect. In the latter case, the position of the main rupture front is not obtained correctly. Instead, an additional coherent "ghost front" is obtained behind the rupture front, illustrating how poor knowledge of crustal structure can be manifest as an artifact in the solution.

The problem remains that in many cases the fit to the data is very good even when the faulting process is poorly reproduced, so that in the real case it would be difficult to know when one has obtained the correct solution. Then one must follow the suggestion of *Das and Kostrov* [1990, 1994] and consider many possible solutions, seeking physical characteristics that persist in many solutions. For example, if solutions resulting from differing constraints all show that the main moment release was at a particular region of the fault or give nearly the same average rupture velocity, then we may have some confidence in these features of the solution. Using data from the 1989 Macquarie Ridge earthquake, *Das and Kostrov* [1994] showed how to perform further optimizations to see if a particular common feature persists. If it does, then can one have some confidence that it is truly representative of the actual faulting process. This study, using artificial, noise-free data, also shows that small variations in the quantities obtained, such as rupture velocity, moment release over the fault, and so on, may not be reliable. The complications in using real, noisy data, deconvolution of instrument responses, and so on, will only make the situation even more difficult.

The results presented here suggest that it is essential to carry out a study such as this before inverting real data in order to have some idea of the limitations of the inversion for the particular case under investigation.

Acknowledgments. This study was started while one of the authors (P.S.) visited the Department of Earth Sciences in Oxford in the framework of agreements between the Royal Society and Accademia Nazionale dei Lincei, and was continued under partial support from the EC program, Environment and Climate, Topic IV.1.1, Natural Risks – Seismic Hazard, under EPOCH contract EPOC-CT91-0042 and ENVIRONMENT contract EN5V-CT94-0513. We would like to thank Steve Hartzell and Bill Foxall, and the anonymous Associate Editor for very thorough reviews and the many constructive comments that helped to improve and clarify the manuscript. We would also like to thank B. V. Kostrov for many helpful suggestions and comments during the entire course of this work. The computations were done on the Cray-YMP8 at the Rutherford-Appleton Laboratories, Didcot, U.K. under a Supercomputing grant obtained through the Natural Environmental Research Council of the U. K.

References

Aki, K., and P. G. Richards, *Quantitative Seismology: Theory and Methods*, 932 pp., W.H. Freeman, New York, 1980.

Ben-Menahem, A., and D. G. Harkrider, Radiation patterns of seismic surface waves from buried dipolar point sources in a flat stratified Earth, *J.Geophys. Res., 69*, 2605-2620, 1964.

Backus, G. E., Comparing hard and soft prior bounds in geophysical inverse problems, *Geophys. J., 94*, 249-261, 1988.

Beroza, G. C., and P. Spudich, Linearized inversion of fault rupture behavior: Application to the 1984 Morgan Hill, California earthquake, *J. Geophys. Res., 93*, 6275-6296, 1988.

Das, S., Tectonic implications of the moment distribution of the 1986 Andreanof Islands earthquake, paper presented at the *International Symposium of Earthquake Source Physics and Earthquake Precursors*, pp. 143-146; sponsored by IASPEI, NCSPEI, SCJ and SSJ, Univ. Tokyo, Tokyo, Japan, 19-22 Nov, 1990.

Das, S., and B. V. Kostrov, Inversion for seismic slip rate and distribution with stabilizing constraints: Application to the 1986 Andreanof Islands earthquake, *J. Geophys. Res., 95*, 6899-6913, 1990.

Das, S., and B. V. Kostrov, Diversity of solutions of the problem of earthquake faulting inversion. Application to SH waves for the great 1989 Macquarie Ridge earthquake, *Phys. Earth Planet. Inter., 85*, 293-318, 1994.

Das, S., P. Suhadolc and B. V. Kostrov, Realistic inversions to obtain gross properties of the earthquake faulting process, *Tectonophysics*, in press, 1995.

Florsch, N., D. Faeh, P. Suhadolc, and G. F. Panza, Complete synthetic seismograms for high-frequency multimode SH waves, edited by A. Udias and E. Buforn, *Proc. El Escorial Workshop, Pure Appl. Geophys, 136*, 529-560, 1991.

Harkrider, D. G., Surface waves in multilayered elastic media, 1, Rayleigh and Love waves from buried sources in a multilayered elastic half-space, *Bull. Seismol. Soc. Am., 54*, 627-679, 1964.

Hartzell, S. H., and T. H. Heaton, Inversion of strong-ground motion and teleseismic waveform data for the fault rupture history of the 1979 Imperial Valley, California earthquake, *Bull. Seismol. Soc. Am., 73*, 1553-1583, 1983.

Hartzell, S. H., and P. Liu, Calculation of earthquake rupture histories using a hybrid global search algorithm: Application to the 1992 Landers, California earthquake, *Phys. Earth Planet. Inter.*, in press, 1995.

Hartzell, S., G. S. Stewart, and C. Mendoza, Comparison of L_1 and L_2 norms in a teleseismic waveform inversion for the slip history of the Loma Prieta, California, earthquake,*Bull. Seism. Soc. Am., 81*, 1518-1539, 1991.

Haskell, N. A., Total energy spectral density of elastic wave radiation from propagating faults, *Bull. Seismol. Soc. Am., 54*, 1811-1841, 1964.

Haskell, N. A., Total energy and energy spectral density of elastic wave radiation from propagating faults, II, A statistical source model, *Bull. Seismol. Soc. Am., 56*, 125-140, 1966.

Haskell, N. A., Elastic displacements in the near-field of a propagating fault, *Bull. Seismol. Soc. Am., 59*, 865-908, 1969.

Jackson, D., The use of a priori data to resolve non-uniqueness in linear inversion, *Geophys. J. R. Astron. Soc., 57*, 137-158, 1979.

Kikuchi, M., and Y. Fukao, Iterative deconvolution of complex body waves from great earthquakes – The Tokachi-Oki earthquake of 1968, *Phys. Earth Planet. Inter., 37*, 235-248, 1985.

Kikuchi, M., and H. Kanamori, Inversion of the complex body waves, *Bull. Seismol. Soc. Am., 72*, 491-506, 1982.

Kostrov, B. V., The theory of the focus for tectonic earthquakes, *Izv. Earth Phys.*,258-267, 1970.

Kostrov, B. V., Mechanics of the Tectonic Earthquake Focus (in Russion), 176 pp., Nauka, Moscow, USSR, 1975.

Kostrov, B. V., and S. Das, Principles of earthquake source mechanics, *Appl. Math. Mech. Ser.*, 286 pp., Cambridge University Press, New York, 1988.

Madariaga, R., The dynamic field of Haskell's rectangular dislocation fault model, *Bull. Seismol. Soc. Am., 68*, 869-887, 1978.

Mendoza, C., and S. H. Hartzell, Aftershock patterns and main shock faulting, *Bull. Seismol. Soc. Am., 78*, 1438-1449, 1988a.

Mendoza, C., and S. H. Hartzell, Inversion for slip distribution using teleseismic P waveforms: North Palm Springs, Borah Peak, and Michoacan earthquakes, *Bull. Seismol. Soc. Am., 78*, 1092-1111, 1988b.

Mendoza, C., and S. H. Hartzell, Slip distribution of the 19 September 1985 Michoacan, Mexico, earthquake: Near-source and teleseismic constraints, *Bull Seismol. Soc. Am., 79*, 655-669, 1989.

Miyatake, T., Reconstruction of dynamic rupture process of an earthquake with constraints of kinematic parameters, *Geophys. Res. Lett., 19*, 349-352, 1992.

Olson, A. H., and J. G. Anderson, Implications of frequency-domain inversion of earthquake ground motions for resolving the space-time dependence of slip on an extended fault, *Geophys. J., 94*, 443-455, 1988.

Olson, A. H., and R. J. Apsel, Finite faults and inverse theory with applications to the 1979 Imperial Valley earthquake, *Bull. Seismol. Soc. Am., 72*, 1969-2001, 1982.

Panza, G. F., Synthetic seismograms: The Rayleigh waves modal summation, *J. Geophys., 58*, 125-145, 1985.

Panza, G. F., and P. Suhadolc, Complete strong motion synthetics, *Seismic Strong Motion Synthetics, Computational Techniques*, editied by B. A. Bolt, vol. 4, pp. 153-204, Academic, San Diego, Calif., 1987.

Parker, R. L., Geophysical Inverse Theory, 386pp., Princeton Univ. Press, Princeton, New Jersey, 1994.

Press, W. H., B. P. Flannery, S. A. Teukolsky, and W. T. Vetterling, *Numerical recipes: The Art of Scientific Computing*, 818 pp., Cambridge University Press, New York, 1986.

Ruff, L. J., Fault asperities inferred from seismic body waves, in *Earthquakes: Observation, theory and interpretation*, edited by H. Kanamori and E. Boschi, pp. 251-276, North-Holland, New York, 1983.

Suhadolc, P., P. Harabglia and G. F. Panza, Deterministic modeling and estimate of strong ground motion: The Iripinia, Italy, November 23, 1980 earthquake, *Proc. 9th Euro. Conf. on Earthquake Engg.*, Kucherenko Tsniisk USSR Gosstroy, Moscow, 100-109, 1990.

Tarantola, A., Inverse problem theory. Methods for data fitting and model parameter estimation, 613pp., Elsevier, Amsterdam, 1987.

S. Das, University of Oxford, Department of Earth Sciences, Parks Road, Oxford OX1 3PR, U. K. (e-mail:das@earth.ox.ac.uk)

P. Suhadolc, Universita di Trieste, Istituto di Geodesia e Geofisica, Via E. Weiss, 4, 34127 Trieste, Italy. (e-mail: suhadolc@geosun0.univ.trieste.it)

(Received February 6, 1995; revised November 10, 1995; accepted November 17, 1995.)

Journal of Seismology **2:** 1–25, 1998.

Effect of non-uniform station coverage on the inversion for earthquake rupture history for a Haskell-type source model

A. Saraò[1], S. Das[2] & P. Suhadolc[1]
[1] *Dipartimento di Scienze della Terra, Università di Trieste, Via E. Weiss 1, 34127 Trieste, Italy*
[2] *Department of Earth Sciences, University of Oxford, Parks Road, Oxford OX1 3PR, U.K.*

Received 4 December 1996; accepted in revised form 8 January 1998

Abstract

In order to determine how reliably one can invert accelerograms to determine the rupture process details, when the station configuration is less than optimal, we use the vertical component of synthetic accelerograms for a Haskell-type earthquake rupture model, at stations in the vicinity of a dip-slip fault and solve the inverse problem. Of the various station configurations used, one is a uniform distribution and the others are very non-uniform. Faults of two different aspect ratios are considered. We mainly use much larger spatial and temporal cell sizes in the inversion than we use to construct the artificial data. The fault mechanism and the fault area are taken as known in the inversions. To solve the inverse problem, we use the method of linear programming and stabilize the solution by the use of physical constraints. The constraints of positivity of the slip rates on the fault is used in all cases in this study. In some cases, additional physical constraints such as preassigning the final moment, the rupture speed, and so on, are also used. We find that using a cell size almost double the wavelength of interest, we are able to reproduce the solution of the problem, even when we add a small amount of random noise to the artificial data, provided the source medium structure is known. We show that the best station configuration is when the stations are on the hanging wall, due to the fact that they provide the best illumination of the fault surface. This provides an incentive to install permanent ocean bottom strong ground motion stations in subduction zones. We also analyzed the effect of the rupture propagation direction on the results of the inversion showing that even four stations are sufficient to retrieve the rupture process if they are in the forward direction of the rupture propagation; the results for this case are better than when the four stations are placed in the backward direction, even when their positions are such that they illuminate the fault in exactly the same way as the four stations in the forward direction. Thus azimuthal distribution and the resulting illumination of the fault as well as the relation of the position of the stations to the direction of rupture propagation are more important than simply the number of stations. Finally, we find that proper knowledge of source medium structure is essential to recover the source process details reliably and that poor knowledge of crustal structure cannot be compensated by adding stations or by additional constraints.

Introduction

The extraction of information about the details of the complete rupturing process of an earthquake by solving inverse problems depends on the availability of high-quality seismograms. Clearly uniform azimuthal distribution of stations around a rupturing fault appears desirable when solving such problems. Since this is often not possible, a study to determine the limitations due to lack of optimal station coverage is important in order to evaluate the reliability of the inverse problem solutions. Some possible configurations of non-uniform station distribution, necessitated by the tectonic and geographic settings, are shown in Figure 1. In many subduction zones, say the circum-Pacific belt, stations are located only on the hanging wall. We call this configuration C-1 in Figure 1(a). In some cases, the stations may be located on the footwall side, as, for example, on the New Guinea subduction zone. We call this configuration C-2 in Figure 1(b). Due to the fact that an earthquake fault may lie partly on land and partly under water, we may have the configurations C-3 and C-4, shown in Figure 1(c). In the Mediterranean area, situations where the stations happen to

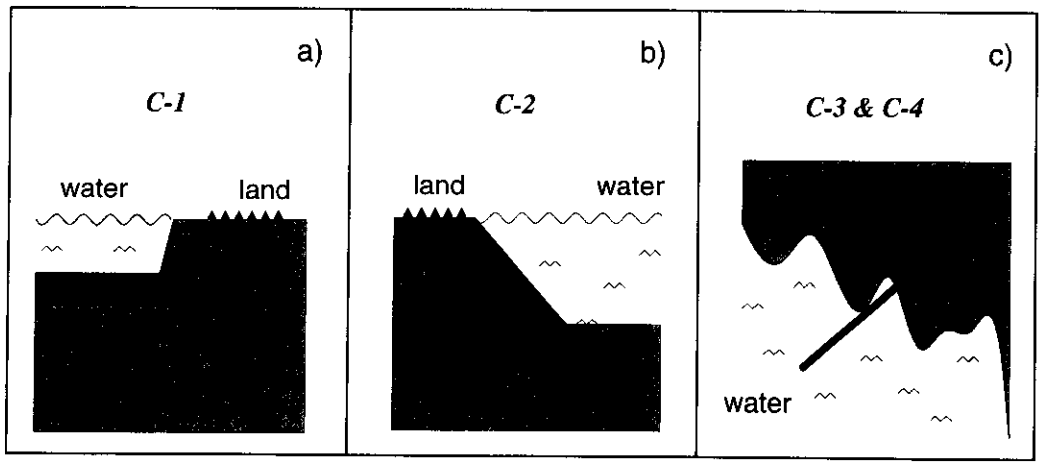

Figure 1. Schematic diagram showing possible non-uniform configurations of seismic stations (solid triangles) relative to an earthquake fault, based on actual situations. (a) and (b) are vertical cross-sections and (c) is a map view; in (c) the thick line is the fault trace.

be at the end of the fault are not uncommon (e.g. the Iberian peninsula, the Messina straits in Italy or on the Yagur fault in Israel). Sometimes this can happen by chance. In Erzincan, Turkey, a single accelerometer was installed in the vicinity of the active fault. When the 1992 earthquake occurred, it was found that the instrument happened to be at one end of the rupture segment (Bernard et al., 1997). There are even geopolitical reasons why stations cannot be placed in the most optimal configuration. The rupture, in such cases, may initiate underwater and propagate towards the stations or initiate under land and propagate away from the stations. Since the effects of the focussing (or de-focussing) of the waves relative to the stations are different in these two cases, we shall consider both these possibilities in this study. We call the case when the rupture propagates towards the station cluster as C-3, and away from the cluster as C-4. The results of our study will help in evaluating the reliability of the moment distribution pattern obtained using very few stations as well as when the azimuthal distribution of available stations is poor. Finally, and not the least important, the results of this study are of practical importance in that they will aid in decisions on the effective (including financial considerations) installation of seismic stations in the field, for example, around recognized active or capable faults.

The problem of non-uniform station coverage has been considered before in moment tensor studies (Stump and Johnson, 1977; Hwang, 1985; Satake, 1985). Olson and Anderson (1988) considered a problem very similar to the one in this paper, for a vertical strike-slip fault. They solved the problem in the frequency domain and used a minimum-norm condition but did not use the physical constraints we use in this paper. Miyatake et al. (1986), Iida et al. (1990), Iida (1993), also carried out a detailed study on the resolving power of strong-motion arrays for source inversion but without any constraints on the solution.

It is well known that such solutions are unstable (Kostrov and Das, 1988; Das and Kostrov, 1990, 1994), and recent work by Das and Suhadolc (1996) and by Das et al. (1996) using vertical component synthetic accelerograms at regional distances has shown that some constraints are essential. In this paper, we shall consider the effect of non-uniform station distribution on the inversion to obtain details of the seismic moment rate history and distribution over the fault for the inversion where additional stabilizing constraints, such as constraining the final moment or disallowing back-slip on the fault, are used. We shall use synthetic accelerograms and stations located at regional distance. One of the reasons we prefer to use accelerograms rather than numerically integrated velocity records, is that it is acceleration that is actually recorded in strong motion investigations. However, the most important reason is to use the data that are most appropriate for retrieving the rupturing process of an earthquake. Madariaga (1977) showed that high-frequency waves are radiated when a rupture front changes speed. Consequently, it is such high-frequencies that must be studied to obtain details of the rupturing process and these are best manifested in measured ground accelerations. The use of the vertical component in the inversion was motivated by several factors. First, at local distances, it is impossible to combine the observed horizontals to get the transverse component of ground motion, as one can do with teleseismic data. So one must use both horizontal

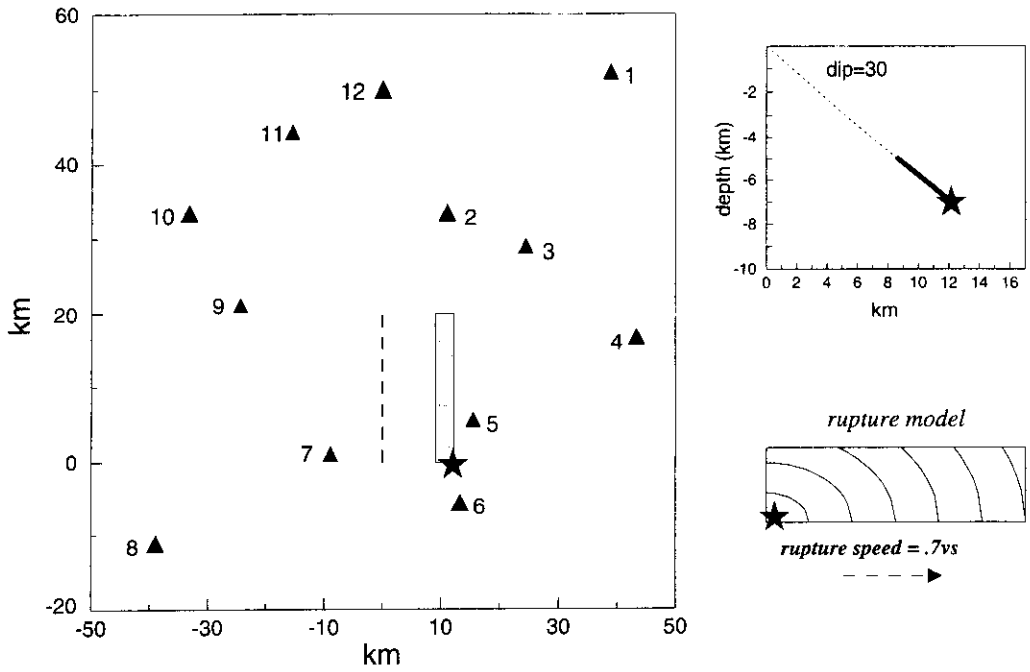

Figure 2. Schematic representation of the dipping fault geometry (cross section on the right) and the 12-station distribution C-0 (plane view on the left) used in this study. The fault dip is taken as 30°. Two different fault aspect ratios (1:5 and 1:2) are used in this study, the fault lengths being taken as 20 km in both sets of cases. The star denotes the hypocenter and the triangles the stations. In the plane view part of the figure, the dashed line is the trace of the buried fault and the stippled fault region is its projection on the horizontal plane. The schematic of the rupture model used in constructing the synthetic accelerograms is also shown.

components in the inversion, thus increasing the number of equations to be solved. This leads to problems related to possible ill-conditioning of the associated matrix, as we shall show in this paper. In addition, use of the vertical components minimizes possible site effects on such records, as it is well known that they are, in general, less sensitive to site effects. Although hard rock site stations are preferable, this is not always possible and stations on 'well-consolidated sediments' or even on unconsolidated sediments might sometimes have to be used out of necessity. Studies using the horizontal components will be the subject of future investigations. Das and Suhadolc (1996) and Das et al. (1996) have shown that with six uniformly distributed stations and a Haskell-type model of the faulting process, some important features remain unresolved even for the problem without any noise in the data. We, therefore, first find the most favourable configuration for which we are able to reliably solve the constrained inverse problem. Once we have done this, we shall perform numerical tests with very non-uniform azimuthal station distributions in order to determine the importance of the station coverage and number of stations necessary to obtain acceptable solutions. We shall consider problems without and with random noise in this study. We shall mostly consider the case when the artificial data is generated using very fine cells and the inversion is performed with much larger cells. Finally, we shall perform the inversion with a different medium than that used in the forward problem. In many of the cases, it may appear that we have deliberately chosen the worst scenario. Since one of our purposes is to find those properties of the faulting process that can be reliably obtained, no matter how unfavorable the scenario, this is desirable. In some real cases the station coverage may be excellent and the knowledge of structural models good, but such cases are globally indeed rare. Most seismic regions of the world are still not well studied and instrumented. In the latter cases the scenario can be even worse than all those discussed in our artificial tests. As a matter of fact, it is very difficult when considering blind test cases as we do here, to

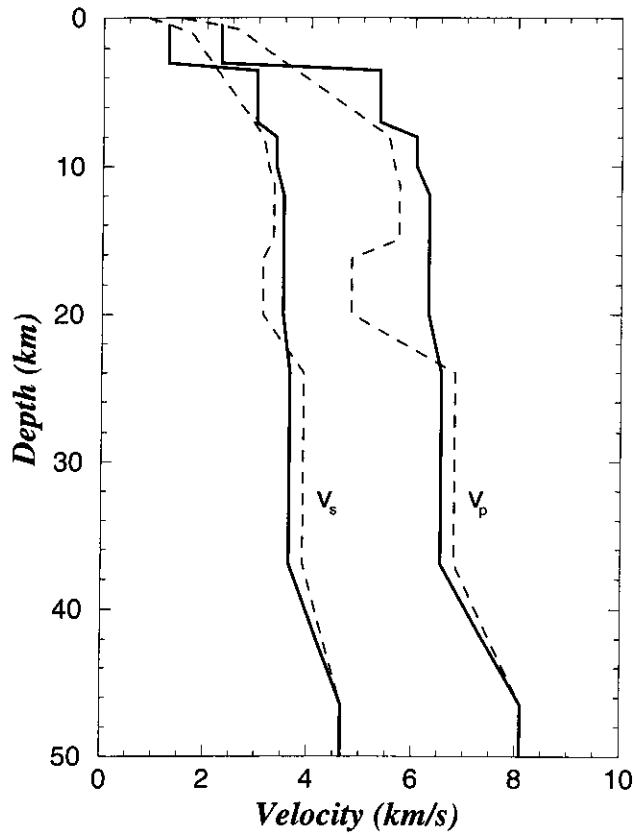

Figure 3. The velocity models used in this study. The solid line shows the structure (M1) used in the forward modeling and in some of the inversions. The dashed line shows an alternative structure (M2) used in some other inversions.

construct the most realistic scenario. Thus, our 'worst case scenarios' may still not be realistic enough, and the real cases may be even worse.

The fault geometry and method of solution

The forward and inverse problems are similar to those described in detail in Das and Suhadolc (1996) and are, therefore, described only briefly here. We construct synthetic vertical accelerograms using the method of multimodal summation for extended sources (Panza and Suhadolc, 1987), for rectangular faults of two different aspect ratios. One fault is taken as 20 km long and 4 km wide, and the other is 20 km × 10 km. The top of the fault is located at a depth of 5 km and the faulting mechanism is taken as pure thrust, the fault dip being taken as 30°. Since the seismograms for a pure normal fault are the same as for a thrust fault with the sign reversed, our results are also applicable to pure normal faulting with a 30° dip. The schematic fault geometry and an uniform twelve-station distribution is shown in Figure 2 and relevant faulting parameters are listed in Table 1. We shall call the 12-station distribution C-0. The P and S wave velocity models (M1) in the vicinity of the source used in constructing the synthetic data are shown by the solid lines in Figure 3. We shall keep some parameters of the faulting model (namely, the source mechanism, rupture area and the process duration) in the forward and inverse problem the same, since our aim is to study separately the effects of other model parameters, such as different station configurations, different physical constraints, and incorrect Earth structure in the source region, on the solution. The fault is discretized into square cells and the source process duration into discrete time steps. The details of the cell sizes and time steps are listed in Table 1 for all the cases considered in this study. The rupture model is a discrete analog of a Haskell-type model, with rupture propagating at a speed of 70% of the shear wave velocity of the medium. As the rupture passes by, each cell slips only during one time step, in the forward model. An azimuthally uniform idealized distribution of 12 stations (Figure 2) around the fault is used in the first step of this study, while in subsequent cases fewer and very non-uniform station distributions will be considered.

We use the method of linear programming developed for this problem by Das and Kostrov (1990, 1994) for the solution of the set of linear equations $A\vec{x} = \vec{b}$, generated from the elastodynamic representation theorem by the discretization of the problem. A is the matrix of the Green functions, $\vec{b}$ the seismograms and the unknown moment rates are the x's. The physical constraints to be used were enumerated by Das and Suhadolc (1996). We shall require positivity (P) of the slip rate for all cases in this study. The final moment constraint (M), in which the total moment value must equal some pre-assigned value and a rupture speed constraint in which the rupture front is not allowed to propagate faster than some preassigned speed will be considered in some cases. When this limiting rupture speed is taken as the shear wave velocity, we call the constraint R1; when it is 70% of shear wave velocity, we shall call it R1*. A 'weak causality' constraint in which the slip rate is zero in a cell and time step that would produce a signal before the first arrival at any station from the hypocentral cell (R2), may also be used sometimes. A cell may be allowed to slip more than once in the inversion (MTO). The constraints selected in the different cases are also listed in Table 1. We shall define the misfit of the solution synthetics to the

Table 1. Summary of parameters for each station configuration studied

Inversion case	Forward model Δx	Δt	nx	nh	nt	Inverse model Medium	h	Δx	Δt	nx	nh	nt	Constraints	Noise added	Remarks
	Fault of size 20 km × 4 km														
Case 1:															
Same grid size in	2	0.39	10	2	24	*M*1	5	2	0.39	10	2	24	*R*1*	no	All the aspects of
													*R*1	no	the solutions
													*R*3, MTO	no	reproduced.
forward and	1	0.39	20	4	24	*M*1	5	1	0.39	20	4	24	*R*1	no	Instability increases
													*R*3, MTO	no	as the grid
inverse case	0.5	0.39	40	8	24	*M*1	5	0.5	0.39	40	8	24	*R*1*	no	size decreases.
													*R*3, MTO, M	no	
Case 2: Larger grids in inversion	0.25	0.1	80	16	92	*M*1	5	2	0.39	10	2	24	*R*1*, MTO	no	The fit to
													*R*1*, MTO, M	no	accelerograms
													*R*2, MTO	no	good;
													*R*2, MTO, M	no	the slip rate
													*R*3, MTO	5%	well
													*R*3, MTO, M	5%	reproduced.
Case 3: Incorrect Earth structure; larger grids in inversion	0.25	0.1	80	16	92	*M*2	5	2	0.39	10	2	24	*R*3, MTO	5%	Poor
													*R*3, MTO, M	5%	solutions.
	Also used only 20s of each accelerogram for C-0 for this case														
	0.25	0.1	80	16	92	*M*2	14	2	0.39	10	2	24	*R*3, MTO	5%	Accelerograms
													*R*3, MTO, M	5%	poorly fitted.
															The slip rate best reproduced when all 12 stations used.
	Fault of size 20 km × 10 km														
Case 1	2	0.39	10	5	24	M1	5	2	0.39	10	5	24	*R*3, MTO	no	Same as Case 1 above
Case 2	0.25	0.1	80	40	137	M1	5	2	0.39	10	5	35	*R*3, MTO	no	Same as Case 2 above
														5%	

Δx is in km; Δt is in seconds; nx = number of cells in which the fault is discretized along the strike direction; nh = number of cells in which the fault is divided along the dip direction; nt = number of steps used to discretize the source time function; h = depth of top of fault in inversion; *R*1: strong causality, rupture front speed constrained to shear wave speed; *R*1*: strong causality, rupture front constrained to move at the 70% of the shear wave speed; *R*2: weak causality; *R*3: without causality.

artificial data, in the ℓ_1-norm sense, as the ratio of the mean absolute error of fit to the mean absolute amplitude of the data (Das and Kostrov, 1990). It should be stated here that comparison of the inversion results with the input is a very strong test of the method and a good comparison between the forward and inverse models is much more revealing than traditional resolution and error matrices. However, in real problems, since there is no other way to estimate the goodness of the result, resolution tests are useful. We do not do such tests here as the simple concept of resolution and error matrices does not hold for the problem where one minimizes the ℓ_1-norm of the residuals. In such cases much more complicated resolution tests, which are beyond the scope of the present paper, would be needed.

More than 110 inversions were performed for this study of which only selected cases will be discussed in detail in the paper. In addition to the ideal distribution of 12 stations (Figure 2), we consider the six non-uniform distributions shown in Figure 4. For each of these station distributions, we consider different combinations of the physical constraints discussed above. For all the above cases, we first perform inversions using the same spatial and temporal cell sizes as used in the construction of the artificial data in order to get

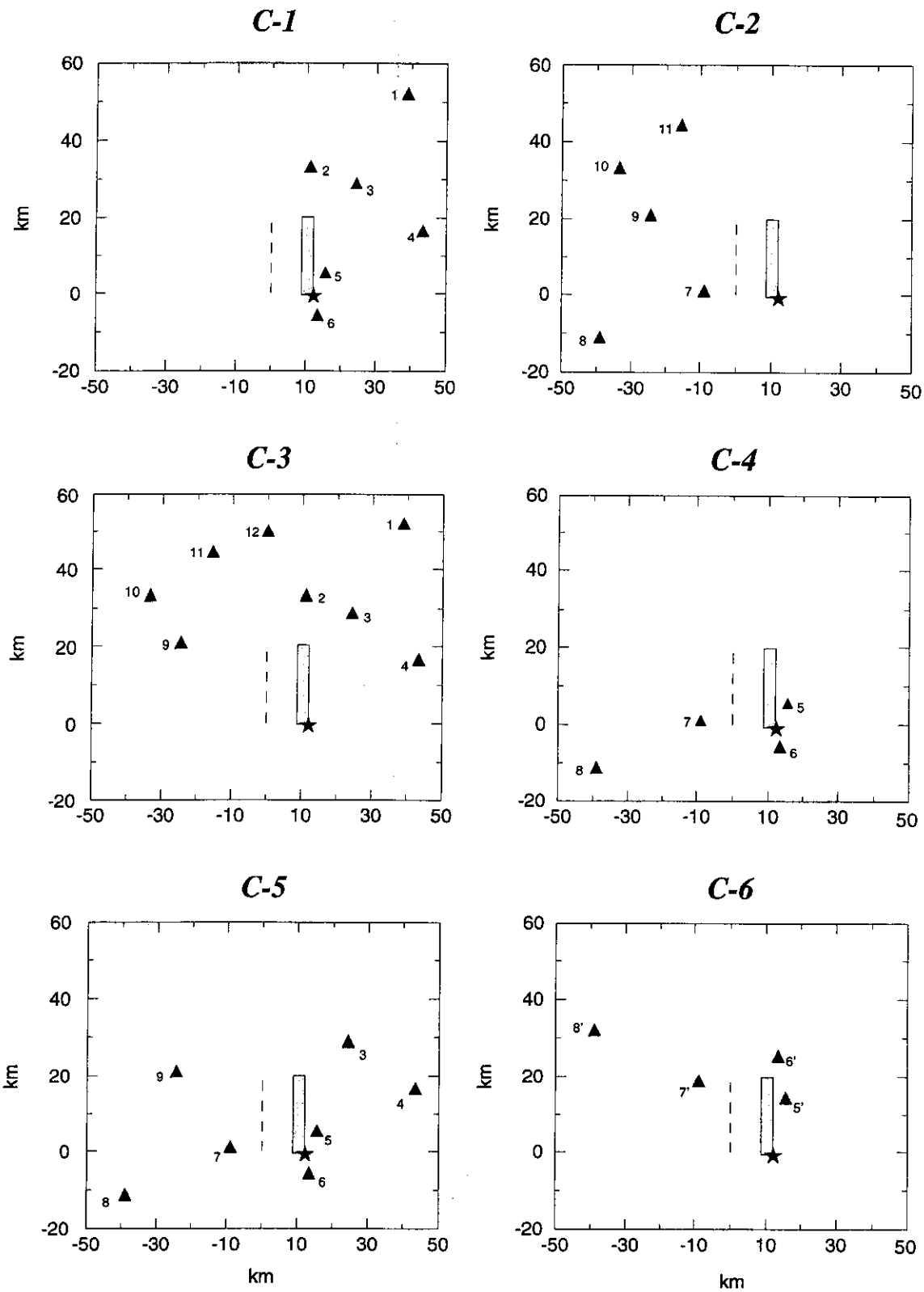

Figure 4. The non-uniform station configurations used in this study chosen to mimic actual possible configurations shown in Figure 1. Two different fault widths are used in this study (the fault lengths are the same in both fault geometries used), but here we plot the fault which is 20 km long and 4 km wide.

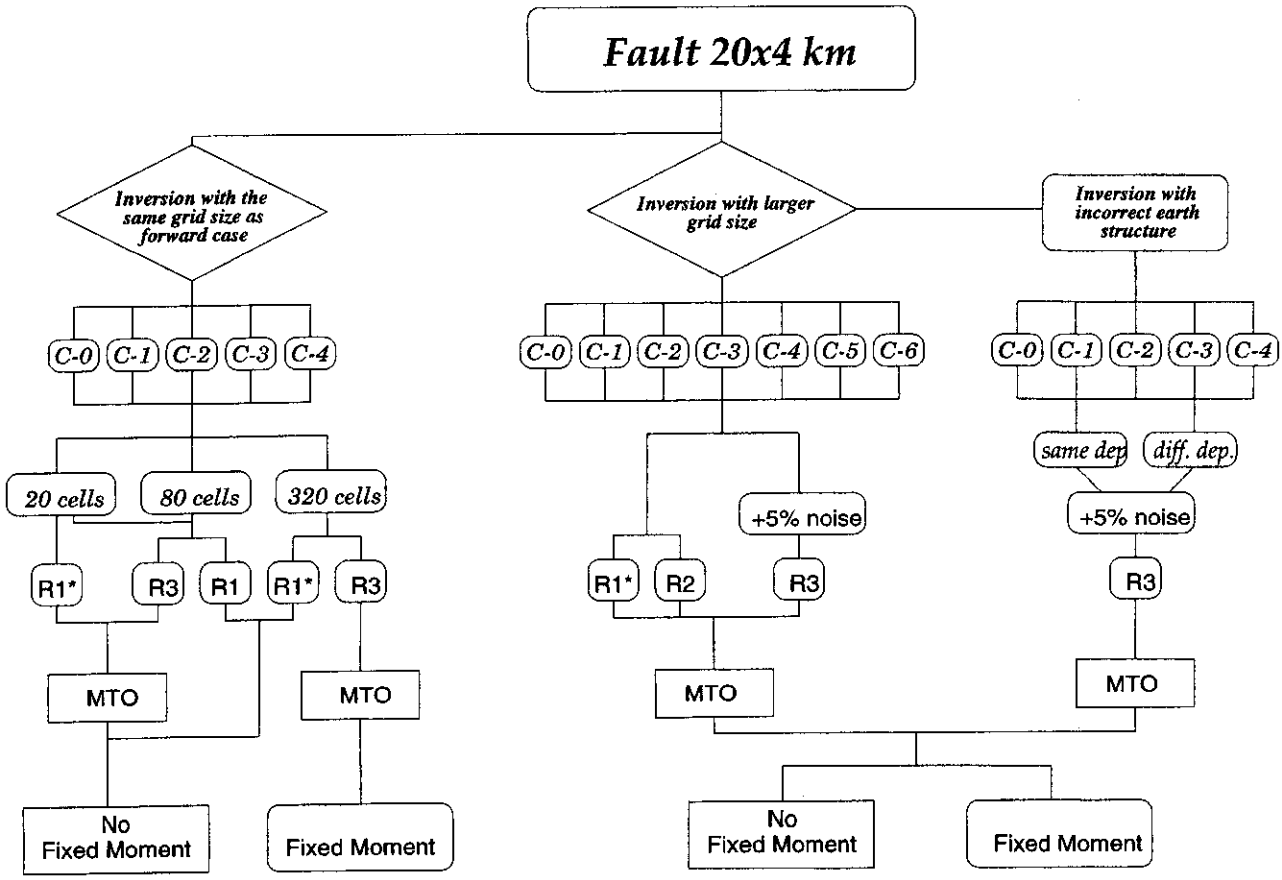

Figure 5a. Chart giving an overview of all the cases considered in this study for the 20 km long and 4 km wide fault. For all the cases, the positivity constraint on the slip rate is used. 'Fixed Moment' denotes the case when the total moment is assigned a priori and 'No Fixed Moment' the reverse. 'R1' denotes strong causality (rupture velocity constrained to be equal to the S wave velocity in the inversion, see Das and Suhadolc, 1996); 'R1*' denotes the case where the rupture velocity is preassigned to be equal to 70% of S wave velocity in the inversion; 'R2' denotes the 'weak causality constraint'; 'R3' is used to identify the case when no causality condition is used. 'MTO' is used to denote the case when grids behind the rupture front are free to slip as often as necessary. In some cases we added 5% of random noise to the artificial data (denoted by '+5% noise'). When using different structures in the forward and inverse problem we perform the inversion for the same fault depth (denoted as 'same dep.') as in the forward problem, and at a different depth (denoted as 'diff. dep.') computed to best agree with the times of first arrival of waves at all the stations.

insight into the inversion. We then carry out inversions using much larger cells in space and time; more than one spatial and temporal cell size will be used in some inversions to investigate its effect on the solution. We shall consider problems with and without random noise added to the data. Finally, we shall perform inversions using 'incorrect' Earth structure. The flow-charts of Figure 5a and Figure 5b give an overall picture of all the cases studied.

Results for the 20 km × 4 km fault

Case 1: Inversions using the same cell sizes in the inverse and forward cases

The artificial data we use in our tests have been computed using the moment rate distribution, which is obviously related to the slip rate by the product of the rigidity modulus and the grid area. In Figure 6, we plot these moment rates, only for the case when the fault is discretized into 20 cells and 24 discrete time steps. This is mainly to facilitate comparisons with inversion results later in the paper. The source medium structure, the fault area, process duration, the depth of the top of the

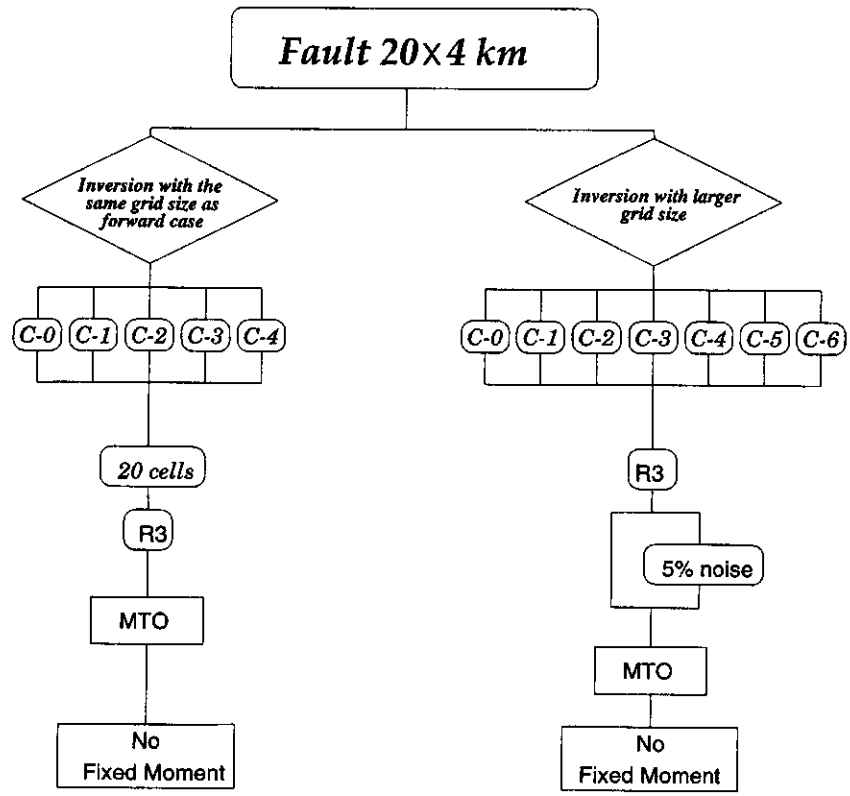

Figure 5b. Same as Figure 5a but for the 20 km × 10 km fault.

fault (h), and the fault mechanism are the same in the inverse and forward problem, in this case.

To investigate the effect of the spatial cell size on the stability of the inversion, we performed tests using three different cell sizes. We considered square cells of 2 km, 1 km and 0.5 km which correspond to 20, 80 and 320 cells on the fault area, respectively. For each cell size we carried out inversions for the five station distributions (C-0, C-1, C-2, C-3, C-4) using the same cell sizes as in the forward problem and analyzed the effect of the different physical constraints. The source time step size Δt is taken as .39s in this set of cases, for both the forward and inverse problem (Table 1).

Test 1 – This test was carried out primarily as a test of our programs. The rupture velocity is constrained to be the same as in the forward model, each cell is permitted to slip only once as the rupture front passes and the positivity of the slip rate is enforced. All aspects of the solution are correctly reproduced for all the station configurations. Even four stations, grouped together at one end of the fault (C-6), are sufficient to reproduce the rupture process. The solutions are reproduced exactly and the fit to the artificial data is very good so that the differences are not visible on plots, and hence they are not included here.

Test 2 – We perform inversions using the weak causality constraint R2 and do not restrict the cells to slip only once. Again, all aspects of the solutions are well reproduced for all the cell sizes and for all the station distributions.

Test 3 – In this case we do not constrain the rupture front in the inversion, that is, no causality constraint is used. The cells are free to slip more than once and the only constraint used is the positivity of the slip rate. The rupture is free to initiate anywhere within the maximum permitted fault area. This is an interesting case, as, in reality, the rupture front position is unknown and the position of the hypocenter is often quite uncertain. As expected (Das et al. 1996), we found that the stability of the problem decreases as the number of the cells increases. For the model with 20 and 80 cells we were able to reproduce the results without any additional constraints. For the case with 320 cells, the computation time needed was excessive, and we shall see below how to improve this situation in Test 4. The relation between the number of cells and the ℓ_1-norm misfit is

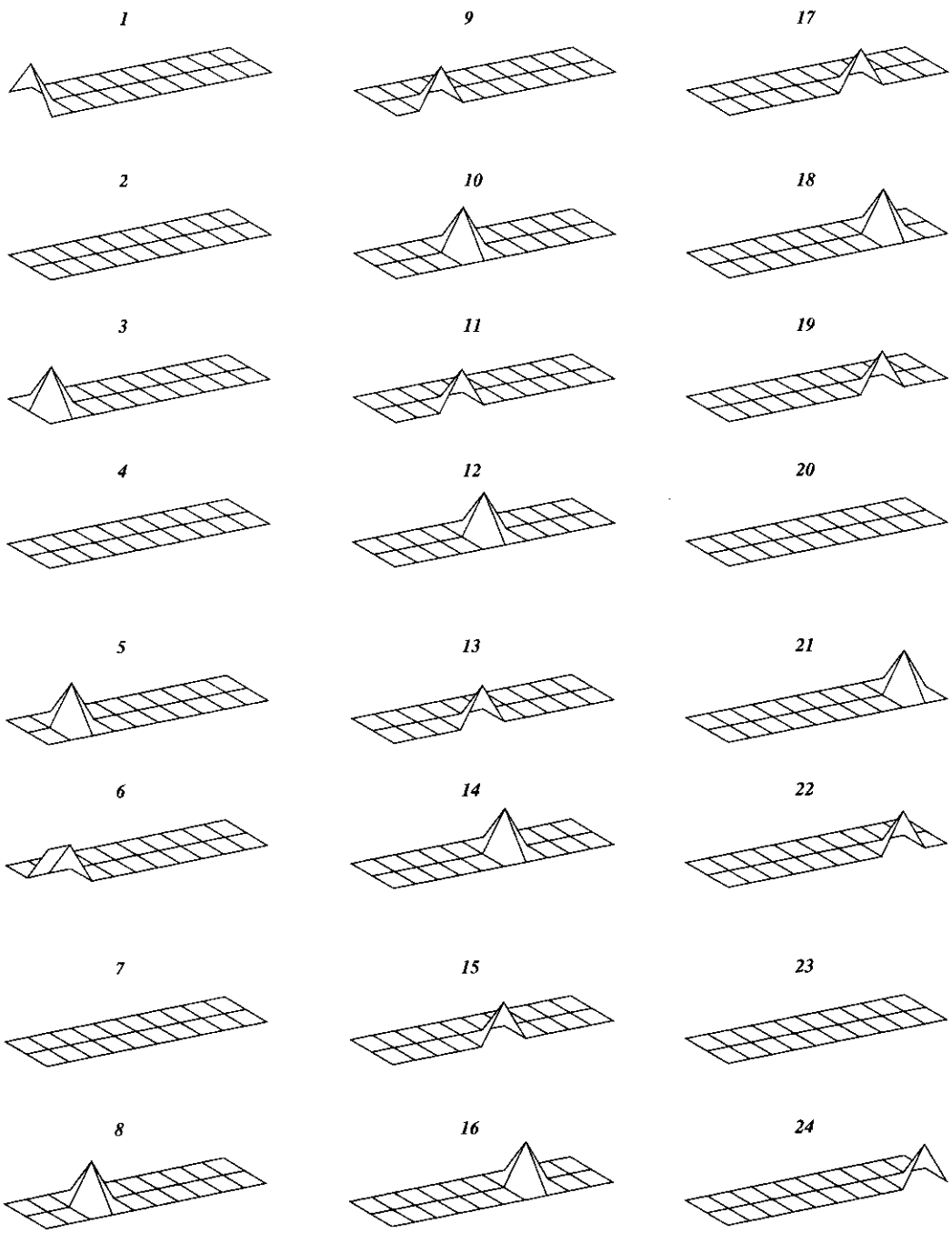

Figure 6. The input moment rate used in Case1 for the fault discretized into 20 spatial cells, is shown at discrete time steps; each step is 0.39s of the source time function. The same plot can be used to compare the inversion results of Case2.

shown in Figure 7. We report for each cell size the misfits for the different configurations. Figure 7 shows that for each cell size the configuration C-1 with the stations on the hanging wall has consistently lower values of the misfit, relative to C-2, with stations on the foot wall.

Test 4 – For the case with 320 cells, we constrained the seismic moment and redid the problem. This reduced the uncertainties in the parameter space and the accelerograms were still fitted well. This demonstrates the necessity of constraints to stabilize the results when using a model with a large number of relatively small cells, as was noted earlier by other authors (Hartzell and Heaton, 1983; Beroza and Spudich, 1988; Das et al., 1996). Clearly, using constraints is one way to reduce the instability of the inverse problem. Next, we

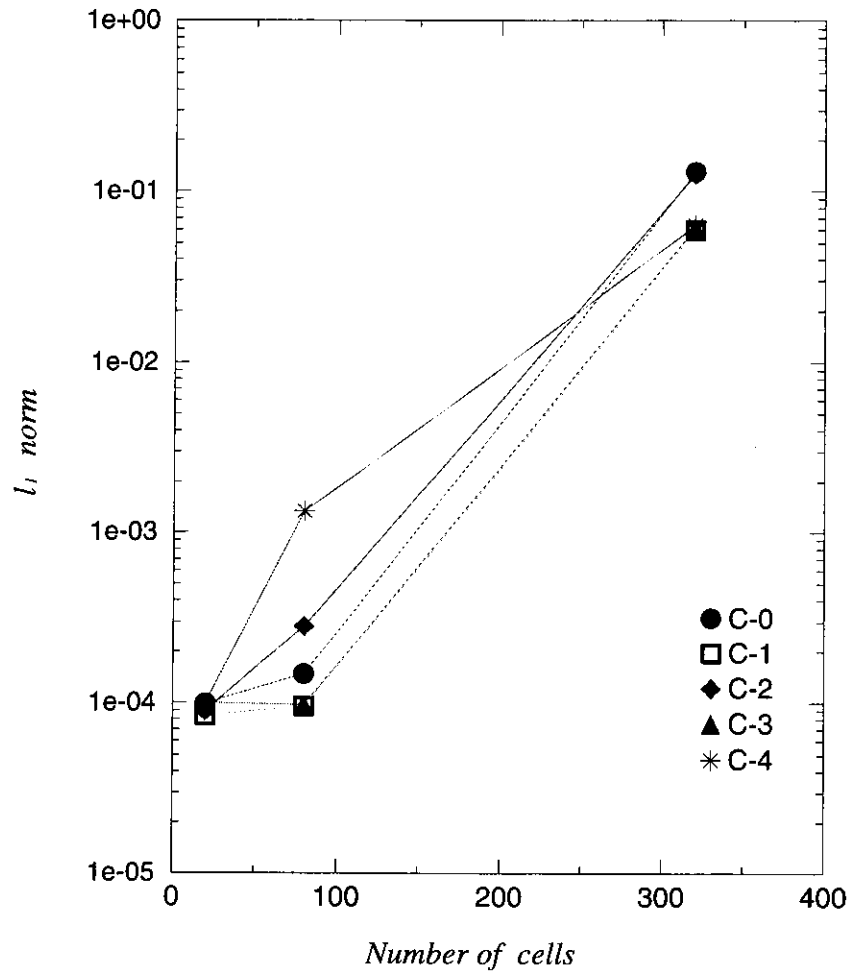

Figure 7. The instability in the solutions when using different cells sizes. The ℓ_1-norm for the five station configurations are plotted against the number of cells.

shall test if it is possible to reduce the size of the matrix and still reproduce the rupture process.

Case 2: Inversion using a larger cell size in space and time in the inverse problem than in the forward problem and with random noise added to the artificial data

We investigate if we can reproduce the total moment rate history and distribution on the fault with a smaller number of cells (that is, larger cells), than that used in the forward problem to generate the synthetic data (Table 1), in order to mimic reality. The accelerograms used as artificial data are computed up to 1 Hz for a cell of 0.250 km. The sampling frequency is 10.24 Hz. This is a reasonably fine discretization for the wavelength of interest in this problem, which is 1.2 km. The cell sizes used for the inversion is 8 times larger in space and 4 times larger in time than the one used in the forward problem. Full details are given in Table 1. We also add some noise to the artificial data in some of the cases (Table 1), in order to mimic not only the 'noise' in the real data mainly due to microtremors not related to the earthquake process, but also to account for the random effect of the 3-D real Earth structure on the signal at any station (the propagation paths from different parts of the fault to the station can be very different). This noise is taken as 5% of the maximum amplitude of the accelerogram at the station, multiplied by a random number. As in Case 1, the source medium structure, the fault area, process duration, the depth of the top of the fault (h), and the fault mechanism are the same in the inverse and forward problem.

Test 5 – We fix the rupture front at its known position and permit the cells to slip only once as the rupture front passes. Even though we reproduce the main features of the solutions, the accelerograms are not perfectly reproduced.

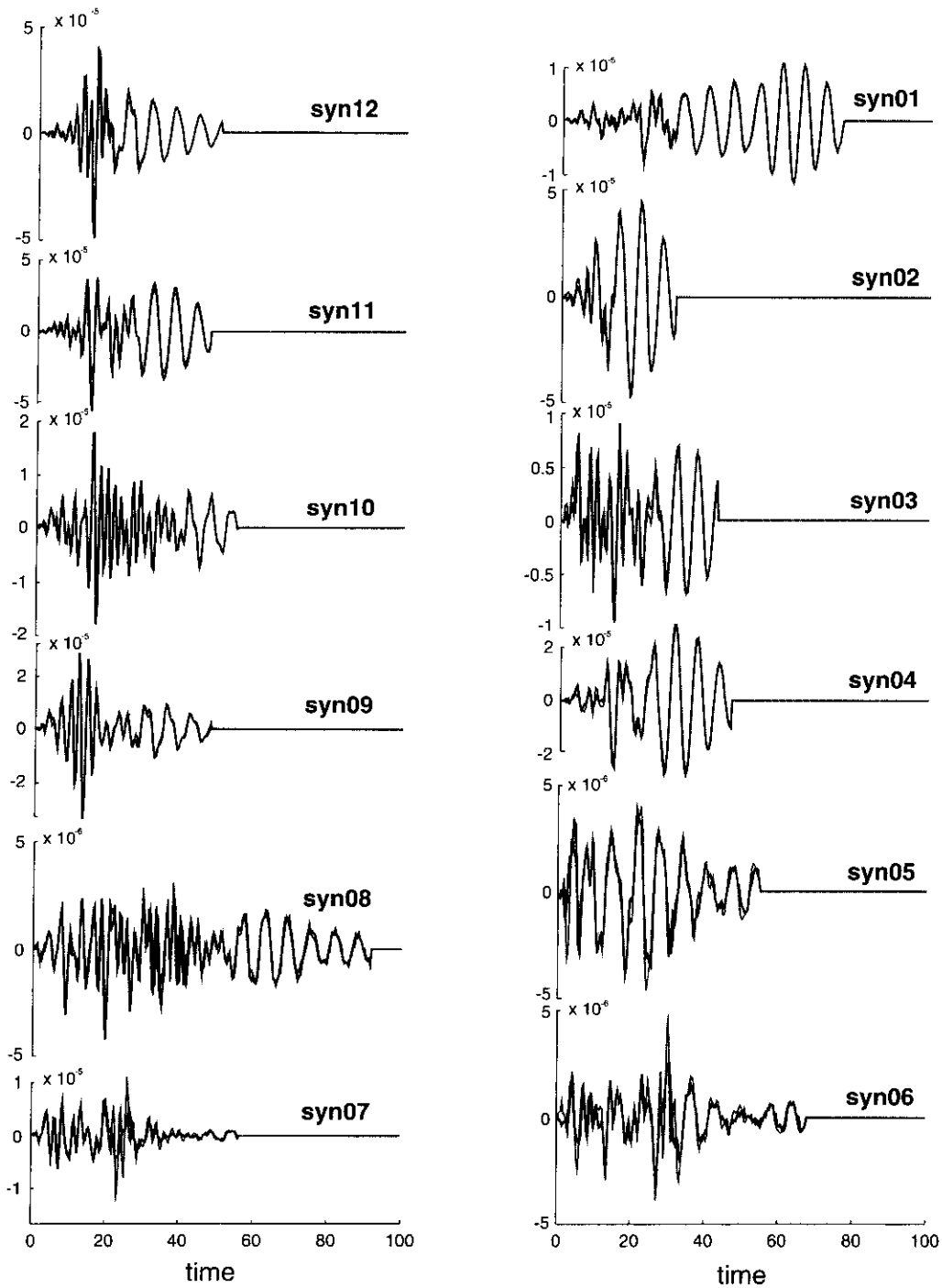

Figure 8. The comparison of the vertical component of the 'artificial data' (solid lines) to the solution accelerograms (dotted lines) for Test 6 of C-0.

Test 6 – We constrain the slip rate to be positive, the cells are allowed to slip as often as necessary and no causality constraint is used on the rupture front. The solution accelerograms obtained after inversion for configuration C-0 are shown in Figure 8. The fit is good and the small differences observed at the stations in the backward direction of the rupture propagation are due to the fact that the amplitudes there are smaller and hence those stations are fit less well than the stations with larger amplitudes. This is also seen by com-

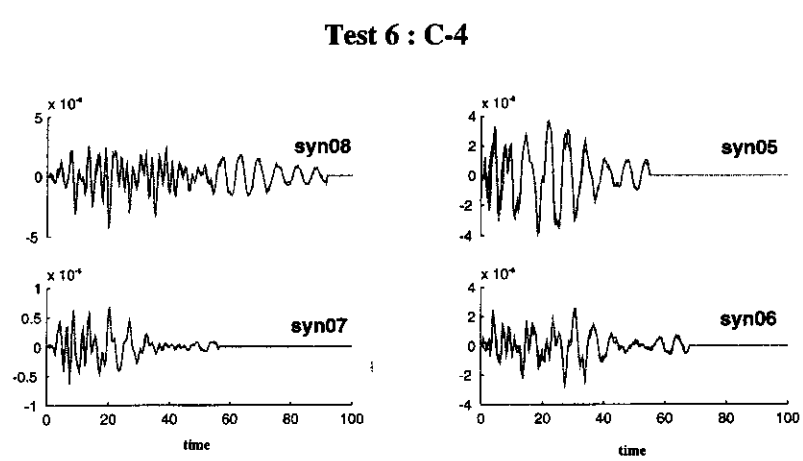

Figure 9. Same as Figure 8 but for Test 6 of C-4.

paring the final relative misfit of the stations among themselves, which shows that the stations in the 'backward' direction with respect to the rupture propagation are less well fitted. In this study we do not normalize the data and we only compare results among configurations which have the same number of stations and same magnitude order of wave amplitudes. By introducing a weight factor before performing any inversion, one could use the mean or the maximum amplitude of the data points at each station as the normalization factor, but we shall not do so in this study.

The waveforms retrieved for configuration C-4, which is one of the cases where the amplitudes of the accelerograms at all the stations used in the inversion are of the same order of magnitude, are shown in Figure 9. The fits of the waveforms improve relative to that for C-0 (Figure 8). The moment rate history and distribution for this test using station distributions C-0, C-1, C-2, C-3 and C-4 are illustrated in Figures 10, 11, 12, 13 and 14, respectively. The best solutions are obtained for C-1. We shall show that this is not only because the stations in C-1 are closer to the fault surface and the physical explanation of this will be given later.

It was not clear if the results obtained for C-4 were relatively poor due to the lower number of stations used in the inversion or due to the particular positions of the stations around the fault. Therefore, we first repeated the inversions for the additional configuration C-5 (Figure 4), using seven stations. C-5 is C-4 but with three additional stations placed in an intermediate position between the forward and backward directions. The fit to the accelerograms obtained for this inversion remains as good as before but the rupture process is now better reproduced. This improvement can be explained by the fact that for C-5, the ray paths from the fault surface to the stations better illuminate the fault area relative to C-4. This is similar to the idea (Menke, 1985) of tomographic imaging of the slip distribution on a fault after an earthquake.

In order to investigate properly the effect of rupture directivity on the inversion, we consider configuration C-6, which is the mirror image configuration of C-4 about the center of the fault, with four stations in the forward rupture direction, so that the fault is illuminated in the same way by C-4 and C-6. We find that the inversion for C-6 is better than C-4 (Figure 15). Thus, the directivity effect plays an important role in how well one is able to retrieve the rupture process details from the inversion. The misfits for the different station distributions are plotted in Figure 16a. Due to the different number of stations used in the different configurations, the misfits are only comparable for configurations C-1 with C-2 and for C-4 with C-6. The lower values of the misfits confirm that the station distributions C-1 and C-6 are better than C-2 and C-4, respectively.

Test 7 – We next constrain the seismic moment to the known value. The moment rate distribution is fairly well reproduced for configurations C-0, C-1, C-2 and C-3 and no slip ahead the rupture front, even though this was permitted in the inversion. We plot only the results for C-2 (Figure 17), and by comparing with Figure 12 for the corresponding case without the moment constraint, we see that solutions did improve. For C-4 (Figure 18), comparing with the Figure 14, we see that the addition of the moment constraint did not improve the solution.

Test 6 : C–0

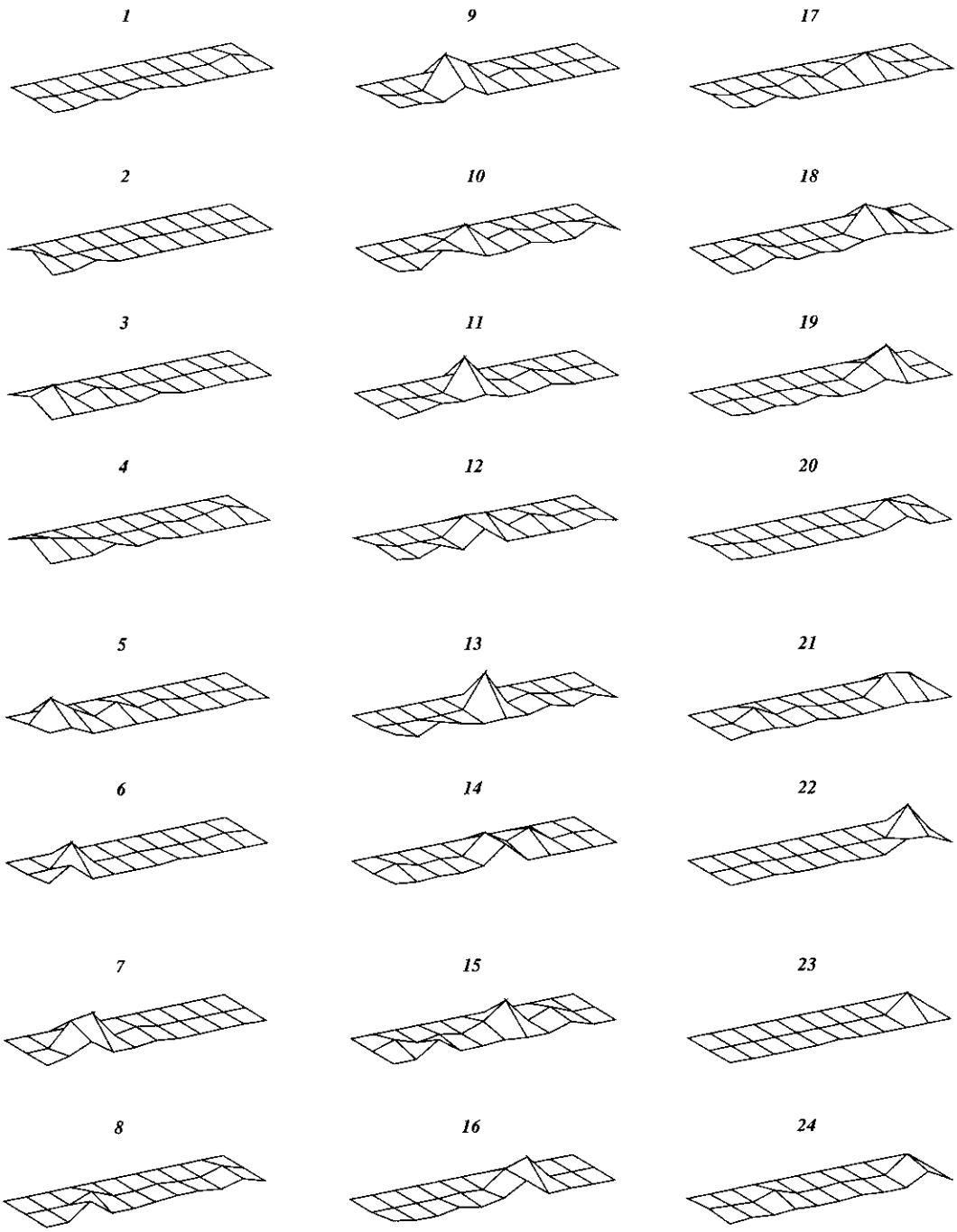

Figure 10. Moment rate map in time obtained by the inversion in Test 6 of C-0.

Test 8 – An unwanted aspect of the solution in Test 6 was the small amount of moment ahead of the rupture front. To eliminate this effect we use the weak causality constraint and grids are permitted to slip more than once. This eliminates the moment ahead of the rupture front but worsens the fit of the accelerograms.

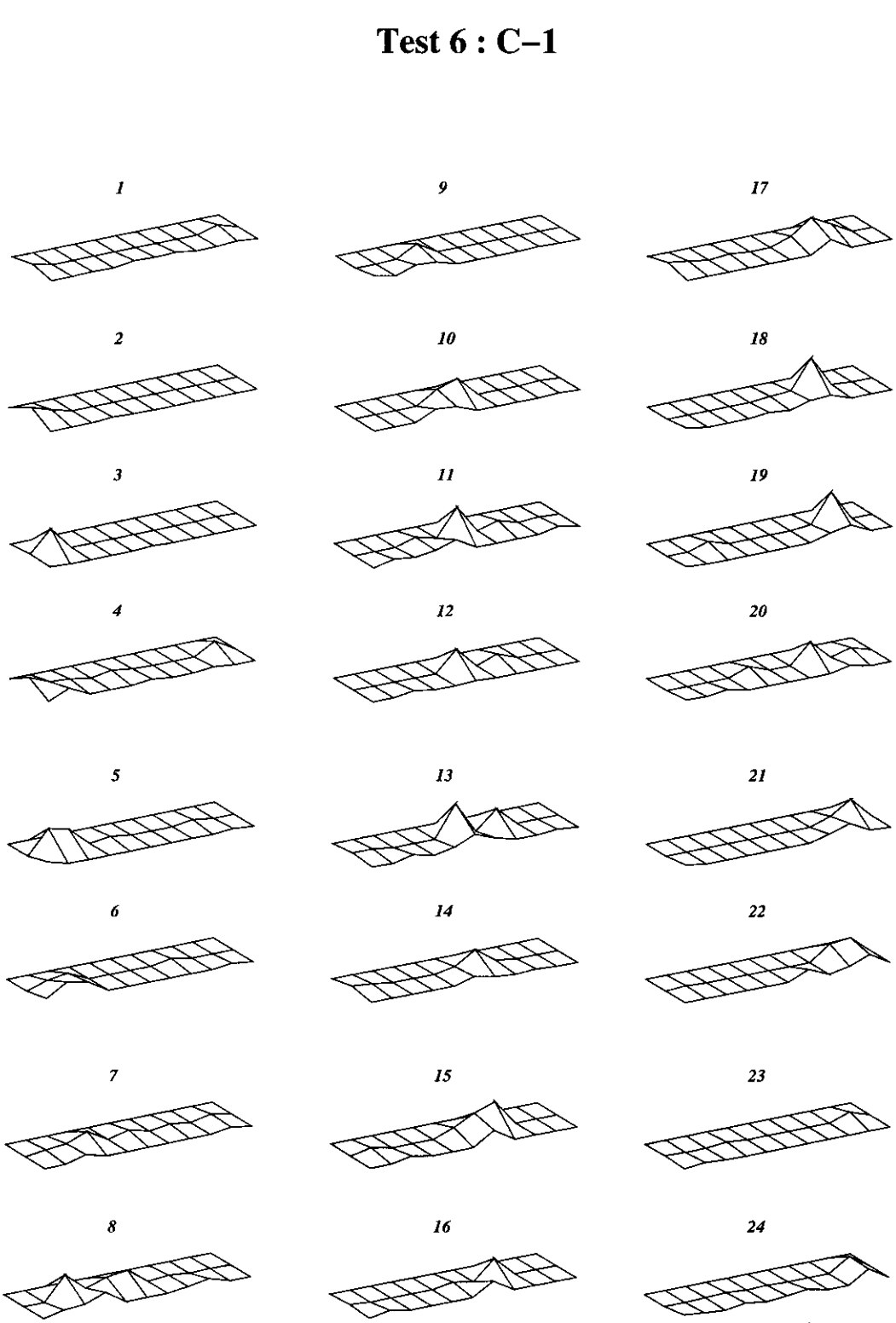

Figure 11. Same as Figure 10 but for Test 6 of C-1.

Case 3: Inversion using a different structure in the forward and in the inverse model

The effect of using an incorrect velocity structural model or an incorrect fault size and depth has been already studied by Das and Suhadolc (1996) and by Das et al. (1996). Using six stations they were unable to reproduce the rupture front correctly. In addition, they

Test 6 : C–2

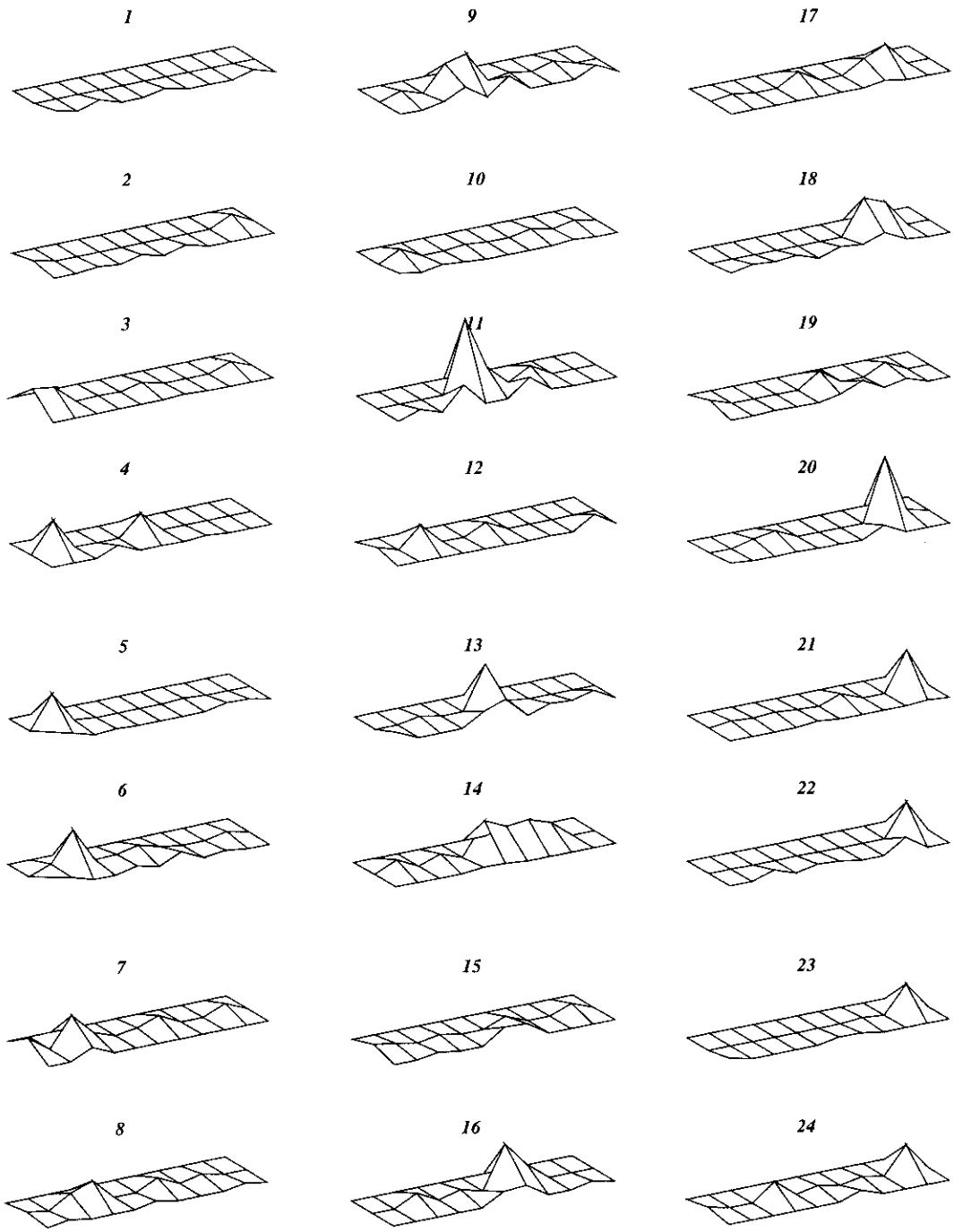

Figure 12. Same as Figure 10 but for Test 6 of C-2.

obtained some systematic moment behind the actual rupture front, which they called 'ghost front'. Here we study the effect of using an incorrect structure in the inversion when the inversion is performed using larger gridding than the forward problem, and when the artificial data also have some random noise added.

Test 6 : C–3

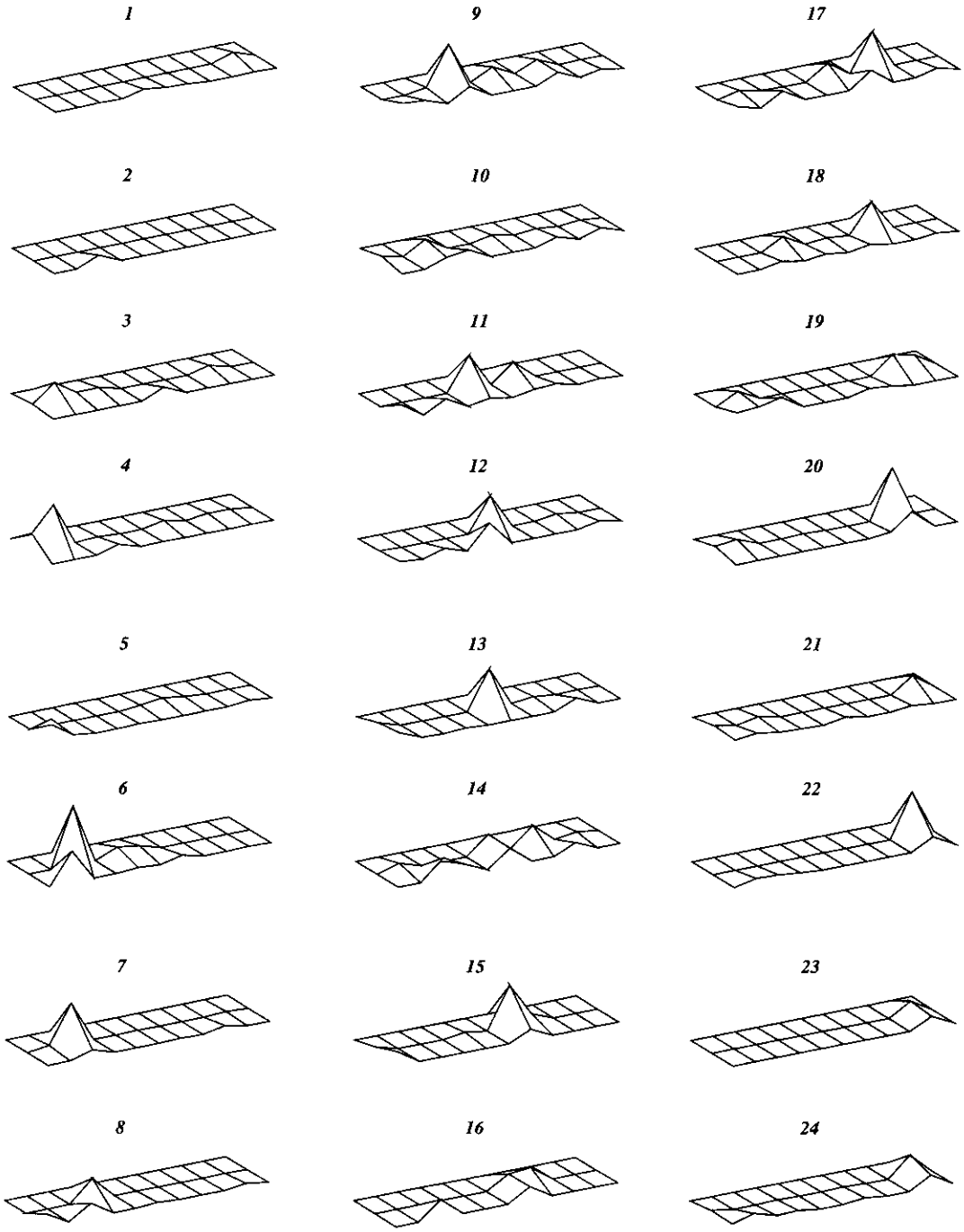

Figure 13. Same as in Figure 10 but for Test 6 of C-3.

The artificial data are computed for a spatial cell size of 0.250 km with a sampling frequency of 10.24 Hz in the medium M1 (solid line in Figure 3). The Green functions used in the inversion are computed for a cell size of 2 km and a temporal step of 0.8s with the structural model M2 (dashed line in Figure 3). The two structural

Test 6 : C–4

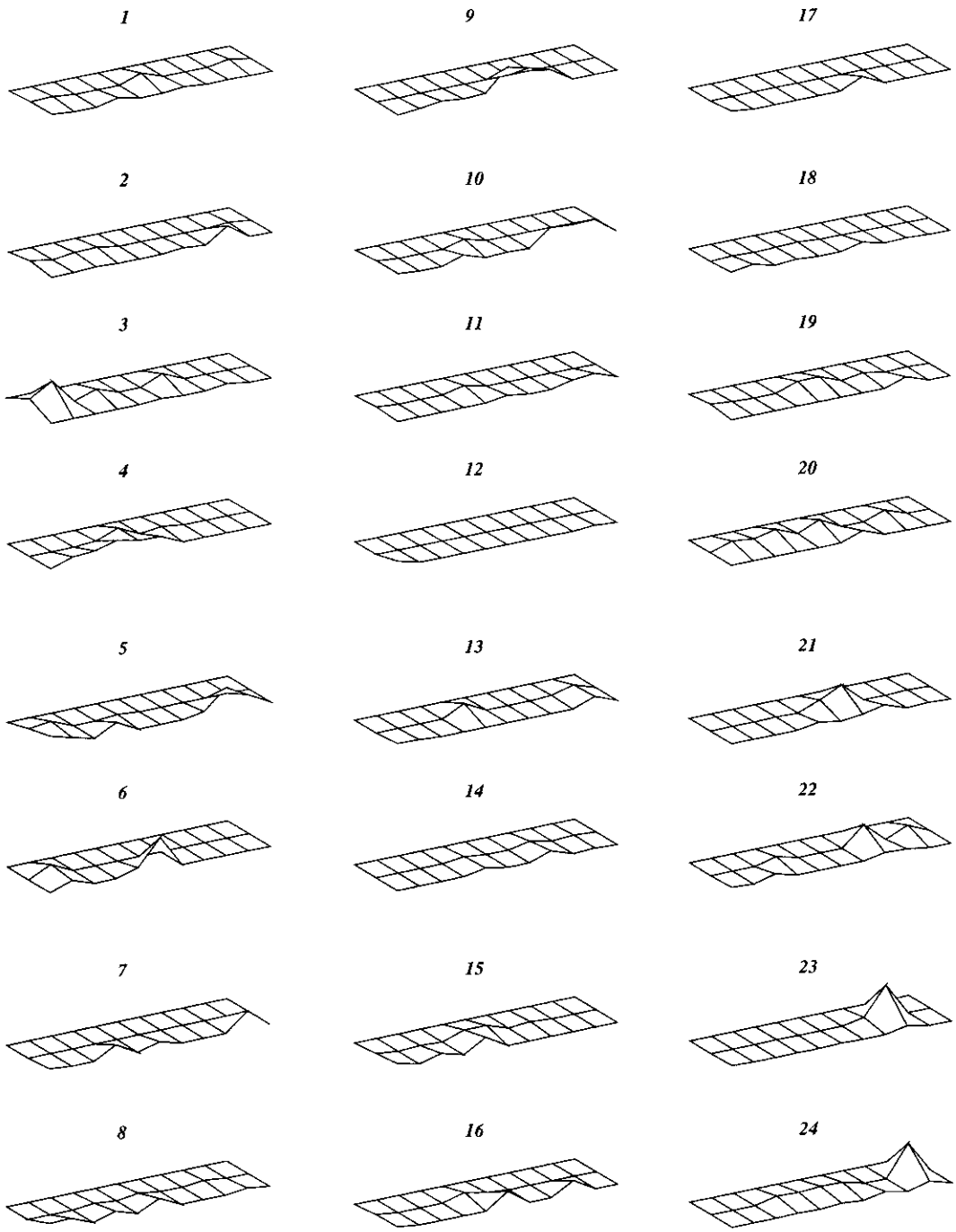

Figure 14. Same as in Figure 10 but for Test 6 of C-4.

models are deliberately chosen to be quite different to analyze a very unfavorable scenario. In most regions of the world, the velocity inaccuracies due to a poor knowledge of the structure are substantially larger than those in the very few well-investigated regions of the

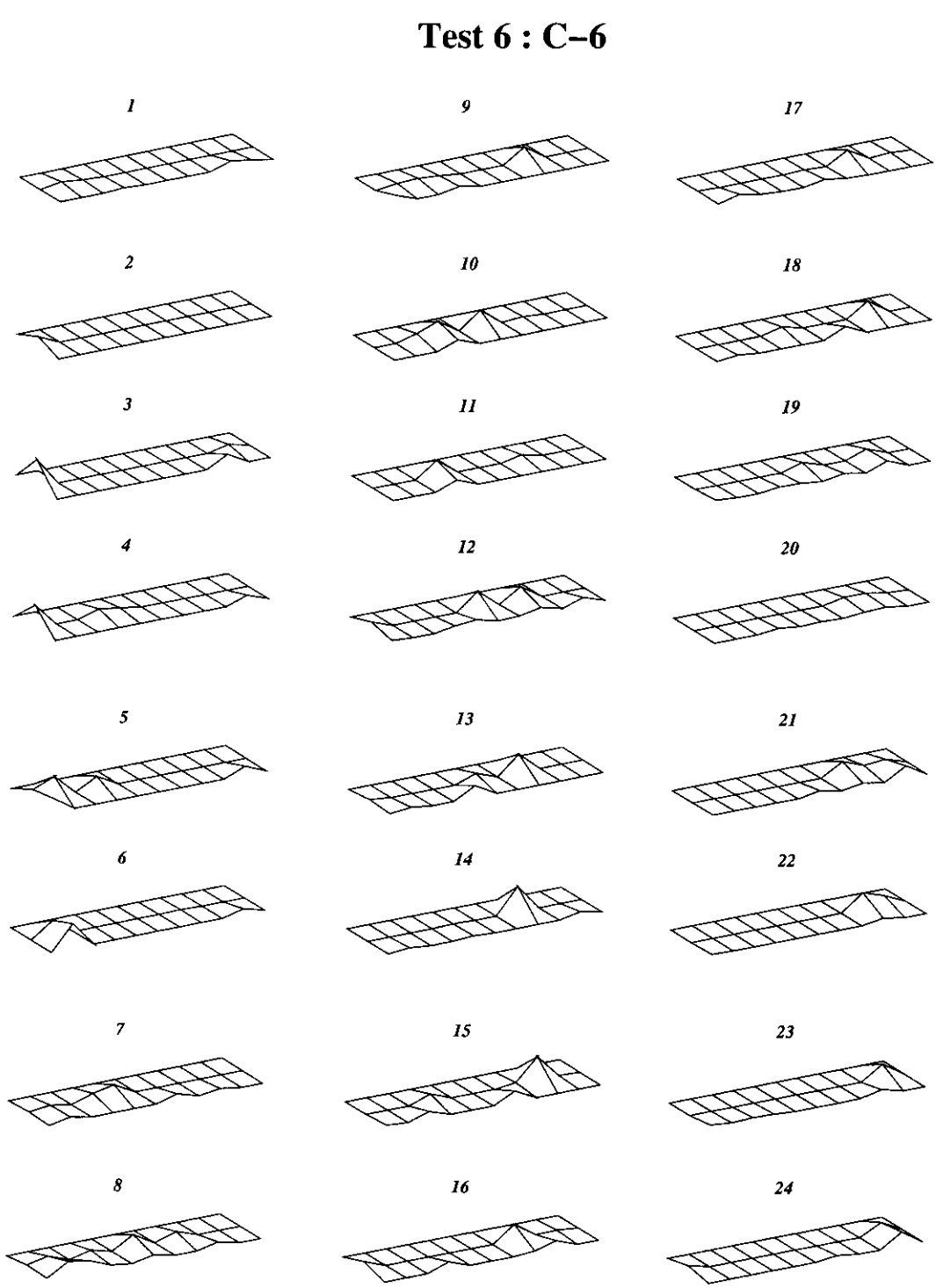

Figure 15. Same as in Figure 10 but for Test 6 of C-6.

world. The fault area and the fault mechanism are the same in the inverse and forward problem.

Test 10 – The fault model of the inversion has the same size, and for this test the top of the fault is placed at the same depth as that in the forward model. We fix the slip rate to be positive and the cells are free to slip as often as necessary. No causality condition is imposed on the rupture front. For all the station distributions we find that the fit of the accelerograms is poor and the rupture process is not well reproduced.

Test 11 – The moment value is fixed in the inversion and we use the same fault model as in Test 10. The fit

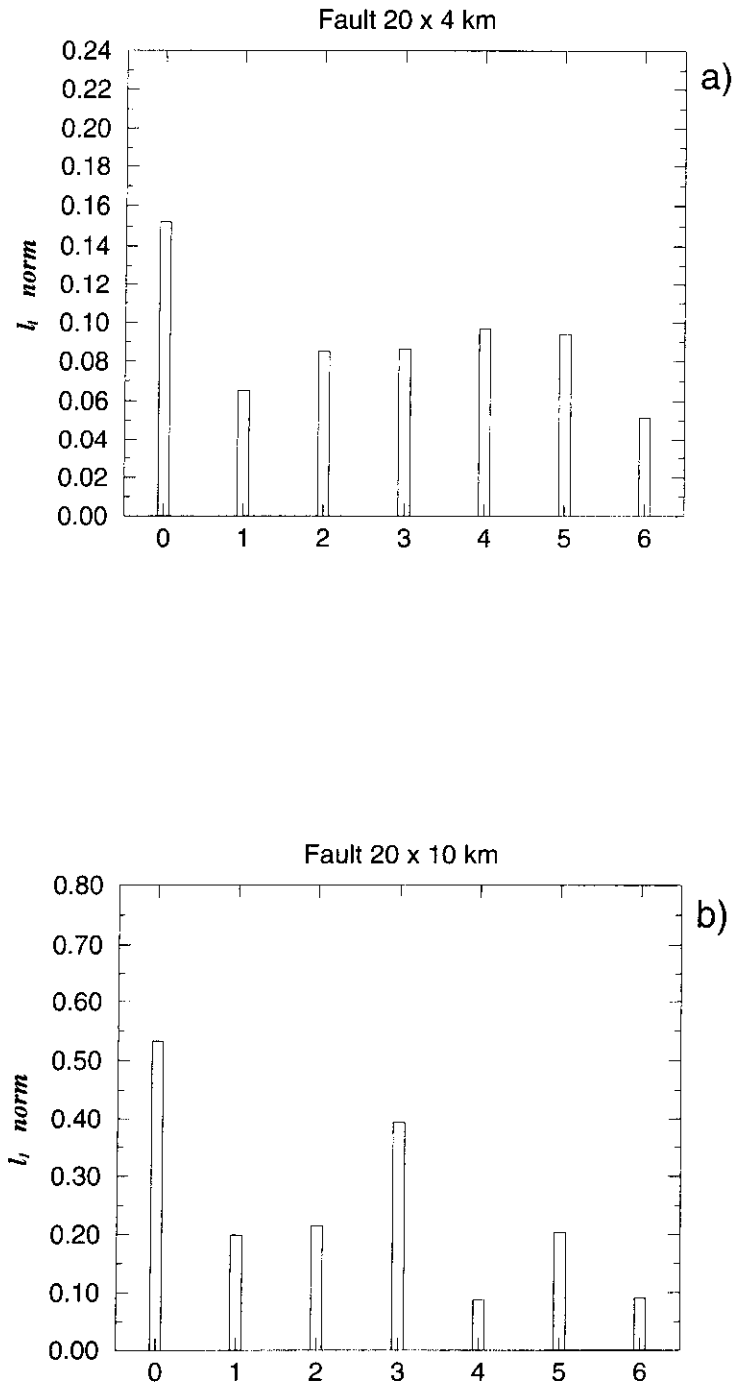

Figure 16. Misfits for different station configurations for (a) the 20 km × 4 km fault (b) the 20 km × 10 km fault.

of the accelerograms does not improve and the rupture front is still not well reproduced.

Test 12 – We place the fault with its top at a depth of 14 km. At this depth the first arrival times are compatible with those obtained for the forward case. The solutions are not well reproduced even with additional constraints. The fit of the accelerograms is shown in Figure 19 and the moment rate in Figure 20. We can identify the rupture front and we do not see any other systematic moment rate behind or ahead of the rupture front. However, a few, small scattered areas with non-zero moment rates are seen over the fault surface, including in the acausal regions. Fixing the value of moment does not improve the results. Thus, we are

Test 7 : C–2

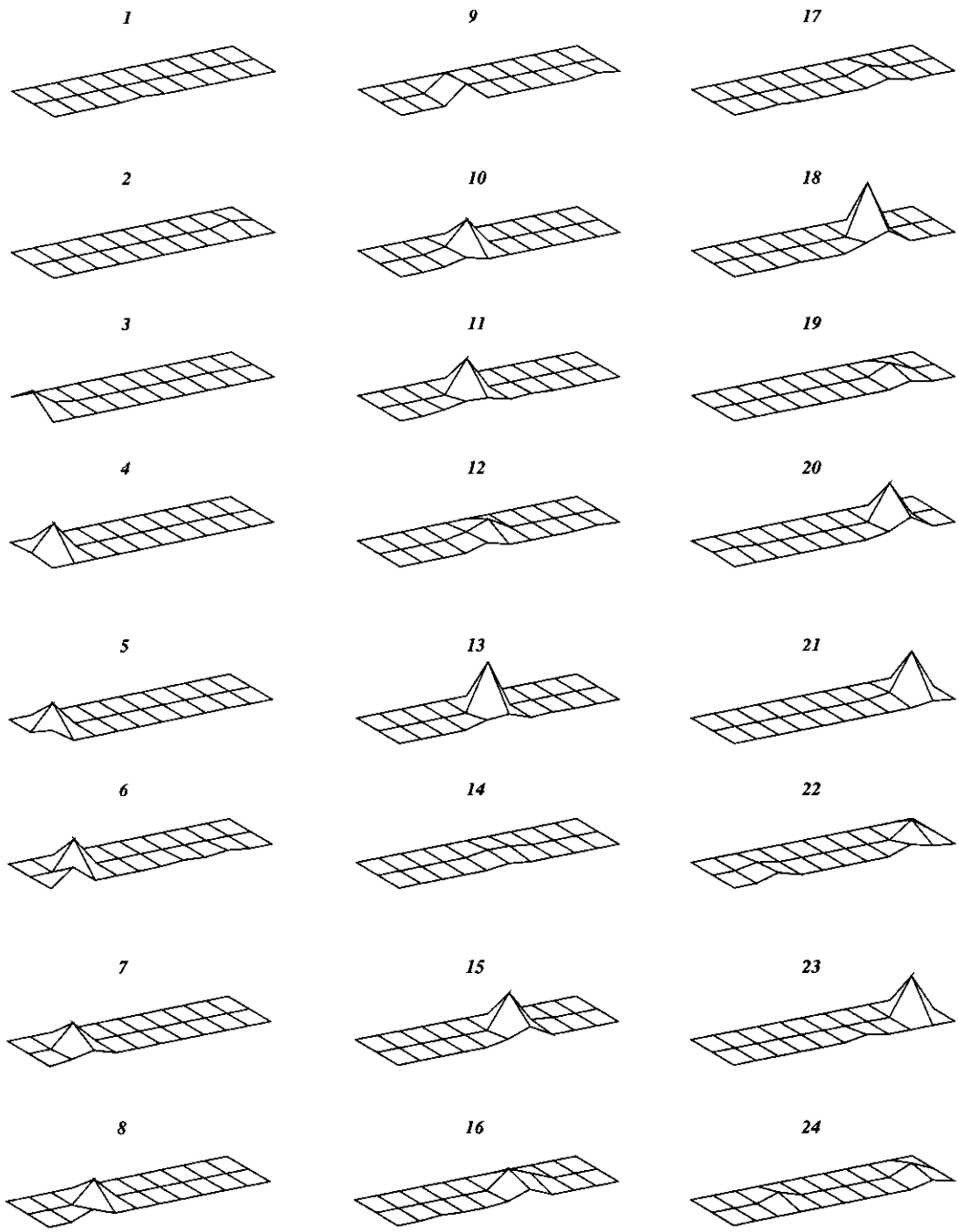

Figure 17. Same as in Figure 10 but for Test 7 of C-2.

unable to fit the data and to reproduce the moment rate distribution in space and time, when a different structure is used in the inverse model, in spite of good azimuthal coverage and many more stations (twelve) than is generally available for strong ground motion data. This is, however, the most realistic case and sug-

Test 7 : C–4

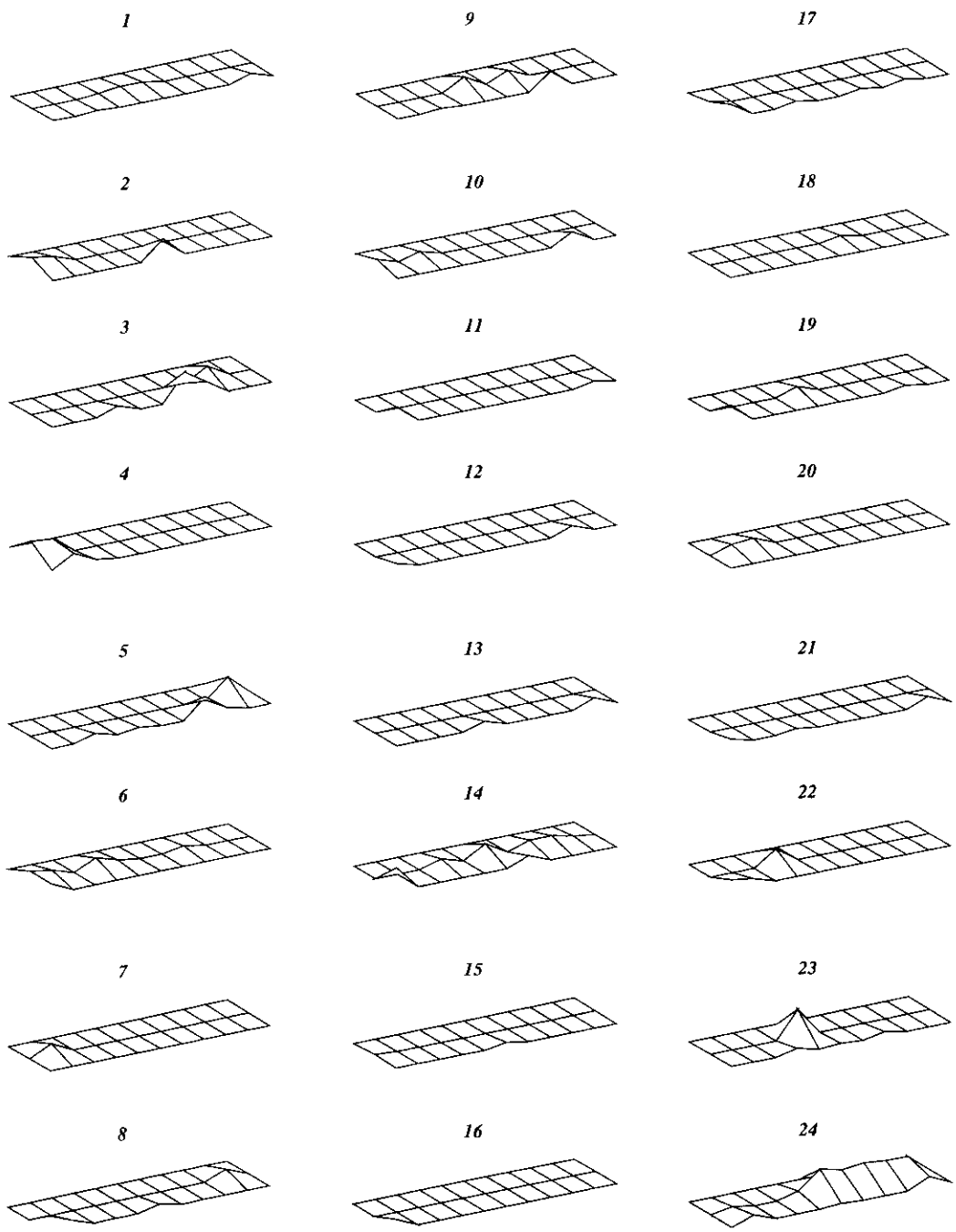

Figure 18. Same as in Figure 10 but for Test 7 of C-4.

gests that good structural information at the source is essential to reliably determine the seismic moment rate history and distribution on a fault.

Test 13 – We performed an inversion using the much shorter time window of 20s of data to see if the solution

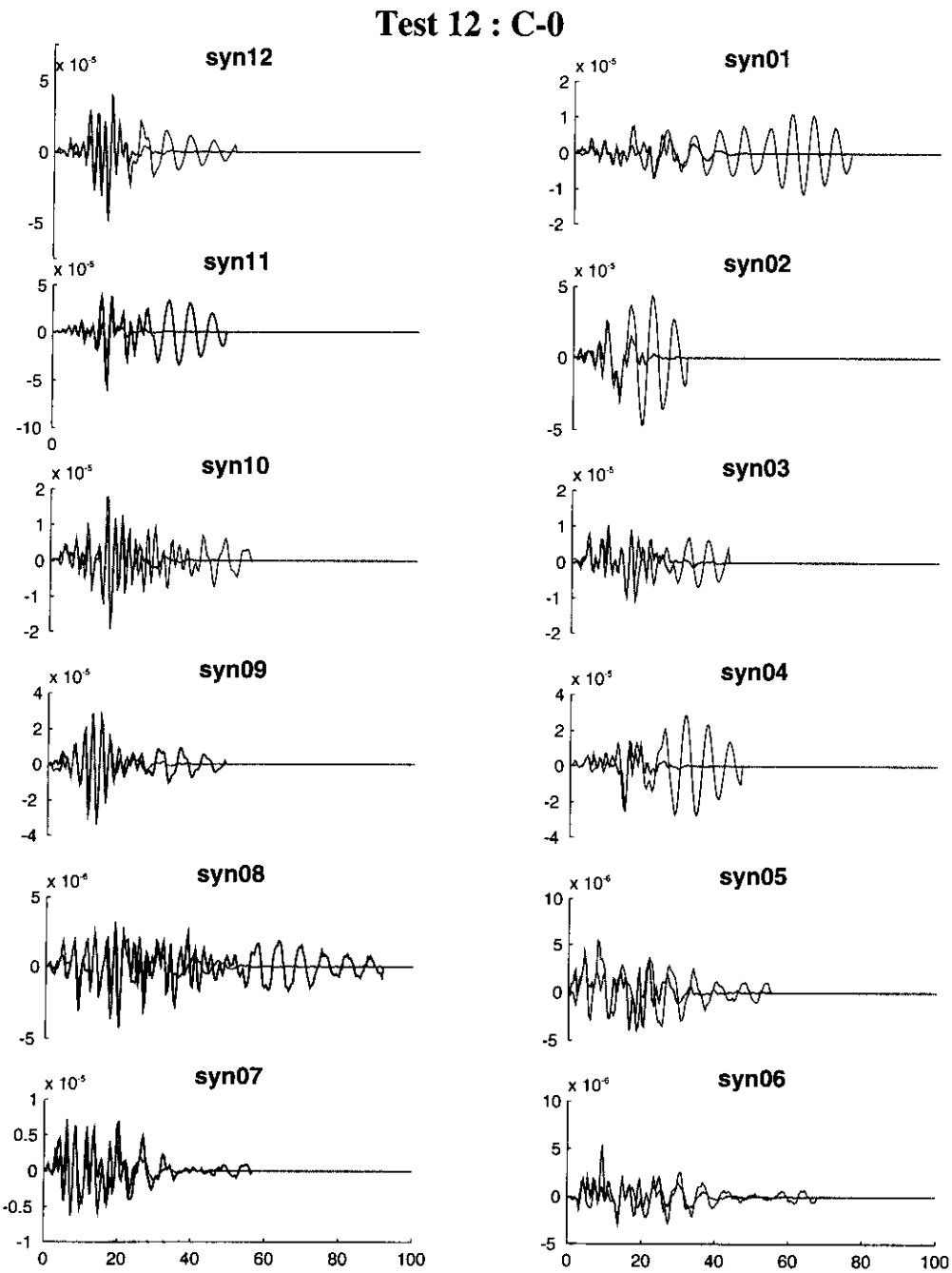

Figure 19. The comparison of the artificial data (solid lines) to the solution accelerograms (dotted lines) for Test 12 for C-0.

is affected. We find that the data are still not well fitted and the solution does not improve.

Results for the 20 km × 10 km fault

Till now, we have considered a fault with an aspect ratio of 1 to 5 which is mainly seen for great events (the 1957 Rat Island earthquake, the 1960 Chilean earthquake, the 1964 Alaska earthquakes, for example) but not usually for smaller events. So we study a fault with the aspect ratio of 1 to 2 which is close to the typical aspect ratio seen for shallow thrust faults (Wells & Coppersmith, 1994). We consider a fault that is 20 km long and 10 km wide. The top of the fault is at 5 km and the tests we performed are reported in the flow-

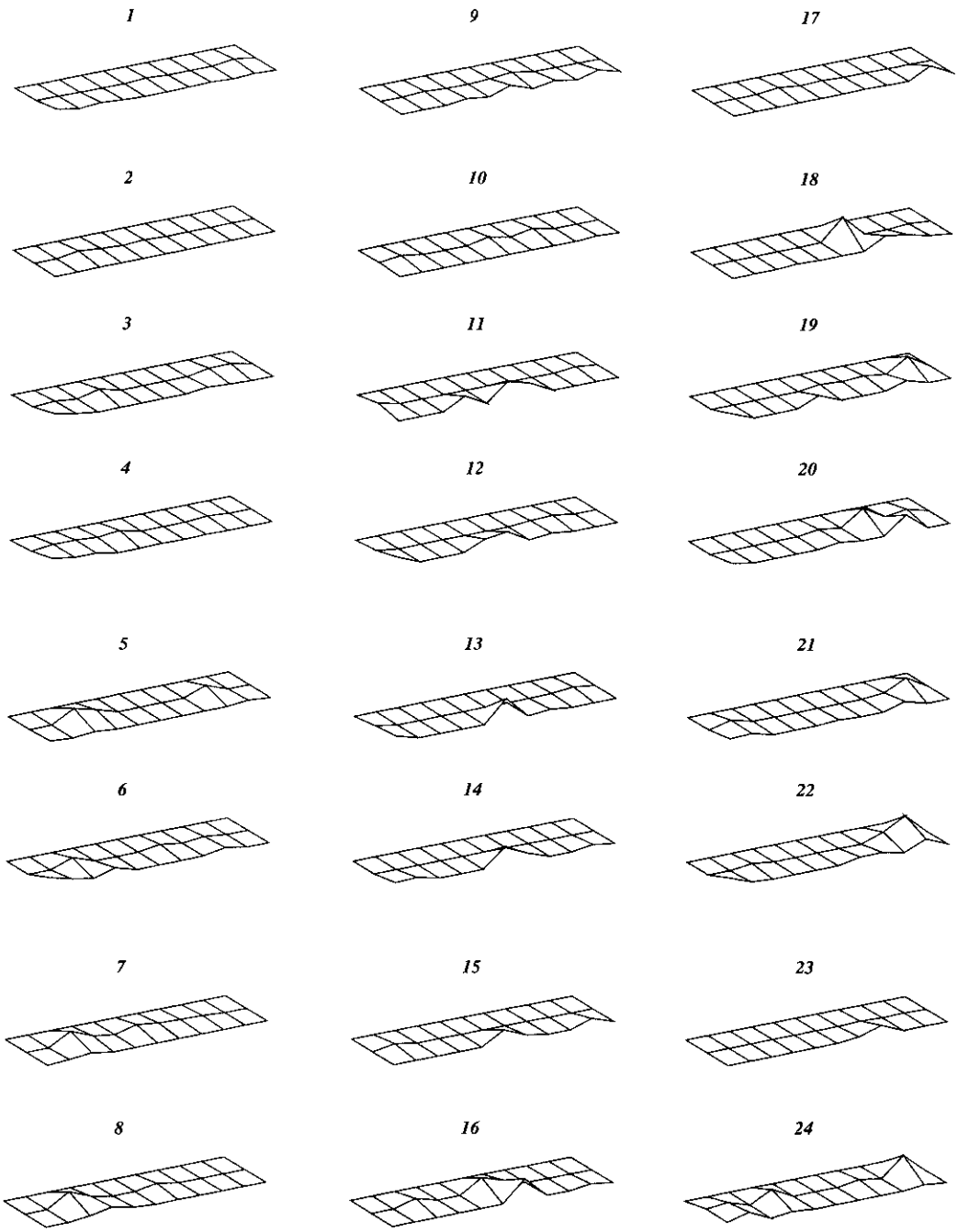

Figure 20. The moment rate maps in time produced by the inversion in Test 12 for C-0.

chart of Figure 5b and in Table 1. With the new fault geometry, we repeated most of the tests of the previous section for Cases 1 and 2 (Table 1); we inverted for the same grid size in space and in time for the forward and the inverse case, as well as for larger cells sizes in the inversion than in the forward case; we also added 5% of noise as we did before. Our main results do not change due to the changing of the aspect ratio, as it

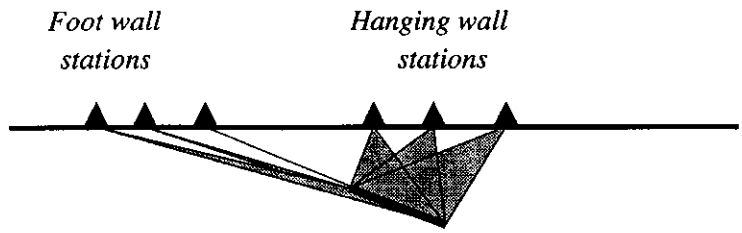

Figure 21. Schematic explanation of the difference between the illumination of the fault by stations located on the foot wall and on the hanging wall.

can be seen by the values of the misfit we report in Figure 16b.

Discussion and Conclusions

The aim of this study was to determine how reliably one can invert accelerograms to determine the rupture process details, when the station configuration is less than optimal. We show that the solutions can be improved by using well-established physical constraints, to reduce the effect of the less-than-optimal station coverage in the inversion. In some cases, we deliberately chose a very unfavorable scenario, since our purpose was to determine which properties of the faulting process could still be reliably obtained, if any.

For a dipping fault, we show that the best configuration is when the stations are on the hanging wall and six stations on the hanging wall are enough to obtain the moment rate history and distribution. The stations on the hanging wall are closer to the fault surface but the better result is also due to the better illumination of the fault by the hanging wall stations, as is illustrated schematically in Figure 21. Further, we find that the solution for the C-1 configuration, with six stations all located on the hanging wall side of the fault, is better than that for configuration C-0 with twelve uniformly distributed stations. It may appear surprising at first glance that adding the six footwall stations produces a poorer solution. But since the footwall stations illuminate the fault less well, their contribution to the Green function matrix A worsens its condition number. This provides incentive to install permanent ocean bottom strong ground motion stations in subduction zones. Thus the azimuthal distribution and the resulting illumination of the fault is more important than simply the number of stations. For a fault dipping more shallowly than that considered in this paper, the illumination effect discussed above will be even more pronounced.

Placing only four stations in the forward direction relative to the rupture propagation, was sufficient to recover the solution well. On the other hand, four stations placed in the backward direction produced a poorer solution, though the main features of the rupturing process were still obtained. Finally, we were unable to determine the details of the rupturing process when using a different source medium structure than the correct one, even though the overall picture of the moment rate distribution could still be recovered. Our point in using very different structure in the inversion was to show that though we can compensate for poor station coverage by using constraints, very incorrect structure cannot be compensated for by any means. Thus at regional distances using an incorrect source Earth structure, it is difficult to distinguish between the true source properties and artefacts generated by the incorrect medium properties, even with an optimal station distribution and additional physical constraints. Except in a very few intensively studied regions of the world (for example, California) the crustal structure unfortunately remains poorly known even today. Our study shows that some gross features of the faulting process can be obtained even in that case, though not the finer details.

Acknowledgements

We are very grateful to Dave Wald and an anonymous reviewer for a thorough review of the manuscript, which helped to improve it significantly. This study was partially supported by EC program, Environment and Climate, Topic IV.1.1, Natural Risks – Seismic Hazard, under the ENVIRONMENT contracts EN5V-CT94-0513 and ENV4-CT96-0296. The computations were done on the Cray J932-SN9522 at the Rutherford-Appleton Laboratories, Didcot, UK under a Supercomputing grant obtained through the Natural Environmental Research Council of the U.K. and on

the Cray J916/8-1024 at Centro di Calcolo of the University of Trieste, Italy.

References

Bernard, P., Gariel, J. C. & Dorbath, L., 1997. Fault location and rupture kinematics of the magnitude 6.8, 1992 Erzincan earthquake, Turkey from strong ground motion and regional records, *Bull. Seismol. Soc. Am.* **87**,5, 1230–1293.

Beroza, G. C. & Spudich, P., 1988. Linearized inversion for fault rupture behavior: application to the 1984, Morgan Hill, California earthquake, *J. Geophys. Res.* **93**, 6275–6296.

Das, S. & Kostrov, B. V., 1990. Inversion for seismic slip rate and distribution with stabilizing constraints: Application to the 1986 Andreanof Islands earthquake, *J. Geophys. Res.* **95**, 6899–6913.

Das, S. & Kostrov, B. V., 1994. Diversity of solutions of the problem of earthquake faulting inversion. Application to SH waves for the great 1989 Macquarie Ridge earthquake, *Phys. Earth Planet. Int.* **85**, 293–318.

Das, S. & Suhadolc, P., 1996. On the inverse problem for earthquake rupture. The Haskell-type source model, *J. Geophys. Res.* **101**, 5725–5738.

Das, S., Suhadolc, P. & Kostrov, B. V., 1996. Realistic inversions to obtain gross properties of the earthquake faulting process, *Tectonophysics*. In: C. Trifu (ed.), Special issue entitled Seismic Source Parameters: from Microearthquakes to Large Events **261**, 165–177.

Hartzell, S. H. & Heaton, T. H., 1983. Inversion of strong-ground motion and teleseismic waveform data for the fault rupture history of the 1979 Imperial Valley, California earthquake, *Bull. Seismol. Soc. Am.* **73**, 1553–1583.

Hwang, P. Y., 1985. Focal depths and mechanisms of mid-ocean ridge earthquakes from body waveform analysis, Ph. D. thesis, Massachusetts Institute of Technology, pp. 36–39.

Iida, M., Miyatake, T. & Shimazaki, K., 1990. Relationship between strong-motion array parameters and the accuracy of source inversion and physical waves, *Bull. Seismol. Soc. Am.* **80**, 1533–1552.

Iida, M., 1993. Source effects on strong-motion records and resolving power of strong-motion arrays for source inversion, *Tectonophysics* **218**, 179–193.

Kostrov, B. V. & S. Das, 1988. Principles of earthquake source mechanics, *Appl. Math. Mech. Ser.*, Cambridge University Press, New York, 286 pp.

Madariaga, R., 1977. High-frequency radiation from crack (stress drop) models of earthquake faulting, *Geophys. J.* **51**, 625–651.

Menke, W., 1985. Imaging fault slip using teleseismic waveforms: analysis of a typical incomplete tomography problem, *Geophys. J. Roy. As. Soc.* **81**, 197–204.

Miyatake, T., Iida, M. & Shiamazaki, K., 1986. The effects of strong motion array configuration on source inversion, *Bull. Seismol. Soc. Am.* **76**, 1173–1185.

Olson, A. H. & Anderson, J. G., 1988. Implications of frequency-domain inversion of earthquake ground motions for resolving the space-time dependence of slip on an extended fault, *Geophys. J.* **94**, 443–455.

Panza, G. F. & Suhadolc, P., 1987. Complete strong motion synthetics. In: B. A. Bolt (ed.) Seismic Strong Motion Synthetics, Computational Tecniques 4, Academic Press, Orlando, pp. 153–204.

Satake K., 1985. Effects of station coverage on moment tensor inversion, *Bull. Seismol. Soc. Am.* **75**, 1657–1667.

Stump, B. W. & Johnson, L. R., 1977. The determination of source properties by the linear inversion of seismograms, *Bull. Seismol. Soc. Am.* **67**, 1489–1502.

Wells, D. L. & Coppersmith, K. J., 1994. New empirical relationships among magnitude, rupture length, rupture width, rupture area, and surface displacement, *Bull. Seismol. Soc. Am.* **84**, 974–1002.

GEOPHYSICAL RESEARCH LETTERS, VOL. 27, NO. 4, PAGES 577-580, FEBRUARY 15, 2000

The 1976 Friuli (NE Italy) Thrust Faulting Earthquake: A Reappraisal 23 Years Later

A. Aoudia,[1] A. Saraó,[2] B. Bukchin,[3] and P. Suhadolc[2]

Abstract. We revisit the 1976 Friuli earthquake sequence by combining hypocenters relocation, long period surface wave inversion, field geology and strong motion modelling. We show that fault-related folding is the main active deformation by which the seismic energy was released during the main shock (Ms=6.5) and that some of the surface effects reported in 1976 correspond to widespread bedding planes displacements induced by flexural-slip folding. The fault evolved from blind to semi-blind along strike showing the control of the inherited structural geology on the fault surface break and rupture arrest. Our fault model produces waveforms that fit the accelerograms recorded in the area.

Introduction

The May 6, 1976 Friuli earthquake (Ms = 6.5) is the largest so far recorded event in Northern Italy. It took place in the Southern Alps within the active collision zone between Eurasia and Adria that undergoes 4 to 5 mm/year of crustal shortening [*Anderson and Jackson*, 1987; *De Mets et al.*, 1990].

The Friuli main shock was preceded by a M 4.5 foreshock, and followed by a strong aftershock sequence. The largest aftershocks occurred in September 15th, 1976, at 03:15 (Ms=6.0) and 09:21 GMT (Ms=6.1). The area has therefore sustained a high seismic strain, which if released simultaneously, could have produced quite a large earthquake. This peculiar earthquake sequence has been the subject of several studies [*Ambraseys*, 1976; *Amato et al.*, 1976; *Finetti et al.*, 1976; *Lyon-Caen*, 1980; *Cipar*, 1980], but the causative geological structure and related fault-rupture process remained unknown.

In this paper, we relocate the main shock and strongest aftershocks. We invert the surface waves of the main shock and two strongest aftershocks to retrieve their mechanism and depth. We perform quantitative landform analysis and field investigations supplemented by the analysis of pre and post earthquake aerial photos to assess the nature and patterns of Quaternary deformation in the epicentral area. Merging together our new results with the reported 1976 field observations we propose a fault-rupture model for the 1976 Friuli earthquake and simulate the related acceleration field for frequencies lower than 1 Hz. Data analysis and other relevant details are in *Aoudia* [1998].

[1]Dipartimento di Scienze della Terra, Università di Trieste, and Abdus Salam International Centre for Theoretical Physics, SAND Group, Trieste, Italy.

[2]Dipartimento di Scienze della Terra, Università di Trieste, Italy.

[3]Institute of Earthquake Prediction and Mathematical Geophysics, Moscow, Russia.

Paper number 1999GL011071.
0094-8276/00/1999GL011071$05.00

Earthquake Relocation

The main shock and strongest aftershocks were well recorded by several WWSSN stations. We use JHD and modified single-event methods [*Dewey*, 1971] to relocate the epicenters of 34 earthquakes (M>4.2) of the Friuli earthquake sequence that occurred in 1976 and 1977. The M>5.2 events produced good quality P-wave readings, while for the others good Pg and Lg readings are available. To test the stability of our results we use two different calibration events located by IPGS and OGS local networks and widely recorded by WWSSN stations. Station corrections and their variances were estimated for 210 station-phase pairs for phases at regional, near teleseismic, and far-teleseismic distances. The relocated 34 events along with other aftershock data located by a local network and reported in *Granet and Hoang* [1980] are plotted in Fig. 1. The aftershocks cover a surface 25 km long and 15 km wide, a region comparable to the expected fault surface implied by the source mechanism. All the aftershocks are distributed to the west of the main shock (Fig. 1). This pattern suggests a unilateral and westward rupture propagation. The maximum depth extent of the aftershocks is approximately 14 km, most of them being at 5 km.

Source parameters

To retrieve the source parameters of the main shock and two largest aftershocks, we use the joint inversion method of long-period surface wave spectra described by *Bukchin et al.* [1994]. We make use of the recently recalibrated HGLP digital data [*Ekstrom and Nettles*, 1997] together with long-period data from the early Seismic Research Observatory (SRO) of the GDSN. The estimation of moment tensor and source depth in the instantaneous point source approximation is done by inverting Love and Rayleigh fundamental mode spectra.

The mechanism and scalar seismic moment we obtain for the main shock (strike=288°, dip=29°, slip=112°, and $M_0 = 0.57 * 10^{19} Nm$) are very similar to the recently computed Harvard source parameters [*Ekstrom and Nettles*, 1997]. Our solution is also similar to the mechanism computed by *Cipar* [1980], but rather different from the one estimated by *Lyon Caen* [1980] from P-wave first arrival polarities. Varying the possible depth of the source, we calculate the residuals between observed and synthetic spectra for every trial value of depth. The residuals reaches its minimum value between 4 and 6 km of centroid depth.

For the September 15th aftershocks, we could not retrieve a reasonable estimate of depth. We fix the depth at 8 km, the average of the different values proposed in the lit-

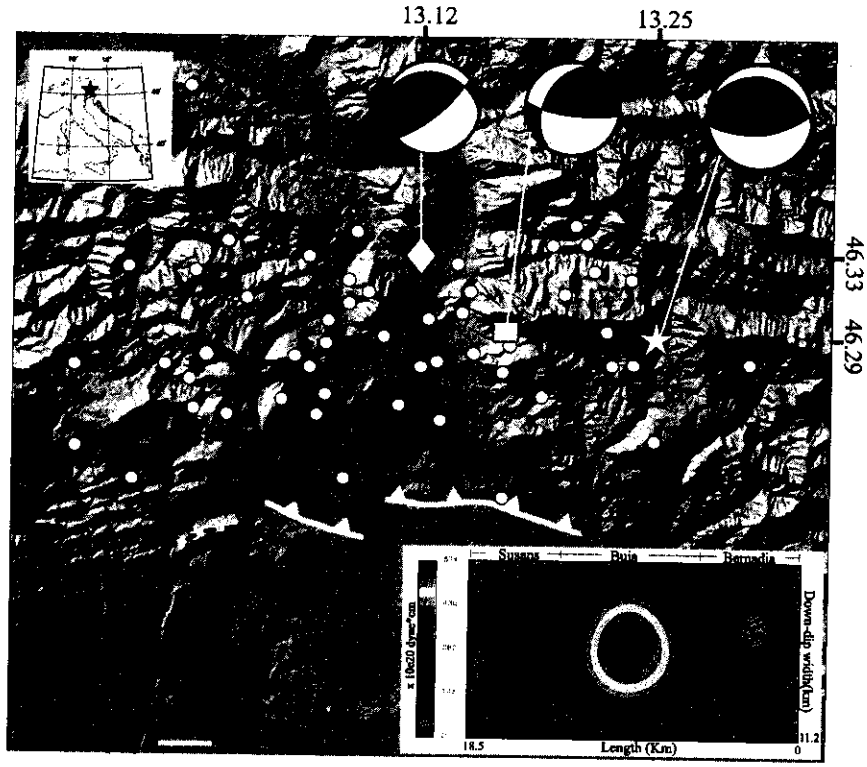

Figure 1. Fault model of the 1976 Friuli earthquake and moment release history used to compute the synthetic strong motions. The white barbed lines are the vertical projection of the top of the blind thrusts while the black line corresponds to an emergent thrust. The fault plane solutions for the main shock (star) and the September 15th aftershocks 3:15 (square) and 9:21 GMT (diamond) are also shown. The triangle refers to the AGIP oil well.

erature. For the 03:15 aftershock the computed mechanism shows a large strike-slip component (strike=204°, dip=36°, slip=21°, and $M_0 = 0.87 * 10^{18} Nm$) when compared to the Harvard CMT solution. The second aftershock solution (strike=288°, dip=28°, slip=144°, and $M_0 = 0.98 * 10^{18} Nm$) is very close to the solutions estimated by *Cipar* [1980], *Lyon Caen* [1980] and *Anderson and Jackson* [1987].

Earthquake Geology

To orient our field investigations, we couple JHD and long-period seismology results with high-resolution digital elevation models (DEM) and GIS surface analysis in an area with a dense vegetation cover. We focus on the most relevant surface effects reported by *Martinis and Cavallin* [1976] and *Ambraseys* [1976]. Those reported by *Bosi et al.* [1976] are located almost at the same latitude as the epicenter, and the field investigations and DEM surface analysis [*Aoudia*, 1998] revealed that the crack locations outlines the contact between Eocene Flysch and Mesozoic limestones representing the uppermost limit of a large paleolandslide.

The Bernadia structure is the only prominent geological structure located 10 km to the south of the epicenter (Fig. 1). It is a basement fault-bend fold covered unconformably by fluvial and fluvio-glacial deposits. The steep south limb and gentle north-dipping back limb require a north-dipping thrust and constrain the dip of the fault to a range of 30-45° (Fig. 2). Figure 2 shows the most striking geomorphic landforms apparent in the front limbs of the fold. The terrace T1 with no apparent tilt or folding sits 50 meters above the modern main Torre river and exhibits the same slope as the Torre. Other terraces appear in the front of T1 and are deformed and back-tilted by a set of N075 to E-W high-angle reverse ramps. This suggests a flat geometry of the frontal thrust. The investigation of pre and post earthquake aerial photos did not reveal any surface faulting of the ramps.

The Buia ridge (Fig. 1) is the only relief that outcrops in the middle of the Tagliamento morainic amphitheatre.

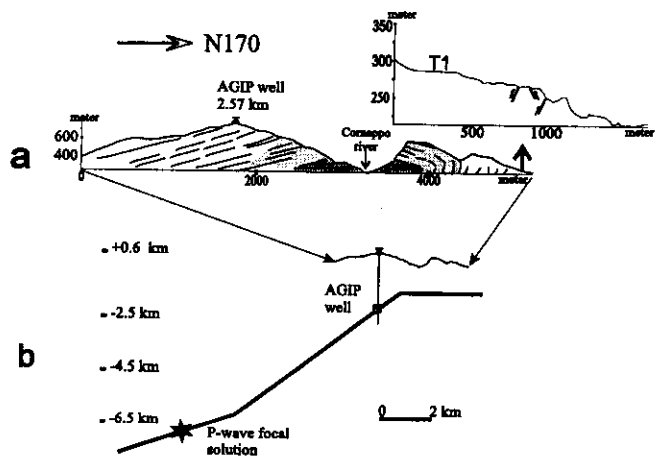

Figure 2. (a) Bernadia field cross-section (see AGIP oil well in Fig. 1 for location) and 5 meter DEM topographic profile at the front of the fold. (b) The integration of the P-wave solution (depth 7 km, dip 19°, strike 260°), the 2.57 km deep oil well *(AGIP, 1959)*, the basement geology along with the surface geology and geomorphology allow us to outline the geometry of the Bernadia thrust.

The denudation of its morainic cover has been attributed by *Carraro et al.* [1982] to vertical deformation. In the field, a thrust places Flysch deposits on top of vertical conglomerates that exhibit slip along their beddings. The Buia structure is probably the surface expression of the anticline that runs W-NW imaged on seismic profiles [*Amato et al.*, 1976] which is related to a fault that is illuminated by the aftershocks in *Finetti et al.* [1976]. The aerial photos did not reveal any surface faulting. The surface projection of the Buia thrust corresponds to the maximum isoseismal of *Giorgetti* [1976].

The N120 Susans ridge (Fig. 1) is made of fluvio-glacial deposits and south-dipping N120 striking conglomerates and sands. *Ambraseys* [1976] described cracks north of Susans ridge and parallel to its strike over a length of 500 meters. The origin was defined as non tectonic. In the field numerous bedding-plane are experiencing widespread flexural slip consistent with a north-dipping blind thrust (Fig. 3). A south dipping high-angle reverse fault offseting the Miocene sand is well exposed at the northern flank of the ridge (Fig. 3). Its location is in good agreement with the surface breaks reported by *Ambraseys* [1976]. The fault acts probably as a backthrust above the main north-dipping blind thrust and the recent activity is highlighted by the presence of wind gaps associated with the Tagliamento river at the western tip of the fold, where tilted alluvial terraces are exposed.

To the west, the N120 trending Susans structure terminates in a pure alpine NE-SW trending system (Fig. 1), represented by the Ragogna ridge. It is a Neogene flexural-slip anticline that extends 18 km along the range front. It is made of marls and clay units interstratified with stiff conglomerates. Widespread NE-SW ground cracks were mapped and well described by *Martinis and Cavallin* [1976] along the bedding-planes of the first 4 km of Ragogna structure towards Susans. The cracks did not show any reactivation during the September aftershocks and were attributed to gravity effects although the authors description suggests a tectonic origin. Our field investigations reveals that these cracks are expressions of slips on bedding-planes distributed over a wide zone. Where Martinis and Cavallin described the most spectacular cracks (20 cm of offset), we found an offset man-made wall, with a maximum slip of 50 cm, which coincides with a 6 meter cumulative bedding plane fault scarp exposed on a river terrace. We suggest that the 50 cm slip has been generated by coseismic folding during the 1976 main shock.

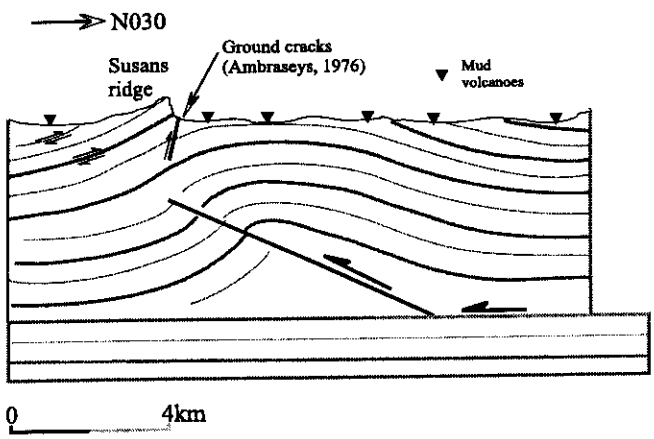

Figure 3. Interpretative cross-section through Susans. Susans ridge is probably the surface expression of a fault-propagation fold associated with a blind thrust ramp. Folding induces flexural-slip on bedding-planes. Depth countours are derived from seismic reflection studies *(AGIP, 1959; Amato et al., 1976)*.

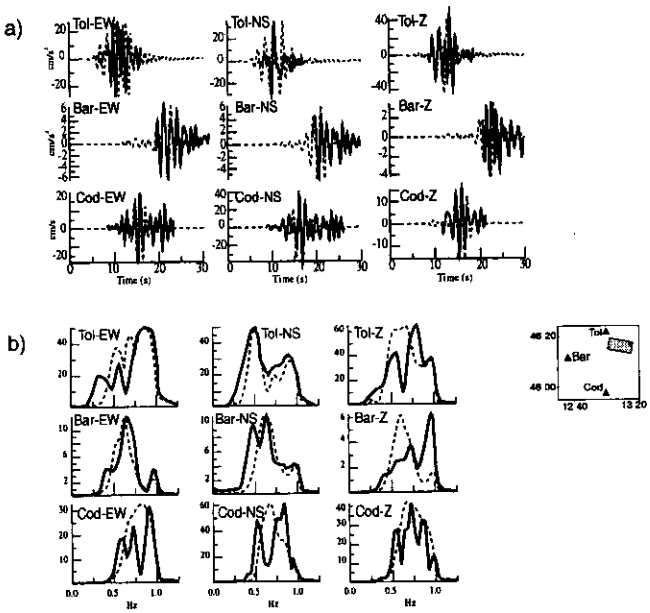

Figure 4. Comparison between three-component (a) real (solid line) and synthetic (dashed line) accelerograms; (b) real and synthetic spectra. The stations used are plotted on the map.

Conclusions: Fault Model and Strong Motion Modelling

Our data show that the Friuli earthquake rupture is related to a 19 km fault-related folding evolving from blind faulting beneath the Bernadia and Buia basement-involved structures to semi-blind faulting beneath the Neogene Susans structure (Fig. 1). The rupture ended up in Ragogna fold. The geometry of this fold relative to the N120 structure (interlimb angle of 130°) and the large slip it sustained are consistent with the flexural-slip process and a model where the surface sediments buckle at the end of a propagating rupture. The gravity field shows that the Bernadia is seen as an E-W to NE-SW trending -60 mGal low [*Amato et al.*, 1976] in agreement with the surface geology and the P-wave focal solution. The gravity low steps southwestward and continues uninterrupted across the plain, beneath Buia and Susans, on a N120 strike in agreement with our centroid solution. The above data and interpretation suggest a relatively shallower slip depth extent westward along the fault consistent with the westward shifted course of the Tagliamento river when nearing the N120 fold system (Fig. 1).

Using our fault model and the method of multimodal summation [*Panza*, 1985] for extended sources [*Panza and Suhadolc*, 1987; *Saraò et al.*, 1998], we compute synthetic accelerograms for three analogic strong motion stations that recorded the main shock. The quality of the available data is rather poor: lack of origin time and sometimes high level of noise make source studies by waveform inversion impos-

sible. Nevertheless, we use some real data for a qualitative comparison with synthetics generated by forward modelling. In our deterministic approach the extended source is a rectangular plane discretized into a grid of point sources. The rupture propagates at a constant speed of 70% of the shear-wave velocity of the medium. We use a fault rupture area of 18.5 km length by 11.2 km width (Fig. 1). The top of the fault is at a depth of 1.5 km and the nucleation point is 7 km deep. We place patches of high energy release in the location of the three fault segments and we smooth the slip distribution at the edges of the fault by a 2-D cosine tapering function. To image these segments seismic waves at least with frequencies up to 1 Hz (corresponding to wavelengths of about 3 km) should be considered. The comparison (Fig. 4) between real and synthetic accelerograms and spectra shows that, in the computed frequency range 0.25-1.00 Hz using a one-dimension structural model the proposed fault model reproduces the strong motion observations. We suggest that the lack of slip at the surface can be explained by flexural-slip folding.

The 1976 Friuli earthquake fault rupture model and related geological structures reflect a transfer of strain from the right-lateral Dinaric fault system to the convergent Alpine system.

Acknowledgments. This work has been supported by EU DG12 contract "SGME" (ENV4-CT96-0296) and Italian CNR-GNDT 98.03238.PF54 and MURST-Cofinanziamento funds. We thank Jim Dewey for use of his JHD programs and Paul Spudich for carefully reading the revised manuscript. B. Bukchin was supported by a subcontract with Cornell University, (EAR-9804859, NSF), and the Russian Foundation (project 99-05-64964).

References

AGIP MINERARIA, *Microfacies Italiane,* S.Donato Milanese, Milan, 1959.

Amato, A., P. F. Barnaba, I. Finetti, G. Groppi, B. Martinis, and A. Muzzin, Geodynamic outline and seismicity of the Friuli Venezia Julia region, *Boll. Geofis. Teor. Appl., 19,* 217-256, 1976.

Ambraseys, N., The Gemona di Friuli Earthquake of 6 May 1976, *UNESCO Technical Report, RP/1975-76/2.222.3,* Paris, 1976.

Anderson, H., and J. Jackson, Active tectonics of Adriatic region, *Geophys. J. R. Astr. Soc., 91,* 937-983, 1987.

Aoudia, A., Active faulting and seismological studies for earthquake hazard assessment, Ph.D. thesis, 153 pp., Univ. of Trieste, October 1998.

Bosi, C., B. Camponeschi, and G. Giglio, Indizi di possibili movimenti lungo faglie in occasione del terremoto del Friuli del 6 maggio 1976, *Boll. Soc. Geol. It., 94,* 187-206, 1976.

Bukchin, B. G., A.L. Levshin, L.I. Ratnikova, B. Dost, and G. Nolet, Estimation of spatio-temporal source parameters for the 1988 Spitak, Armenia Earthquake, *Computational Seismology and Geodynamics, Am. Geophys. Union (eds),* 156-161, 1994.

Carraro, F., and F. Petrucci, Tentative assessment of the deformation of a morainic amphitheatre: the Tagliamento amphitheatre (Italy),*Z. Geomorph. N. F., 26,* 331-341, 1982.

Cipar, J., Teleseismic observations of the 1976 Friuli, Italy, earthquake sequence, *Bull. Seismol. Soc. Am., 70,* 963-983, 1980.

De Mets, C., R. G. Gordon, D. F. Argus, and S. Stein, Current plate motions, *Geophys. J. Int., 101,* 425-478, 1990.

Dewey, J. W., Seismicity studies with the method of joint hypocenter determination, Ph.D. thesis, 163 pp., Univ. Calif., Berkeley, 1971.

Ekstrom, G., and M. Nettles, Calibration of HGLP seismograph network and centroid-moment tensor analysis of significant earthquakes of 1976, *Phys. Earth Planet. Inter., 101,* 219-243, 1997.

Finetti, I., F. Giorgetti, H. Haessler, H. T. P. Hoang, D. Slejko, and G. Wittlinger, Time-space epicenter and hypocenter distribution and focal mechanism of 1976 Friuli earthquakes, *Boll. Geofis. Teor. Appl., 19,* 637-655, 1976.

Giorgetti, F., Isoseismal map of the May 6, 1976 Friuli earthquake, *Boll. Geofis. Teor. Appl., 19,* 707-714, 1976.

Granet, M., and T. P. Hoang, Some medium properties at Friuli (Italy) from amplitude spectrum analysis: a possible change in time or in space, *Tectonophysics, 68,* 167-182, 1980.

Lyon-Caen, H., Seismes du Frioul (1976): modeles de source a l'aide des sismogrammes synthetiques d'onde de volume, Ph.D. thesis, Univ. Paris VII., 1980.

Martinis, B., and A. Cavallin, The Friuli earthquake May 6, 1976: Ground cracks and sand mounds, *Boll. Geofis. Teor. Appl., 19,* 792-808, 1976.

Panza G. F., Synthetic Seismograms: the Rayleigh Waves Modal Summation, *J. Geophys., 58,* 125-145, 1985.

Panza, G.F., and P. Suhadolc, Complete strong motion synthetics, in *Seismic Strong Motion Synthetics, Computational Techniques,* edited by B. A. Bolt, pp. 153-204, Academic Press, Orlando, 1987.

Saraò, A., Das, S., and P. Suhadolc, Effect of non-uniform station coverage on the inversion for earthquake rupture history for a Haskell-type source model, *J. Seism., 2,* 1-25, 1998.

A. Aoudia, Dipartimento di Scienze della Terra, Università di Trieste, Via E. Weiss 1, I-34127 Trieste, Italy & Abdus Salam International Centre for Theoretical Physics, SAND Group, Trieste, Italy. (e-mail: aoudia@geosun0.univ.trieste.it)

A. Saraó and P. Suhadolc, Dipartimento di Scienze della Terra, Università di Trieste, Via E. Weiss 1, I-34127 Trieste, Italy. (e-mail: angela@geosun0.univ.trieste.it; suhadolc@geosun0.univ.trieste.it)

B. Bukchin, Institute of Earthquake Prediction and Mathematical Geophysics, Buid. 2, 79, Varshavskoe road, Moscow, 113556, Russia. (e-mail: bukchin@mitp.ru)

(Received September 18, 1999; revised November 10, 1999; accepted November 22, 1999.)

The 1998 Bovec-Krn mountain (Slovenia) earthquake sequence: Implications for earthquake hazard

J. Bajc

Geophysical Survey of Slovenia, Ljubljana, Slovenia

A. Aoudia[1]

The Abdus Salam International Centre for Theoretical Physics, Trieste, Italy

A. Saraò and P. Suhadolc

Department of Earth Sciences, University of Trieste, Trieste, Italy

Short title: THE BOVEC 98 SEQUENCE

Abstract. We study the 1998 Bovec-Krn mountain (Slovenia) earthquake sequence by combining hypocenters relocation, strong motion inversion, digital elevation modelling and field geology. We show that the main shock ($M_W = 5.6$) is related to a 12 km right lateral strike-slip on the Dinaric fault system with no evidences of surface faulting. The first 3 months of aftershock activity were restricted to the fault zone with very few off-fault events. Mainshock slip occured on a sub-vertical fault plane extending from 3 to 9 km depth. The rupture propagated bilaterally from the focus to terminate adjacent to two structural barriers. The northern barrier is adjacent to the Bovec basin at the junction between Dinaric and Alpine structures where there is a sharp change in the geometry of faulting. The southern barrier, the Tolminka-spring perched basin, is within the Dinaric system and corresponds to a 1 km restraining step-over. It exhibits evidences of recent activity presumably related to earlier slip events on a set of thrust faults rooting into the termination of a 30 km neighbouring stike-slip fault segment clearly visible on the digital elevation model. This segment is free of aftershocks and could be undergoing an increase of stress. This fault system represents the northeastern strand of the Idrija right-lateral fault.

1. Introduction

On April 12, 1998, at 10:55 GMT a magnitude $M_S = 5.7$ earthquake struck northwestern Slovenia close to the town Bovec near the border with Italy. This event is the largest so far instrumentally recorded earthquake in Slovenia and the best constrained one within the active collision zone between Eurasia and Adria at the junction between the Southeastern Alps and the Dinarides. This deforming area undergoes 4 to 5 mm/year of crustal shortening [*De Mets et al.*, 1990]. The epicenter is about 40 km east of the destructive Friuli 1976 thrust faulting earthquake [*Aoudia et al.*, 2000] and is located near the junction between Alpine structures trending E-W and external Dinaric structures trending NW-SE [*Aoudia*, 1998; *Benedetti*, 1999]. Its focal mechanism corresponds to an almost pure strike-slip faulting in agreement with the NW-SE trend of Dinaric structures. The aftershock zone does not match any already known active fault.

In this paper we provide accurate locations of the main shock and its aftershocks. We invert the available strong motion data to retrieve the moment release history along the activated fault. We combine these results with digital elevation modeling and field investigations to image the Bovec-Krn earthquake fault and its interaction with the brittle infrastructure of a larger fault zone. We discuss the active tectonics along the Dinaric fault system and its implications on the earthquake hazard in Slovenia and northeastern Italy.

2. Earthquake Relocation

The Bovec-Krn sequence has been well recorded by the national seismic networks of Slovenia, Italy, Croatia and Austria, as well as by the regional networks operating in the Friuli area (NE Italy) and run by the Osservatorio Geofisico Sperimentale (OGS) and the University of Trieste (DST). In addition, a few hours after the main event several local temporary stations were set up around the epicentral area by the Geophysical Survey of Slovenia. Over 4000 aftershocks have been recorded till the end of June 1998. We relocate the sequence by adapting the standard Joint Hypocenter Determination (JHD) method for teleseismic data [*Douglas*, 1967; *Dewey*, 1971] to local earthquakes. We developed an accurate travel time calculation procedure that is taking into account direct and head waves in a planar one-dimensional Earth model. 97 station-phase corrections have been obtained by applying the adapted JHD on 45 best recorded events, each having at least 45 P- or S-wave arrival times per event identified ($N_{ph} \geq 45$). These station-phase corrections have been passed to a single event location program in order to locate the 584 events with at least 10 recorded station-phases, a reasonable lower quality limit for the earthquakes processed. Only the events having the largest 90% hypocentral confidence ellipsoid axes smaller than 5 km have been retained in the final results. The vertical uncertainty is usually much larger than the horizontal ones and the corresponding 90% epicentral confidence ellipses are smaller than 500 m for most of the earthquakes.

In contrast with the use of JHD on teleseismic data, which utilizes the master events

in order to stabilize the inversion, we have fixed the P-wave arrival time correction on the temporary station DRZN (Fig. 1) to zero (Jim Dewey, personal communication, 1999). Because of the trade-off between the origin times and station-phase corrections this does not constrain any physical parameter, but still stabilizes the inversion.

The initial epicentral area (single event location with all station-phase corrections set to zero) can be roughly described as a NW-SE trending cluster with an approximate size of 20 km×10 km. The depths of the preliminary hypocentral locations were ranging from 0 to over 30 km, the lower limit having been immediately assessed as too deep for the geology of the area. The relocated events are well organized along a trend of about N125° and the epicentral area has an approximate size of 12 km×3 km (Fig. 1). The depth of the relocated events does not exceed 14 km. In fact, there are only 5 hypocenters that are deeper than 10 km, all of them located SW of the main fault, i.e., on the foot wall, whereas the shallowest are right below the surface. The depth of the main shock calculated with P-waves is 7.6 km $\pm$ 1.1 km, whereas the average depth and the median of the whole sequence are both at about 3.9 km (Fig. 2).

3. Strong Motion Inversion

The strong motion records of four three-component stations of the Friuli accelerometric network (Fig. 3) are inverted to study the source process of the main shock. The inversion, developed by *Das and Kostrov* [1990] makes use of weak physical constraints and allows the retrieval of the main features of the rupture process even in the case that four stations cover one side of the fault [*Saraò et al.*, 1998]. To model the

moment release during the Bovec-Krn earthquake, we assume a fault geometry consistent with the aftershock relocation [the source modeling procedure is fully described in *Das and Suhadolc*, 1996; *Saraò et al.*, 1998]. The fault, whose top has been placed at a depth of 3 km, is a rectangular plane, 13 km long and 7 km wide with strike 313°, dip 82° and rake 178° and has been discretized into 128 square subfaults of 0.8 km×0.8 km. This choice is a result of several inversion tests performed using different fault geometries. The inversion results are constrained by the requirements that the slip rate is positive and that the rupture velocity is smaller or equal to the S-waves velocity.

The accelerograms are bandpass-filtered between 0.1 and 1.0 Hz. We model about 10 seconds of the strong motion on each component. The obtained waveform fit (Fig. 3) is fairly good and very slight differences are visible for the station GERC. The moment release is shown in Figure 4. The total seismic moment retrieved is 4.5×10^{17} Nm. The overall slip distribution shows that the maximum energy release is around the hypocenter of the main shock decreasing towards the edges of the fault, where geometrical barriers are present. The analysis of the moment rate during the 3 seconds of the rupture history reveals that the rupture was growing in a bilateral way starting from the hypocenter. The distribution of the aftershocks is compatible with the slip; the aftershocks are more frequent in shallower areas that did not break during the main shock and there are no aftershocks in the vicinity of the hyopcenter during the entire investigated period.

4. Field Observations

The Bovec-Krn earthquake took place in a mountainous area that has been the site of a devastating earthquake sequence in 1511 [*Ribarič*, 1979] and was previously unexplored from the active tectonics point of view. The field investigations did not reveal any surface faulting. However, rock falls involving very large boulders and debris-flow were considerable in the epicentral area [*Vidrih and Ribarič*, 1998]. In Figure 5 the relocated aftershocks are plotted on a 25 meter sampling Digital Elevation Model (DEM). The majority of the aftershocks occurred in a narrow band along a N125° strike in good agreement with our P-wave first polarity focal mechanism solution. The length of the aftershock zone is about 12 km. Figure 5 clearly highlights two pronounced basins at both tips of the aftershock cluster, where there is a sharp cut-off in the seismic activity. The south-eastern tip of the aftershock sequence corresponds to the Tolminka-spring perched basin standing at 700 m of altitude, whereas the north-western tip corresponds to the large Bovec basin. The Bovec basin (5 km of width) is at the termination of the strike-slip geometry and at the junction between fully Dinaric and transition to Alpine structures. It displays a typical morphology of a down-thrown basin (Fig. 5). In this section we focus mainly on the Tolminka-spring basin, 1.5 km long and 1 km wide, because of its tectonic significance for the assessment of the hazard on the Dinaric strike-slip system. The field investigations and DEM analysis show that this basin is a restraining step-over within the strike-slip fault system (Fig. 5). The most striking feature within the basin is the step-like terrace morphology visible on its

eastern part and its well-organized drainage pattern. These terraces correspond to four eroded surfaces covered by fluvioglacial deposits with the upper terrace unconformably covered by slope deposits. The terrace surfaces are tilted towards the south-west with a tilt-magnitude and risers height increasing towards the upper terrace. The lowest terrace is bounded by a fault scarp trending N140° with a throw of 2 m presumably related to earlier slip events. While aftershocks mechanisms were generally consistent with the strike-slip rupturing parallel to the main shock, thrust geometry was locally evident in the Tolminka-spring basin [*Kravanja et al.*, 1999]. The Tolminka-spring restraining step is interpreted to have a half-flower structure cross-sectional geometry with the NE-dipping thrust faults rooting into the steep right-lateral strike-slip fault. This morphology is typical for thrust-faults acting as structures that allow slip transfer along the strike-slip, from one segment to another. The northern fault segment is where the Bovec-Krn mountain earthquake took place, whereas the southern segment (Fig. 6), clearly visible on the DEM, is being free of any aftershock. The field investigations reveal that the southern segment is a N140° right-lateral strike-slip with a minor thrust component. The DEM analysis indicates a lateral extent of over 30 km for the southern segment.

5. Conclusions and Implications for Earthquake Hazard

Our data show that the Bovec-Krn earthquake rupture is related to 12 km of strike-slip faulting. The location of the main shock hypocenter and the retrieved moment release history are consistent with the initiation of the rupture at the depth 8 km

and its bilateral growth. Merging the results derived from the earthquake relocation, strong motion inversion, DEM analysis, and field investigations, we conclude that the rupture is confined between two structural barriers (Figs. 5 and 6). The northwestern barrier is adjacent to the 5 km wide Bovec basin where there is a sharp change in the geometry of faulting [*Aoudia*, 1998; *Benedetti*, 1999] unlikely to be jumped during an earthquake. On the other hand, the southeastern barrier, the Tolminka-spring basin, is an antidilatational jog with a step-over of about 1 km that is likely to be jumped during an earthquake. The highly deformed quaternary deposits and related fault scarps in the Tolminka-spring basin suggest a recent activity of the neighbouring fault segment, whose trace on the DEM is very clear over a length of more than 30 km. This segment is free of aftershocks and could represent a presently locked segment undergoing an increase of stress. This fault system could have been the site of the most destructive known historical earthquake in the area, the March 26, 1511 earthquake with estimated macroseismic magnitude 6.8 [*Živčić et al.*, 1999]. It represents the northeastern strand of the Idrija right-lateral fault (Fig. 6) that exhibits witnesses of recent activity [*Aoudia*, 1998; *Benedetti*, 1999] without any major historical earthquake and thus should be of concern in terms of hazard.

Acknowledgments. The relocation part of this study was performed while one of the authors (J.B.) was a postdoctoral fellow at the University of Trieste with a scholarship granted by the "Consorzio per lo Sviluppo Internazionale dell'Universita' di Trieste". This research was funded by EU contract ENV4-CT96-0296 "Strong Ground Motion Estimates", Italian

MURST Cofinanziamento funds and Gruppo Nazionale per la Difesa dai Terremoti fund CNR 98.03238.PF54.

References

Aoudia, A., A. Saraò, B. Bukchin, and P. Suhadolc, The 1976 Friuli (NE Italy) thrust faulting earthquake: A reappraisal 23 years later, *Geophys. Res. Lett.*, *27*, 573-576, 2000.

Aoudia, A., Active faulting and seismological studies for earthquake hazard assessment, Ph.D. Thesis, 153 pp., Univ. of Trieste, 1998.

Benedetti, L., Sismotectonique de l'Italie et des regions adjacentes: fragmentation du promontoire adriatique, Ph.D. Thesis, 345 pp., Univ. Paris VII, 1999.

De Mets, C., R. G. Gordon, D. F. Argus, and S. Stein, Current plate motions, *Geophys. J. Int.*, *101*, 425-478, 1990.

Das, S. and B.V. Kostrov, Inversion for seismic slip rate and distribution with stabilizing constraints: Application to the 1986 Andreanof Islands earthquake, *J. Geophys. Res.*, *95*, 6899-6913, 1990.

Das, S. and P. Suhadolc, On the inverse problem for earthquake rupture. The Haskell-type source model, *J. Geophys. Res.*, *101*, 5725-5738, 1996.

Dewey, J. W., Seismicity studies with the method of joint hypocenter determination, Ph.D. Thesis, 163 pp., Univ. of Calif., Berkeley, 1971.

Douglas, A., Joint epicentre determination, *Nature*, *215*, 47-48, 1967.

Kravanja, S., G. Costa, G. F. Panza, and P. Suhadolc, Full moment tensor retrieval from waveform inversion: an application to the Bovec event (Slovenia) and its swarm, International Union of Geodesy and Geophysics, IUGG99 Abstracts, vol. B, 214, 1999.

Ribarič, V., The Idrija earthquake of March 26, 1511, *Tectonophysics*, *53*, 315-324, 1979.

Saraò A., S. Das, P. Suhadolc, Effect of non-uniform station coverage on the inversion for earthquake rupture history for a Haskell-type source model, *J. Seism.*, *2*, 1-25, 1998.

Vidrih, R. and M. Ribarič, Slope failure effects in rocks at earthquake in Posočje April 12 1998 and Europe Macroseismic Scale (EMS-98), *Geologija*, *41*, 365-410, 1998.

Živčić, M., F. Vaccari, and P. Suhadolc, Seismic zoning of Slovenia based on deterministic hazard computations, *Pure and Appl. Geophys.*, in press, 1999.

J. Bajc, Geophysical Survey of Slovenia, Pot na Golovec 25, 1000 Ljubljana, Slovenia. (e-mail: jure.bajc@gov.si)

A. Aoudia, The Abdus Salam International Centre for Theoretical Physics, Strada Costiera 11, P.O. Box 586, I-34100 Trieste, Italy. (e-mail: aoudia@dst.univ.trieste.it)

A. Saraò and P. Suhadolc, Department of Earth Sciences, University of Trieste, Via E. Weiss 1, I-34127 Trieste, Italy. (e-mail: angela@dst.univ.trieste.it; suhadolc@dst.univ.trieste.it)

Received _____

[1]Also at Department of Earth Sciences, University of Trieste, Trieste, Italy.

Sent to *Geophysical Research Letters*, 2000.

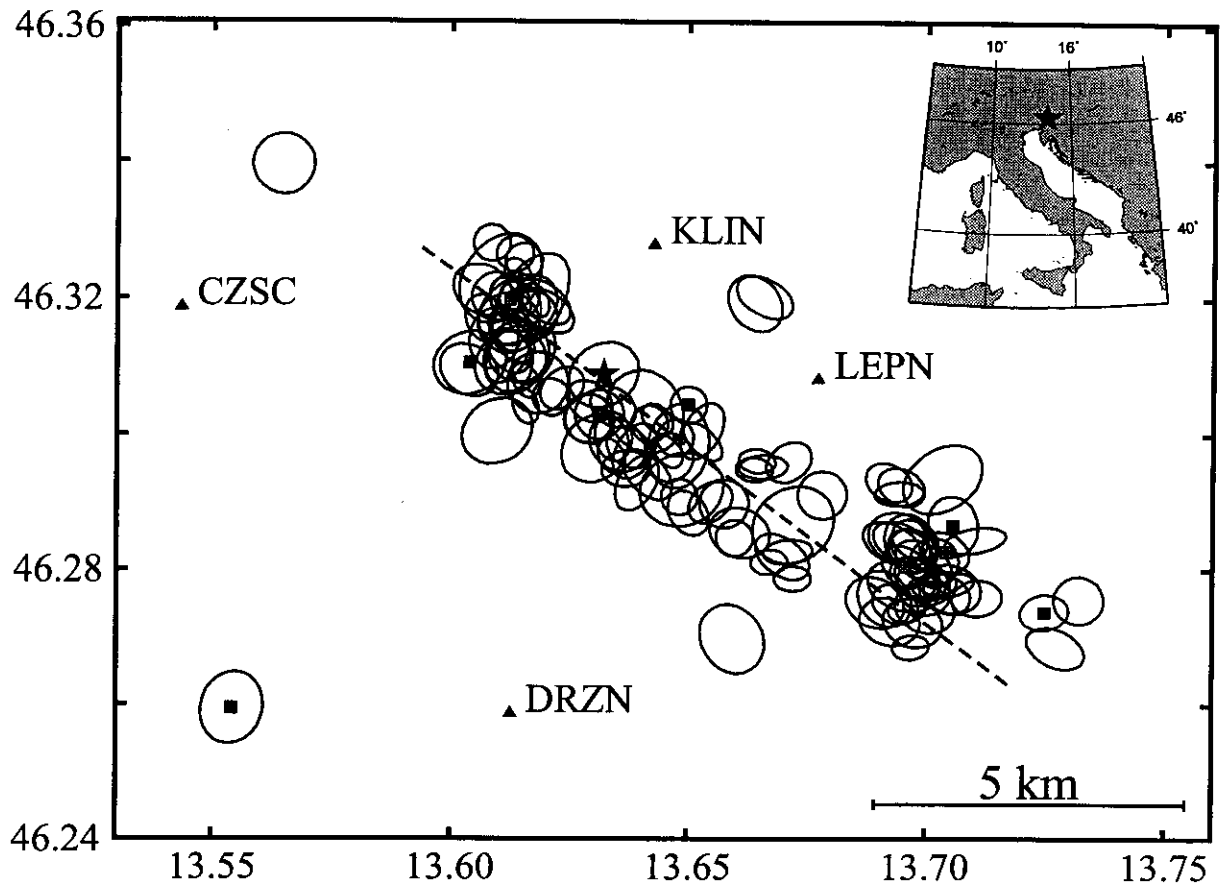

Figure 1. The 90% epicenteral confidence ellipses of the 122 well-recorded events ($N_{ph} \geq 30$) in the first 80 days after $M_S = 5.7$ 1998 Bovec-Krn earthquake (star). The squares show the aftershocks with $M_L \geq 3.0$, the triangles the temporary stations. The trend of the cluster (N125°) is added (dashed line).

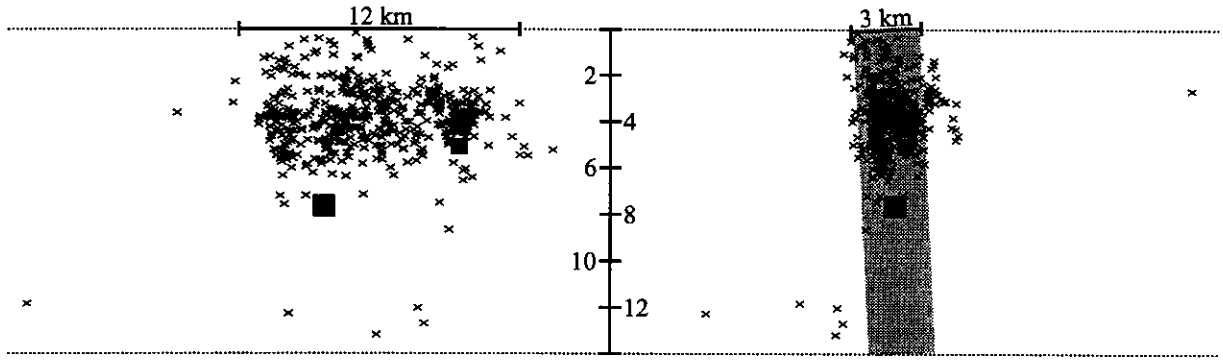

Figure 2. The hypocenters of the 548 well-recorded events ($N_{ph} \geq 10$) — the cross-section along (left) and perpendicular (right) to the trend on Fig. 1. The main shock and the strongest aftershock are denoted by squares, proportional to the magnitude, whereas all other aftershocks are shown as crosses. The depth distribution of the aftershocks is in good agreement with the northeast dipping sub-vertical fault plane of the P-wave focal mechanism shown in Fig. 5

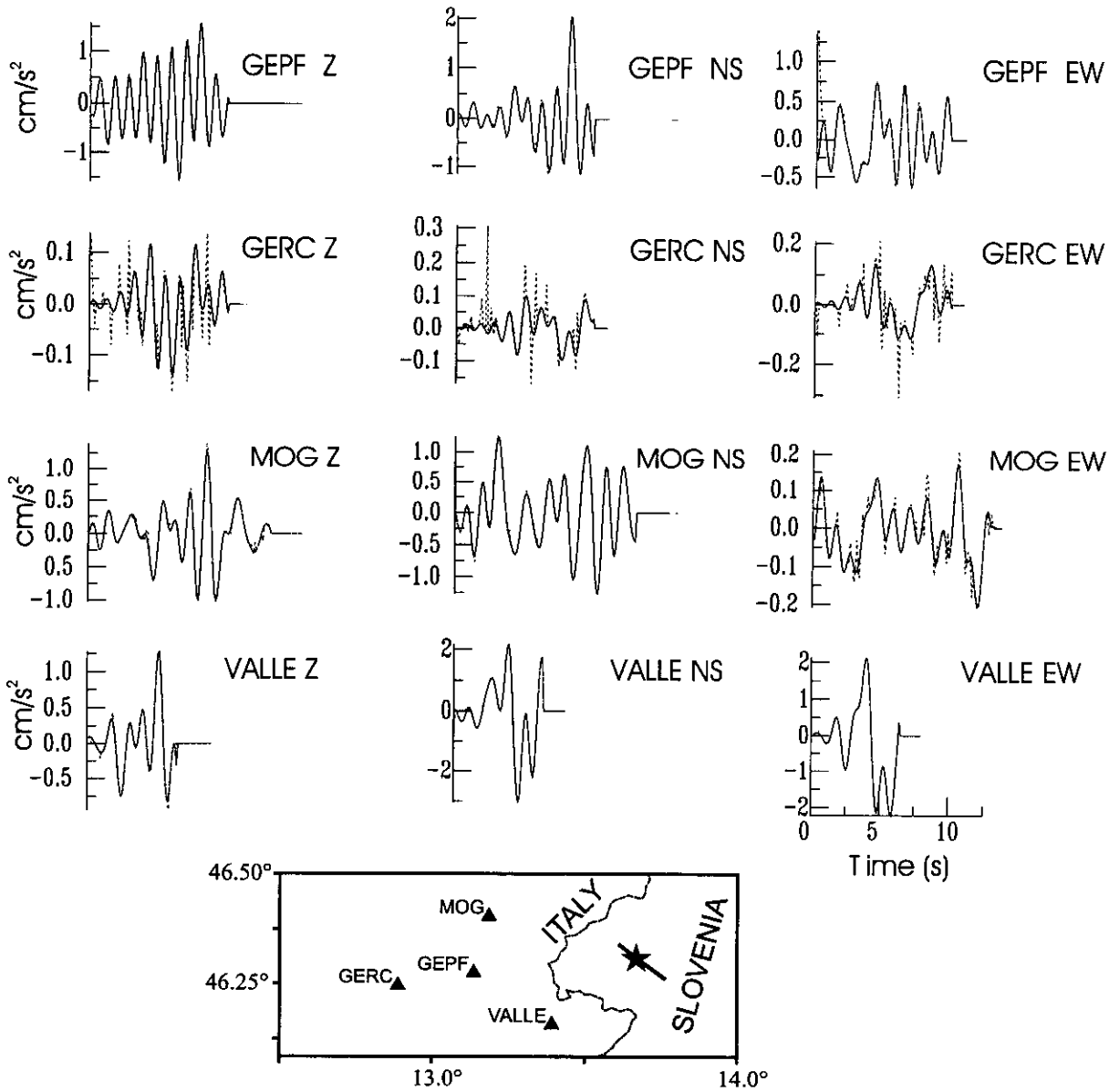

Figure 3. Comparison between the real (solid lines) and the synthetic accelerograms (red dotted lines) on the selected stations (bottom). The fault projection on the surface (thick line) and the epicenter (star) are also shown.

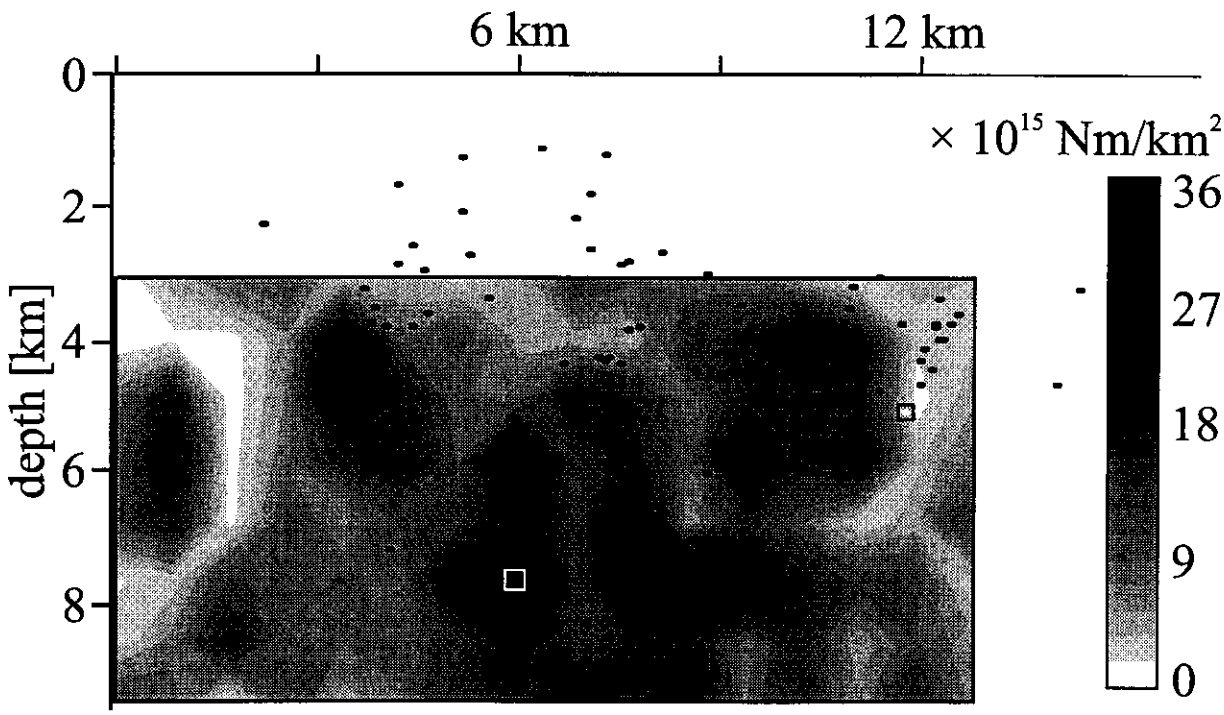

Figure 4. Moment release on the fault. The maximum moment (black shading) was released around the hypocenter of the main shock (white square). The aftershocks (dots) are more frequent in the areas that released less moment. In particular, the strongest aftershock (black square) with $M_L = 4.2$ occurred near the area that did not rupture (white shading) during the main shock.

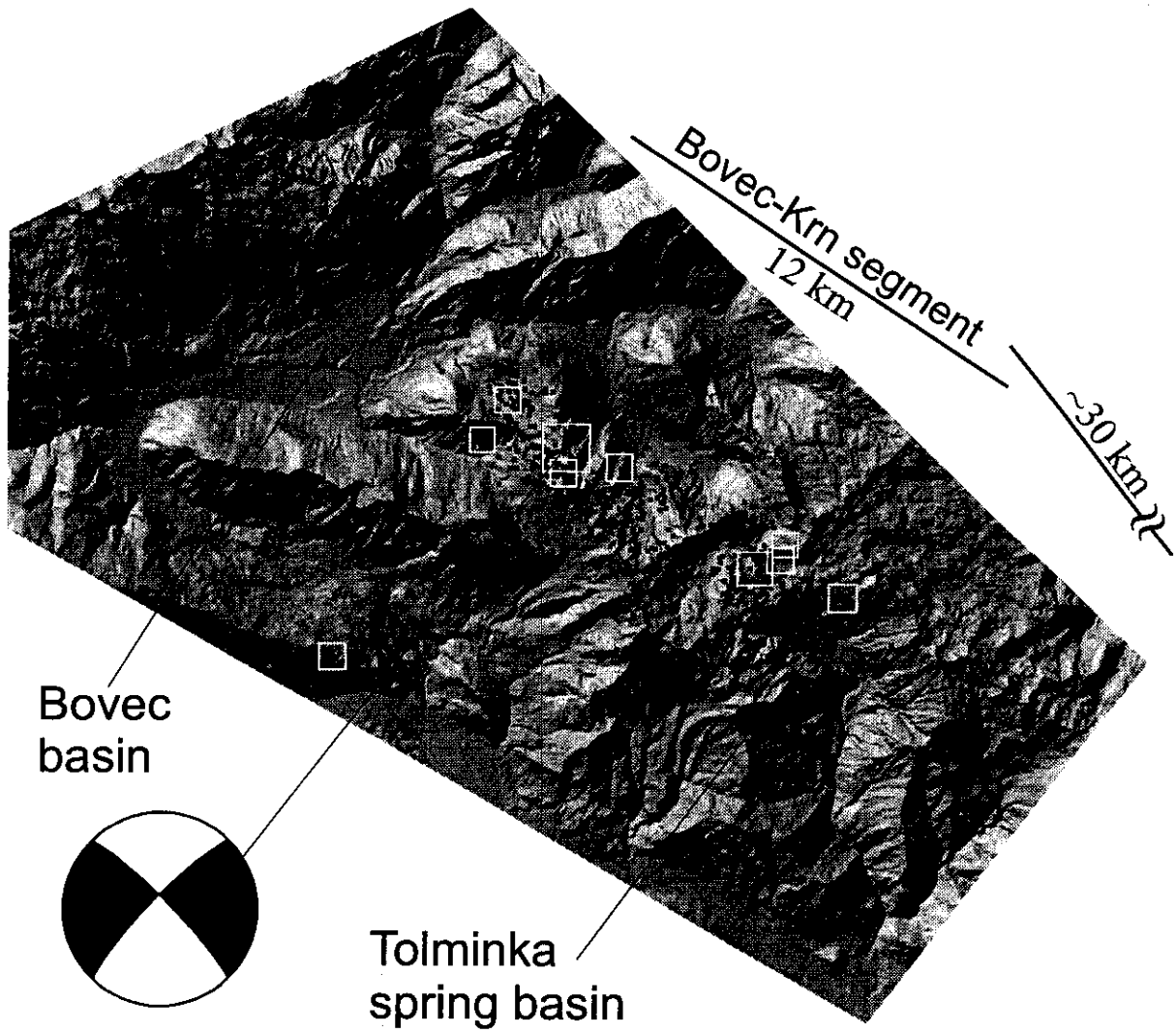

Figure 5. The epicenters (dots) of the 548 relocated earthquakes. The epicenters of the events with $M_L > 3.0$ are denoted by squares, proportional to the magnitude. The P-wave focal mechanism agrees well with the distribution of the aftershocks, which are confined between the Bovec and Tolminka-spring basins. In addition, the beginning of the nearly 30 km long lineament (Fig. 6) that extends southeast from the Tolminka-spring basin is shown.

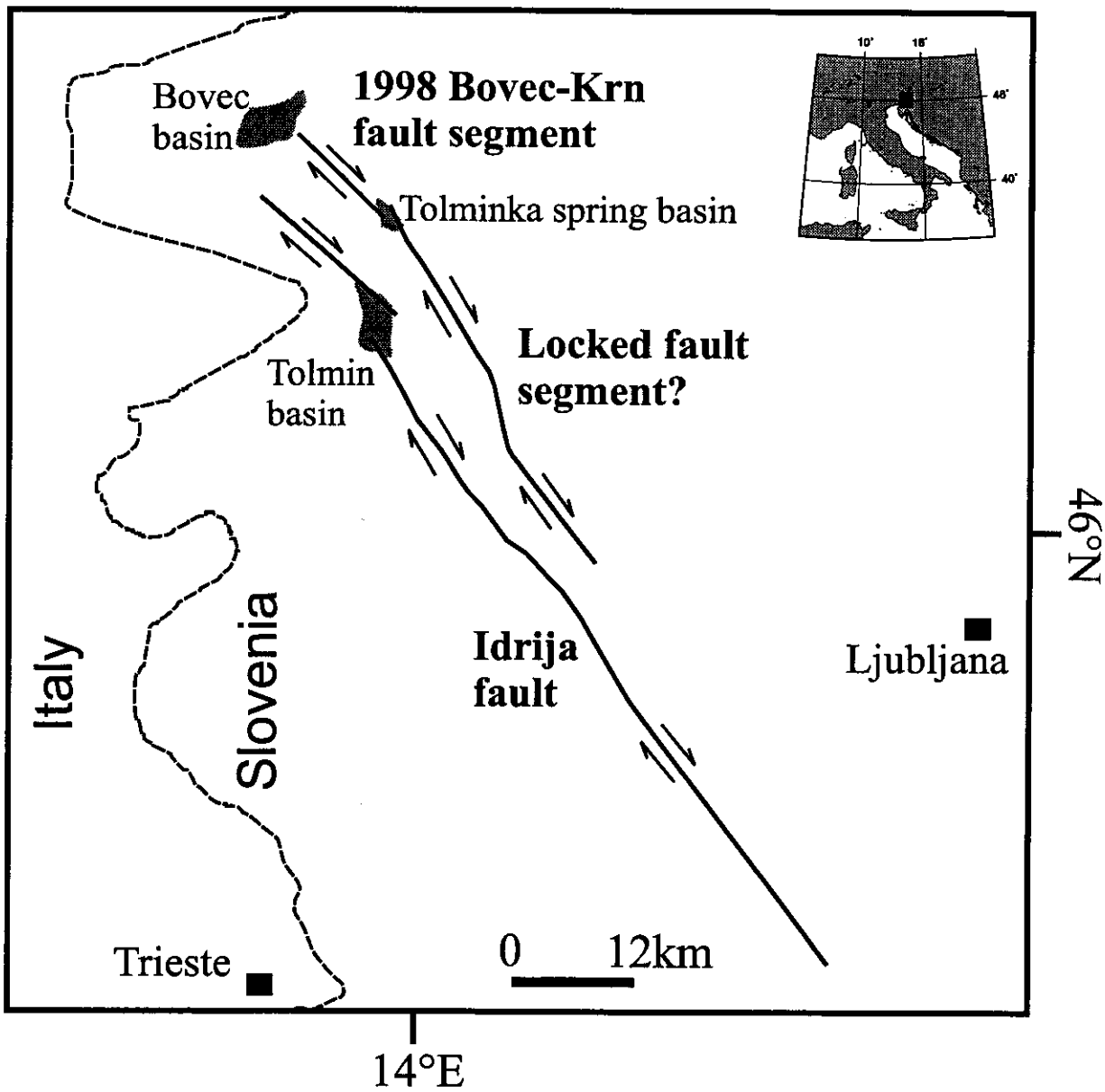

Figure 6. The Bovec-Krn earthquake fault segment and its interaction with the brittle infrastructure of the Idrija fault zone. The faults are mapped from 100 and 25 meter DEM (Surveying and Mapping Authority of the Republic of Slovenia, 1995; 1999).

Some References ...

Bullen and Bolt, 1985. An introduction to the theory of seismology, University Press Cambridge, pp.499.
Lay . and T.C. Wallace, 1995. Modern Global Seismology, Academic Press, London, pp. 521.

Moment Tensor Inversion:

Campus, P., Suhadolc, P., Panza, G.F. and Sileny, J., 1996. Complete moment tensor retrieval for weak events: application to orogenic and volcanic areas, In Seismic source parameters; from microearthquakes to large events, Tectonophysics, 261,147-163.

Cespuglio, G., Campus, P. and Sileny, J., 1996. Seismic moment tensor resolution by waveform inversion of few local noisy records-II. Application to Phlaegrean Fields (Southern Italy) volcanic tremors, Geophys. J. Int., 126, 620-634.

Dufumier, H., Michelini, A., Du, Z., Bondar, I., Sileny, J., Mao, W., Kravanja, S. and Panza G.F. (1997), "Regional Structure Modelling and Source Inversion for the 1992 Roermond Earthquake", *J. Seism.*, Vol. 1, pp. 321-340.

Frohlich, C., and Riedesel M. A., 1989. Note concerning possible mechanisms for non-double-couple earthquake sources. *Geophys. Res. Lett.*, 16, 523-526.

Jost, M.L. and R.B. Herrmann 1989. A Student's Guide to and review of Moment Tensors. Seismological Research Letters, 60, 37-57

Julian, B.R., Miller, A.D. and Fougler G.R., 1998. Non-double-couple earthquakes I. Theory, *Rev. Geophys.*, **36**, 525-549.

Kravanja, S., Panza, G.F. & Sileny, J., 1999a. Robust retrieval of seismic point source time function, *Geophys. J. Int.,* 136, 385-394

Kravanja, S., Batini, F., Fiordelisi, A. & Panza, G.F., 1999b. Full moment tensor retrieval waveform inversion in the Larderello geothermal area, in press on *Pure and Appl. Geophys.*

Panza, G.F. and Saraò, A., 2000. Monitoring volcanic and geothermal areas by full seismic moment tensor inversion: are non-double couple components always artefacts of modeling? In press on Geophys. J. Int., Knopoff's special issue.

Sileny, J., Panza, G.F. and Campus, P., 1992. Waveform inversion for point source moment tensor retrieval with optimization of hypocentral depth and structural model, Geophys. J. Int., 108, 259-274.

Sileny, J., Campus, P. and Panza, G.F., 1996. Seismic moment tensor resolution by waveform inversion of a few local noisy records-I. Synthetic tests, Geophys. J. Int., 126, 605-619.

Extended source Inversion

Aoudia A., G. Chimera, G. Costa, C. Nunziata, G.F. Panza, F. Romanelli, A. Saraò, P. Suhadolc and F. Vaccari, 1999. Modelling of the seismic ground motion of the Umbria-Marche sequence (September 1997). Proceedings of the 12th World Conference on Earthquake Engineering, CdRom – paper ID2500, Auckland, New Zealand.

Aoudia A., A. Saraò, B. Bukchin and P. Suhadolc, 2000. The 1976 Friuli (NE Italy) thrust faulting earthquake. A reappraisal 23 years later. *Geophys. Res. Lett,* 27, 573-577.

Bajc, J., A. Aoudia, A. Saraò, P. Suhadolc, 2000. The 1998 Bovec-Krn (Slovenia) earthquake sequence. Submitted to *Geophys. Res. Lett.*

Das, S. and B.V. Kostrov, 1990. Inversion for seismic slip rate and distribution with stabilizing constraints: Application to the 1986 Andreanof Islands earthquake. *J. Geophys. Res.*, 95, 6899-6913.

Das, S., P., Suhadolc and B.V., Kostrov, 1996. Realistic inversions to obtain gross properties of the earthquake faulting process. *Tectonophysics*, .261, 147-163.

Das S. and P. Suhadolc, 1996. On the inversion problem for earthquake rupture. The Haskell-type source model. *J. Geophys. Res.*, 101, 5275-5738.

Saraò A., S. Das and P. Suhadolc, 1998. Effect of non-uniform station coverage on the inversion for seismic moment release history and distribution for a Haskell-type rupture model. *J. Seism.*, 2, 1-25.

Scaling Parameters for Forward Modelling

Wells, D.L., K.J. Coppersmith, 1994.
New Empirical Relationships among Magnitude, Rupture Length, Rupture Width, Rupture Area, and Surface Displacement.
BSSA, 84, 4, 974-1002.

Somerville, P., Irikura, K., Graves, R., Sawada, S., Wald, D., Abrahamson, N., Iwasaki, Y., Kagawa, T., Smith, N. and Kowada, A., 1999. Characterizing Crustal Earthquake Slip Models for the Prediction of Strong Ground Motion. Seism. Res. Lett, 70, 1, 59-80.